

2020-10-14

The Natural History of Bone Marrow Lesions and Cysts in the Dunkin-Hartley Guinea Pig Knee Osteoarthritis Model

Francis, Destiny

Francis, D. (2020). The Natural History of Bone Marrow Lesions and Cysts in the Dunkin-Hartley Guinea Pig Knee Osteoarthritis Model (Master's thesis, University of Calgary, Calgary, Canada). Retrieved from <https://prism.ucalgary.ca>.

<http://hdl.handle.net/1880/112686>

Downloaded from PRISM Repository, University of Calgary

UNIVERSITY OF CALGARY

The Natural History of Bone Marrow Lesions and Cysts in the Dunkin-Hartley Guinea Pig Knee
Osteoarthritis Model

by

Destiny Francis

A THESIS

SUBMITTED TO THE FACULTY OF GRADUATE STUDIES
IN PARTIAL FULFILMENT OF THE REQUIREMENTS FOR THE
DEGREE OF MASTER OF SCIENCE

GRADUATE PROGRAM IN BIOMEDICAL ENGINEERING

CALGARY, ALBERTA

OCTOBER, 2020

© Destiny Francis 2020

Abstract

Idiopathic knee osteoarthritis (OA) is a disease with unknown etiology, where age is described as a major risk factor. There is a need to document OA's natural history to gain insight into its etiology. Therefore, an animal model like the Dunkin-Hartley (DH) guinea pig that spontaneously develops a knee OA phenotype similar to idiopathic OA observed in humans can be used to study the disease-related bony degeneration. This phenotype includes osteophyte formation, sclerosis, bone marrow lesions (BMLs), and cysts within a relatively short period. This thesis employs advanced magnetic resonance imaging (MRI), micro-computed tomography (μ CT), and histological techniques to assess knee joint degeneration in DH guinea pigs at ages 2, 4, 6, 12, and 24 months. The results from this project show evidence of cartilage degradation and bone cyst formation in the 6-month age group, which becomes more apparent in the 12 and 24-month age groups. When present, cysts were primarily located in the central compartment of the bone and often accompanied by osteophytes and sclerosis. Joint degeneration was most severe in the 24-month age group with the largest cysts as well as the greatest osteophyte size and number. Bone microarchitecture was also significantly affected in this age group. Overall femoral and tibial trabecular number (Tb.N) was lowest in the 24-month age group, and it had the highest medial femoral subchondral bone plate thickness (Sbp.Th), femoral and tibial subchondral bone plate porosity (Sbp.Po), femoral trabecular separation (Tb.Sp), and medial tibial trabecular thickness (Tb.Th). The medial compartment also revealed greater joint degeneration, as demonstrated by greater femoral and tibial Sbp.Th and femoral Sbp.Po in the 12 and 24-month age groups compared with the lateral compartment. This project demonstrates that age-related joint degeneration occurs in the DH guinea pig spontaneous knee OA model with evidence of osteophytes, cysts, and bone microarchitecture alterations in older age groups. Although histology revealed abnormalities in the bone

that have been associated with MRI-defined BMLs, I am unable to conclude whether or not BMLs occur in this model as a further investigation with MRI is still required.

Preface

Chapter 1: A general introduction of the thesis.

Chapter 2: A literature review of topics relevant to this thesis.

Chapter 3: A manuscript-based chapter describing age-related joint degeneration in the Dunkin-Hartley guinea pig using assessments from micro-computed tomography, magnetic resonance imaging, and histology.

Chapter 4: A general discussion on the findings in this thesis.

Acknowledgements

I want to express my deepest appreciation to all those that made it possible to complete my thesis project. To Dr. Sarah Manske, my supervisor, who deserves special thanks for her guidance and advice. Thank you, Sarah, for taking me on as a student, teaching me a lot about my project, and always dedicating time to review my work and address my questions. I am also grateful to my supervisory committee, Drs. John Matyas and Jeff Dunn for helping me shape this thesis. Thank you, Dr. John Matyas, for reviewing my research proposal, answering my questions about bone histology and helping me with microscopy. Many thanks to Dr. Jeff Dunn for providing direction for my thesis title, research questions and MRI protocol. It has been an honour to work with all of you.

I want to thank the technicians who helped me complete this project, from MR imaging to histology. Thank you, Dragana Ponjevic, for dedicating many hours to sectioning and staining my samples for histology. Thank you, David Rushforth, for MR scanning my early samples. I am also grateful to Dr. Heather Jamniczky for permitting me to use her desktop MRI and offering me free credits to take an MRI-operating course in Massachusetts. Thank you to the McCaig Institute for Bone and Joint Health, specifically the McCaig Education Committee, for providing me with a Special Training Opportunities Fund (STOF) award to attend this MRI-operating course.

Furthermore, I want to thank Dr. Andres Kroger for sharing the data analysis pipeline to analyze bone microstructure in the knee joint's weight-bearing regions. Thank you, Dr. Leigh Gabel, for guiding me through choosing the appropriate statistical tests to answer my research questions. I am also very thankful to be a part of the Manske Lab, which introduced me to incredible people. Thank you, Alicia Gabilondo, for teaching me many skills, including animal handling and micro-computed tomography scanning that helped me with my thesis project. Also, for making

sure I had all the lab supplies I needed. Thank you, Michael Kuczynski, Justin Tse, Scott Brunet and Jenn Bhatla for helping me with random tasks that came up during my time in the lab, and for being a great team.

Additional thanks to the Biomedical Engineering Graduate Program for awarding me a Biomedical Engineering Graduate Program Academic Scholarship and introducing me to fascinating research areas under the biomedical engineering umbrella.

Lastly, I would like to thank my family and friends for supporting me throughout my degree. I am grateful to have them in my corner.

Table of Contents

<i>Abstract.....</i>	<i>i</i>
<i>Preface.....</i>	<i>iii</i>
<i>Acknowledgements.....</i>	<i>iv</i>
<i>List of Figures.....</i>	<i>ix</i>
<i>List of Tables.....</i>	<i>xi</i>
<i>List of Abbreviations</i>	<i>xii</i>
CHAPTER 1: Introduction.....	1
1.1 Purpose and Aims	3
1.2 Thesis Outline	3
CHAPTER 2: Background and Literature Review	4
2.1 Knee Joint Anatomy	4
<i>2.1.1 Articular Cartilage</i>	<i>5</i>
<i>2.1.2 Subchondral Bone.....</i>	<i>7</i>
<i>2.1.3 Menisci</i>	<i>8</i>
<i>2.1.4 Ligaments</i>	<i>8</i>
2.2 Medical Imaging	9
<i>2.2.1 X-ray Planar Radiography and Computed Tomography</i>	<i>10</i>
<i>2.2.2 Magnetic Resonance Imaging</i>	<i>11</i>
2.3 Knee Osteoarthritis.....	12
<i>2.3.1 Risk Factors.....</i>	<i>12</i>

2.3.2 Pathology	13
2.3.3 Diagnosis	16
2.3.4 Imaging.....	18
2.3.5 Histological Evaluation of Knee OA	19
2.3.6 Treatment.....	21
2.3.7 Preclinical Models.....	22
2.4 Dunkin-Hartley Guinea Pig	23
2.4.1 Risk Factors of Human Knee OA Studied in the DH Guinea Pig.....	23
2.4.2 Tissue Changes Related to Risk Factors of Knee OA	24
2.4.3 Knee OA Assessment in the DH Guinea Pig.....	28
2.5 Summary.....	28
 Chapter 3: Age-related Joint Degeneration in the Dunkin-Hartley Guinea Pig: Joint	
Assessments with Micro-computed Tomography, MRI and Histology	29
3.1 Introduction	29
3.2 Methods	31
3.2.1 Ethics Statement.....	31
3.2.2 Sample Collection.....	31
3.2.3 Magnetic Resonance Imaging	31
3.2.4 Micro-computed Tomography and Bone Microarchitecture Analysis	32
3.2.5 Rat Arthritis Knee Scoring System (RAKSS)	34
3.2.6 Histology.....	35
3.2.7 Visual Assessments.....	36
3.2.8 Statistical Analysis.....	36
3.3 Results.....	37

3.3.1 MRI Hyperintensities	37
3.3.2 RAKSS	40
3.3.3 Bone Microarchitecture	42
3.3.4 Histological Assessments	56
3.4 Discussion	60
3.5 Conclusions	64
Chapter 4: General Discussion.....	65
4.1 Addressing Aims	65
4.2 Validity of Measurements	66
4.3 Study Limitations.....	67
4.4 Future Directions	67
4.5 Concluding Remarks	68
References.....	70
Appendix A – Additional Tables and Figures	83
Appendix B – Extended Methods.....	87
Appendix C – Copyright Permissions	91

List of Figures

- Figure 1.** Anterior view of a coronal section of the knee (patella not depicted). Netter illustration used with permission of Elsevier Inc. All rights reserved. www.netterimages.com (12)..... 4
- Figure 2.** Diagrammatic representation of the articular cartilage zones. The organization of chondrocyte (left) and collagen fibrils across all three zones (right). Used with permission from Wolters Kluwer Health, Inc., Journal of the American Academy of Orthopaedic Surgeons. 6
- Figure 3.** The ACR clinical classification criteria for knee OA (45). Chart reproduced from (46). 17
- Figure 4.** An overlay of medial and lateral weight-bearing regions (purple) on the left (A) femur and (B) tibia from a DH guinea pig. The central region is between the medial and lateral regions. 33
- Figure 5.** Masked regions of the femur (A) and tibia (B) indicating the areas of the cortical plate (purple) and trabecular bone (grey) that were included in the bone microarchitecture analysis.. 34
- Figure 6.** Coronal MR images of DH guinea pig tibiofemoral joints at 2, 4, 6, 12, and 24 months. T2 FLASH with fat suppression images at ages 2 (A) and 4 months (B). (C) STIR image of a 6-month-old with hyperintensities in the lateral femur, central femoral and tibial epiphyses, and ACL. (D) STIR image of a 12-month-old with two hyperintensities in the central femoral epiphysis, one in the tibial epiphysis, and another in the joint space. (E) T2 FLASH image of a 24-month-old with an even larger hyperintensity in the central femoral epiphysis, two in the tibia, and one in the joint space. White arrows indicate hyperintensities. 38
- Figure 7.** Fluid-sensitive MR (A, B, C) and complementary μ CT (D, E, F) images of guinea pig tibiofemoral joints at ages 6 (A, D), 12 (B, E) and 24 (C, F) months. White arrows indicate cysts as defined by hyperintensities on fluid-sensitive MRI and corresponding cavities in the trabecular bone..... 40
- Figure 8.** Maximum subchondral bone plate thickness (mm) in the lateral, central and medial compartments of the (A) femur and (B) tibia plotted across DH guinea pig age groups. Data points represent individual animals. Mean \pm SD maximum Sbp.Th for age groups are indicated by the full circles and error bars, respectively. Simple effects results from the two-way ANOVA tests are represented in (A), where * and *** mean $p < 0.05$ and $p \leq 0.001$, respectively. Main effects results are represented in (B), where NS and *** mean $p > 0.05$ and $p \leq 0.001$, respectively. 43
- Figure 9.** Subchondral bone plate porosity (%) in the lateral, central and medial compartments of the (A) femur and (B) tibia plotted across DH guinea pig age groups. Data points represent individual animals. Mean \pm SD Sbp.Po for age groups are indicated by the full circles and error bars, respectively. Simple effects results from the two-way ANOVA tests are represented in (A), where *, **, and *** mean $p < 0.05$, $p \leq 0.01$, $p \leq 0.001$, respectively. Main effect results are represented in (B), where ** and *** mean $p \leq 0.01$ and $p \leq 0.001$, respectively. 45
- Figure 10.** Trabecular bone mineral density (mgHA/cm³) in the lateral, central and medial compartments of the (A) femur and (B) tibia plotted across DH guinea pig age groups. Data points represent individual animals. Mean \pm SD Tb.BMD for age groups are indicated by the full circles and error bars, respectively. Main effect results from the two-way ANOVA test are represented in (A), where NS and *** mean $p > 0.05$ and $p \leq 0.001$, respectively. Simple effects

results are represented in (B), where *, **, and *** mean $p < 0.05$, $p \leq 0.01$, and $p \leq 0.001$, respectively. 47

Figure 11. Trabecular bone volume fraction (%) in the lateral, central and medial compartments of the (A) femur and (B) tibia plotted across DH guinea pig age groups. Data points represent individual animals. Mean \pm SD Tb.BV/TV for age groups are indicated by the full circles and error bars, respectively. Main effect results from the two-way ANOVA test are represented in (A), where NS and *** mean $p > 0.05$ and $p \leq 0.001$, respectively. Simple effects result is represented in (B), where * and *** mean $p < 0.05$ and $p \leq 0.001$, respectively. 49

Figure 12. Trabecular thickness (mm) in the lateral, central and medial compartments of the (A) femur and (B) tibia plotted across DH guinea pig age groups. Data points represent individual animals. Mean \pm SD Tb.Th for age groups are indicated by the full circles and error bars, respectively. Simple effects results from the two-way ANOVA tests are represented on plots, where NS, **, and *** mean $p > 0.05$, $p \leq 0.01$, and $p \leq 0.001$, respectively. 51

Figure 13. Trabecular number (mm^{-1}) in the lateral, central and medial compartments of the (A) femur and (B) tibia plotted across DH guinea pig age groups. Data points represent individual animals. Mean \pm SD Tb.N for age groups are indicated by the full circles and error bars, respectively. Main effects from the two-way ANOVA test are represented on plots, where ** and *** mean $p \leq 0.01$ and $p \leq 0.001$, respectively. 53

Figure 14. Trabecular separation (mm) in the lateral, central and medial compartments of the (A) femur and (B) tibia plotted across DH guinea pig age groups. Data points represent individual animals. Mean \pm SD Tb.Sp for age groups are indicated by the full circles and error bars, respectively. Main effect results from the two-way ANOVA test are represented in (A), where * and *** mean $p < 0.05$ and $p \leq 0.001$, respectively. Simple effect results are represented in (B), where *, ** and *** mean $p < 0.05$, $p \leq 0.01$ and $p \leq 0.001$, respectively..... 55

Figure 15. Image of cysts seen on H&E-stained sections from three DH guinea pig age groups. (A&D) ACL cyst in a 2-month-old. (B&E) Femoral cyst in a 12-month-old. (C&F) Femoral cyst and cystic rim in a 24-month-old. Photomicrographs were scanned at 20X magnification. 56

Figure 16. Anomalies (indicated by arrows) were seen on H&E-stained sections of the subchondral bone of the DH guinea pigs. (A&D) A femoral osteophyte (highlighted) near the site of cruciate ligament insertion in a 6-month-old. (B, E, & F) An abnormal soft connective tissue (solid arrow) and an anomaly (dashed arrow) similar to a fibrous clot in a 6-month-old femur. (C&G) A tibial cyst (solid arrow) adjacent to fibrotic tissue (dashed arrow) detected in a 12-month-old. Photomicrographs were scanned at 20X magnification..... 57

Figure 17. Anomalies (indicated by black arrows) on H&E-stained sections that were bone-related, as seen on μ CT images. (A&D) 6-month-old, (B&E) 12-month-old, (C&F) 24-month-old. Photomicrographs were scanned at 20X magnification. μ CT images were upscaled by a factor of 2.5..... 58

Figure 18. Toluidine-blue stained sections of the articular cartilage overlying a (A&C) 6-month-old tibia and (B&D) 12-month-old tibia. (C) The zoomed in region of the 6-month-old tibial articular cartilage shows fibrillation and fragment loss in the superficial and transitional zone and a moderate reduction in matrix staining. (D) The zoomed in region of the 12-month-old tibial articular cartilage shows fibrillation and loss of matrix stain to the deep zone. Photomicrographs were scanned at 10X magnification. 59

List of Tables

Table 1. Summary of MR sequences and their scan acquisition parameters.....	32
Table 2. Modified rat arthritis knee scoring system (RAKSS). Osteophytes are scored in 8 regions (anterior and posterior medial and lateral locations for femur and tibia each), and sclerosis is scored in 4 regions (medial and lateral tibia and femur). Adapted from (98)....	35
Table 3. Animal characterization by age, sample size, weight, and level of skeletal maturity.	37
Table 4. Description of the hyperintense regions observed on MRI in different DH guinea pig age groups according to their mean count, anatomical locations, whether they are bone changes and match BML or cyst definitions.	39
Table 5. Median (interquartile range) of RAKSS scores based on μCT bony features. Different letters (^{a,b}) indicate significant differences in total RAKSS score (Kruskal-Wallis test and subsequent pairwise multiple comparisons, $p < 0.05$).	41

List of Abbreviations

Abbreviation	Definition
ACL	Anterior cruciate ligament
BLOKS	Boston Leeds osteoarthritis knee score
BMD	Bone mineral density
BML	Bone marrow lesion
BS2	Bristol strain 2
BV/TV	Bone volume fraction
CT	Computed tomography
DH	Dunkin-Hartley
DXA	Dual-energy X-ray absorptiometry
ECM	Extracellular matrix
FLASH	Fast low angle shot
H&E	Hematoxylin-eosin
HHGS	Histologic Histochemical Grading System
HR-pQCT	High-resolution peripheral quantitative computed tomography
KL	Kellgren and Lawrence
MOAKS	Magnetic resonance imaging osteoarthritis knee score
MRI	Magnetic resonance imaging
NSAIDs	Nonsteroidal anti-inflammatory drugs
NTX	Urinary N-telopeptide of type I collagen
OA	Osteoarthritis
OARSI	Osteoarthritis research society international

PCL	Posterior cruciate ligament
PET	Positron emission tomography
RAKSS	Rat arthritis knee scoring system
Sbp.Po	Subchondral bone plate porosity
Sbp.Th	Subchondral bone plate thickness
SNR	Signal-to-noise ratio
STIR	Short tau inversion recovery
Tb.BMD	Trabecular bone mineral density
Tb.BV/TV	Trabecular bone volume fraction
Tb.N	Trabecular number
Tb.Sp	Trabecular separation
Tb.Th	Trabecular thickness
WORMS	Whole-organ magnetic resonance imaging score
μ CT	Micro-computed tomography

CHAPTER 1: Introduction

Osteoarthritis (OA) is a complex and slowly progressing degenerative disease that affects the entire synovial joint. It is among the most common chronic health conditions and a leading cause of pain and lower extremity disability in older adults (1,2). It is characterized radiographically by joint space narrowing, meniscal damage, and bone malformations, such as subchondral bone sclerosis, osteophyte formation, and bone cysts (3). OA commonly affects joints of the knees, hips, hands, and ankles. In particular, knee OA is highly prevalent. Its incidence increases with age, and it is more prevalent in females than males (1).

There are two main forms of OA: primary and secondary OA. Primary or idiopathic OA is a spontaneous form of OA with unknown causes and higher incidence rates with increasing age and in women (1). It is a more prevalent form of OA compared with post-traumatic OA, a common form of secondary OA that occurs after a joint injury and makes up only approximately 12% of symptomatic OA cases (4). Studying the pathogenesis of idiopathic OA in humans has been challenging due to the lack of a demonstrable acute event that triggers onset, and as a result, there are many unknowns in early disease onset and progression.

Studies using imaging to understand OA are important in describing the tissue-level degeneration associated with the disease and can be conducted *in vivo* throughout the disease process. While a weak correlation exists between symptoms and radiographic findings (5), advanced imaging techniques are useful to characterize the presence and timing of the disease-related changes. Such techniques include magnetic resonance imaging (MRI) and quantitative computed tomography.

Magnetic resonance imaging has allowed for the non-invasive diagnosis of bone marrow lesions (BMLs), which are associated with pain in late-stage knee OA (2). Specifically, Felson et

al. (2001) found that approximately 78% of people with knee pain had BMLs, while 30% of people without knee pain had BMLs (2). BMLs appear as irregularly shaped regions of hyperintense signal on fluid-sensitive MR sequences (6). These lesions have been observed in weight-bearing regions of the knee and associated with histological abnormalities, such as adipocyte necrosis, bone marrow fibrosis and subchondral cysts (6,7). Some BMLs have been found to progress to cysts (92% incidence rate), which can be visualized using MRI as well as radiography (8,9).

Advanced computed tomography (CT) imaging techniques, such as high-resolution peripheral quantitative computed tomography (HR-pQCT) and micro-computed tomography (μ CT), have allowed for quantitative measurements of bone microarchitecture parameters, such as bone mineral density, subchondral bone plate thickness, subchondral bone plate porosity, and trabecular thickness, number, and separation (10,11). Bone microarchitecture is affected during OA. Specifically, regions in the subchondral bone where BMLs were present, paradoxically, had a more plate-like trabecular structure with increased trabecular thickness, higher volumetric bone mineral density (BMD), and little to no overlying articular cartilage compared to regions in the same samples where they were absent, suggesting that they are likely associated with the progression of OA (7).

Despite these advancements, the etiology of primary OA is still not well understood. There is a need to document the entire natural history of OA. This can be made possible with an animal that models human idiopathic knee OA. The Dunkin-Hartley (DH) guinea pig develops a spontaneous knee OA phenotype over its life span, and BMLs have not been studied extensively in this model.

1.1 Purpose and Aims

The overall purpose of this project is to describe the natural history of knee OA in a spontaneous knee OA model. This project will address the following *aims*:

1. Document the knee joint degeneration in the DH guinea pig with complementary information from MRI, μ CT, and histology.
2. Investigate the presence and timing of BMLs and cysts in the subchondral bone of the DH guinea pig relative to other pathological features associated with the development of knee OA.
3. Characterize the development of insertional cysts and whether they are associated with pathological features of knee OA.

1.2 Thesis Outline

Chapter 1 introduces the thesis, the rationale behind this project, and its purpose and aims.

Chapter 2 is a literature review on knee osteoarthritis describing the anatomical and morphological components involved in the disease, and the techniques developed to study it.

Chapter 3 is a manuscript-style chapter on this project titled Age-related Joint Degeneration in the Dunkin-Hartley Guinea Pig: Joint Assessments with Micro-computed Tomography, MRI and Histology.

Chapter 4 is a general discussion addressing the aims, limitations, and future directions of this project.

Appendices include additional figures, extended methods and scripts used in this project, as well as copyright permissions obtained for this thesis.

CHAPTER 2: Background and Literature Review

2.1 Knee Joint Anatomy

The knee joint is the largest synovial joint in the human body. As a synovial joint, it is made up of a fluid-filled capsule, the synovium, lined with a synovial membrane. Within the synovium, the articulating surfaces of the bones covered by thin layers of hyaline cartilage meet. There are two articulations in the knee joint: the tibiofemoral and patellofemoral. The tibiofemoral joint consists of the femur and the tibia, and it is the weight-bearing component of the knee. Two menisci (medial and lateral) are located within this joint, while the collateral and cruciate ligaments connect the bones (Figure 1).

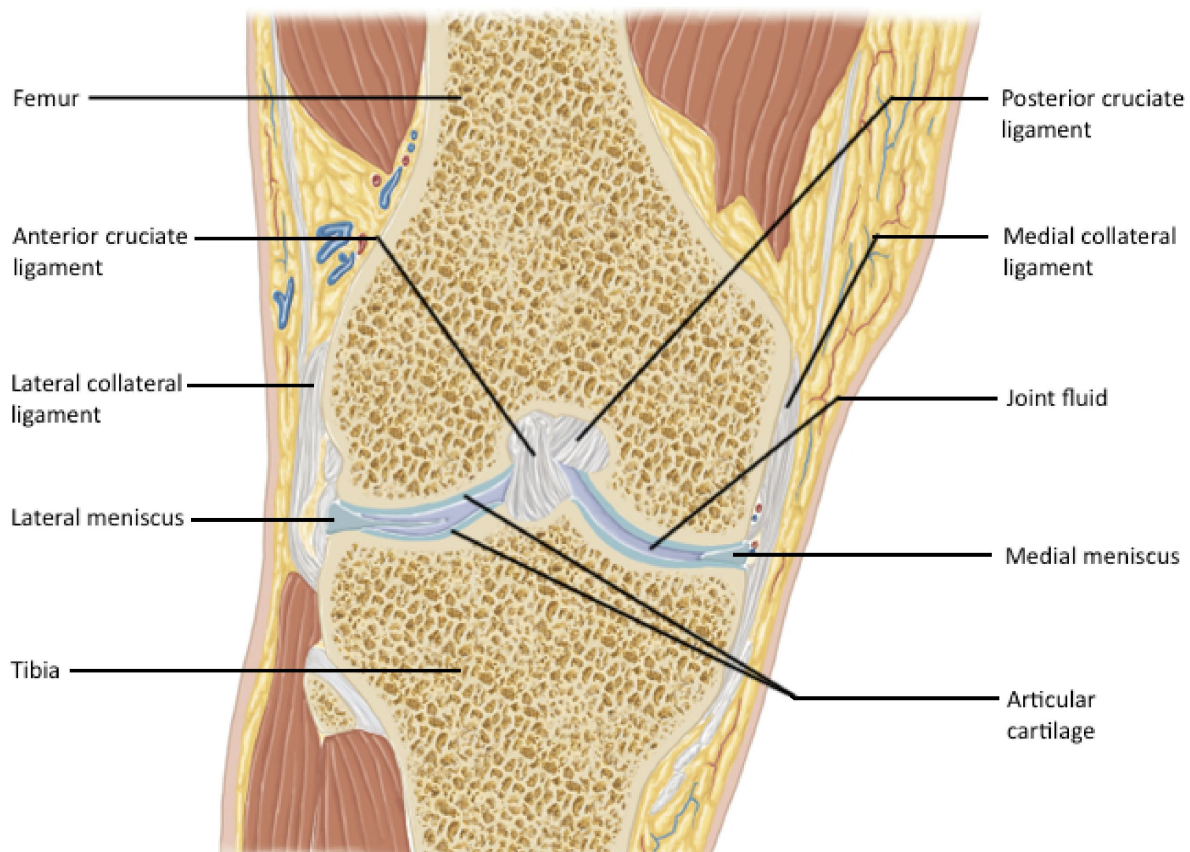


Figure 1. Anterior view of a coronal section of the knee (patella not depicted). Netter illustration used with permission of Elsevier Inc. All rights reserved. www.netterimages.com (12).

The patellofemoral joint is made up of the patella and femur, and it enables knee extension movement because of the quadriceps femoris tendon that attaches to the patella. The quadriceps femoris tendon extends into the patellar ligament, which attaches to the tibia (12). Around this joint are several synovial fluid-filled sacs called bursa.

All structures in the knee joint play unique roles that allow for mobility, stability, strength, shock absorption and reduce/prevent friction.

2.1.1 Articular Cartilage

The articular cartilage is a thin layer of hyaline cartilage that covers the bones of a synovial joint, like the knee joint. It is an avascular structure made up of a dense extracellular matrix (ECM) and specialized cells known as chondrocytes (13). The ECM contains water, collagen, proteoglycans and other proteins that contribute to the cartilage's biomechanical properties, such as its ability to resist significant loads. Chondrocytes are essential to the development, maintenance, and repair of the ECM (13).

There are three zones in the articular cartilage: the superficial/tangential zone that is located at the proximal end of the articular surface and in contact with synovial fluid, the middle/transitional zone, and the deep zone, which is situated distally. All three zones have distinct cellular and molecular organization that allow for their unique properties (Figure 2). In the superficial zone, collagen fibrils are arranged parallel to the articular surface and tightly packed, and a relatively large number of chondrocytes are present and flattened (13). This arrangement allows the cartilage to resist forces caused by articulation.

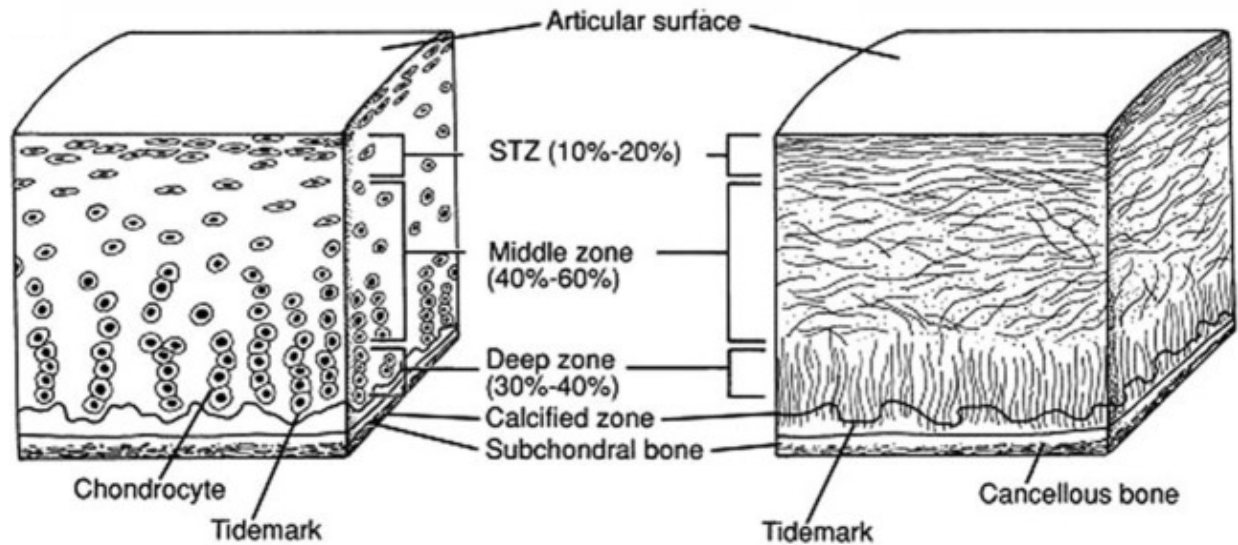


Figure 2. Diagrammatic representation of the articular cartilage zones. The organization of chondrocyte (left) and collagen fibrils across all three zones (right). Used with permission from Wolters Kluwer Health, Inc., Journal of the American Academy of Orthopaedic Surgeons.

The middle zone is specialized to resist compressive forces (13). It is the largest of the three zones and serves as a bridge between the other two zones. It contains randomly organized collagen fibrils and spherical chondrocytes that are at low density (13,14).

Similar to the middle zone, the deep zone is also responsible for resisting compressive forces. However, it is designed to have the greatest stiffness (13). The chondrocytes in this zone are in a columnar organization while the collagen fibrils are arranged radially, with both parallel to each other and perpendicular to the joint line. The deep zone is separated from the calcified layer of the cartilage by a tidemark. The calcified layer secures the cartilage to the bone by connecting the collagen fibrils in the deep zone to the subchondral bone (13).

2.1.2 Subchondral Bone

The subchondral bone is the bone underlying the articular cartilage. In the knee joint, this means the femur, tibia and patella. At the tibiofemoral articulation, the femur and tibia are long bones with epiphyses above their growth plates, metaphyses below their growth plates, and a diaphysis. Both the epiphysis and metaphysis consist of a shell of dense cortical bone that borders a spongy trabecular bone, while the diaphysis is a hollow shaft of cortical bone (15).

Directly below the calcified cartilage, in the epiphysis, is a thick plate of cortical bone known as the subchondral bone plate. The cortical bone in the subchondral bone plate is dense and solid, similar to cortical bone in other skeletal locations, but less stiff than the cortical bone in the diaphysis (15,16). Beneath this bone plate is the trabecular bone, a mesh-like structure of trabecular plates and rods spread around the bone marrow. The trabecular bone is more porous and has a lower ratio of bone volume to total volume compared with the cortical bone (15,16).

Bone undergoes changes during life. It grows, changes its shape, and gets renewed over time. The subchondral bone can grow longitudinally and radially. During longitudinal growth, which happens at the growth plate, cartilage proliferates in the epiphysis and metaphysis then becomes mineralized to form primary new bone (15).

Bone can gradually change its shape due to biomechanical forces or physiological influences (15). Bone remodelling is a lifelong process whereby mature bone is resorbed and replaced with a newly formed bone (15). Bone remodelling makes use of specialized cells called osteoclasts and osteoblasts. Osteoclasts resorb bone while osteoblasts form bone. This process is necessary to maintain the mechanical strength of bone (15). The subchondral bone withstands repetitive cycles of mechanical loading, and damage may occur due to these loads (17). Bone remodelling may

prevent the accumulation of bone microdamage. It might also enable bone to adapt to its mechanical environment to reduce the risk of fracture (17).

2.1.3 Menisci

The medial and lateral menisci are crescent-shaped fibrocartilage structures that are attached to the intercondylar part of the tibia. Their functions include load transmission, shock absorption, joint stability, lubrication, and proprioception (18). The medial meniscus is located on the medial aspect of the knee. The anterior and posterior sides of the medial meniscus are attached to the intercondylar part of the tibia, anterior to the anterior cruciate ligament (ACL) and the posterior cruciate ligament (PCL), respectively. At the periphery of the medial meniscus, it is fixed to the joint capsule.

The lateral meniscus is smaller than the medial meniscus and it is more mobile (18). While it is attached to a greater portion of the articular surface than the medial, it has an area in the region of the popliteus tendon where it is not attached to the joint capsule, making it fairly mobile (19). Its anterior side is attached to the intercondylar fossa, which is located near the broad attachment site of the ACL, while its posterior is attached to the PCL and medial femoral condyle (18).

2.1.4 Ligaments

Ligaments connect bones in synovial joints. They are important for the function of the knee joint because they enable joint stability, preventing excessive movement. There are three major ligaments in the knee joint, the patellar, collateral and cruciate ligaments. The patellar ligament is located at the front of the joint capsule, where it extends as a continuation from the quadriceps femoris tendon and attaches onto the tibial tuberosity (12). This ligament is more commonly called

the patellar tendon because it contains fibres of the quadriceps femoris tendon. However, it functions as a ligament since it connects bone (patella) to bone (tibia). The medial collateral ligament is attached proximally at the medial femoral epicondyle and distally at the medial tibial condyle while the lateral collateral ligament is attached proximally at the lateral femoral epicondyle and distally on the lateral fibular head (20). Both collateral ligaments function to restrain valgus and varus rotation (21).

The cruciate ligaments prevent the anteroposterior displacement of the tibiofemoral joint. The ACL starts at the posterior side of the femoral intercondylar notch, medial to the lateral condyle and ends in a groove that is anterior and lateral to the medial tibial tubercle in the intercondylar fossa (20). The PCL starts at the posterior side of the femoral intercondylar notch, lateral to the medial condyle and ends in a depression that is posterior to the intra-articular upper surface of the tibia.

2.2 Medical Imaging

Medical imaging allows for the non-invasive visualization of human anatomy. It has been valuable for confirming the presence of diseases, tracking their progression, and assessing responses to treatment. Imaging modalities can be grouped according to the processes that they use to form an image. For example, X-ray planar radiography and computed tomography (CT) modalities are based on the principles of x-ray transmission while MRI is based on the electromagnetic induction of nuclei with angular momentum.

The fundamental physics underlying each imaging modality enables them to provide contrast between objects or tissues based on the physical characteristics the objects possess. This review will focus on imaging physics that allow certain modalities to image the knee joint. For this

purpose, the knee is divided into two components: bone and soft tissue, where the modalities that excel for providing contrast in bone imaging are planar radiography and CT, while soft tissue displays excellent contrast on MRI.

2.2.1 X-ray Planar Radiography and Computed Tomography

X-ray planar radiography and CT imaging are based on how various tissues absorb x-rays (22). The various tissues in the knee joint have different x-ray attenuation coefficients, which is a measure of the degree to which x-rays are scattered and absorbed within tissues (23). Radiographs have dark regions that correspond to low attenuation and varying degrees of bright regions with the brightest region corresponding to the highest attenuation. Bone has a higher attenuation coefficient than soft tissue because of its relatively high density; therefore, it appears brighter on radiographs (23).

In planar radiography and CT, x-rays are generated from a source and directed towards a patient. The x-rays that pass through the patient are detected on a detector located opposite the source. The detector converts the x-ray energy to light, which is then converted into a voltage and is digitized (22). In planar radiography, the digitized image is a two-dimensional projection of the tissues situated between the x-ray source and detector.

Computed tomography images are three-dimensional radiographs. In CT, there is a synchronous rotation of the x-ray tube, which houses the source, and multiple detectors to obtain one-dimensional projections at multiple angles around the patient (22). The one-dimensional projections undergo image reconstruction to create a two-dimensional image. The third dimension is obtained when the source and detectors acquire projections at multiple locations in the horizontal direction (22).

2.2.2 Magnetic Resonance Imaging

Magnetic resonance imaging makes use of the nuclear magnetic resonance properties of the protons in tissues (23). Most MRI is designed to image hydrogen nuclei in various tissues, because of the abundance of the hydrogen atom in biological tissues (23,24). A patient placed in an MRI scanner is placed in a relatively strong magnetic field. The magnetic field of the scanner causes all charged and moving hydrogen nuclei to become magnetized according to the law of electromagnetic induction (25).

To obtain an MR image, a patient is placed in a scanner with a radiofrequency transmitter positioned around them. The transmitter sends radiofrequency waves of energy equal to the Larmor frequency of hydrogen. This causes the hydrogen nuclei to achieve resonance, which varies by position in the patient because of the magnetic field gradient coils in the scanner (23). When the transmitter is switched off, the nuclei tries to return to equilibrium, which causes a radiofrequency wave signal to be emitted (26). This signal is detected by the receiver coils in the scanner, which uses the frequency and phase information of the signal to determine their position in the patient.

A knee joint imaged with MRI will display varying intensities based on the magnetic properties of the tissues. Since bone has a relatively low concentration of hydrogen atoms, it has a relatively low signal intensity on an MRI. However, in adult humans, where bone marrow may be fatty, the shape of the bone can still be visualized. Soft tissues have much better contrast than bone because of the high concentration of hydrogen atoms from water and lipid molecules (24). Image contrast between various soft tissues can be achieved in MRI acquisition techniques that utilize the specific times it takes tissues to return to equilibrium after the radiofrequency transmitter is switched off (27).

2.3 Knee Osteoarthritis

Osteoarthritis is the most common type of arthritis (28). Compared with osteoarthritis in other joints, knee OA most commonly leads to clinical symptoms and disability (29). The Framingham Osteoarthritis Study reported that both radiographic and symptomatic knee OA prevalence increased with age in a population >65 years, and women were more likely to have symptomatic knee OA than men (29). This study demonstrated that age and sex play a role in OA prevalence, but its etiology is unclear.

Age-related knee OA with unknown etiology is often referred to as primary or idiopathic knee OA. It is different from secondary OA that results from a predisposing condition. One example of secondary OA is post-traumatic knee OA, which stems from injury to one or multiple components of the joint, such as an ACL or meniscal tear. Idiopathic OA in the knee has been postulated to result from the intersection of biological, morphological, and neuromuscular changes to the musculoskeletal system during ageing (30).

2.3.1 Risk Factors

Idiopathic OA etiology is often described as multifactorial, as such complex interactions between mechanical, cellular and biochemical factors likely contribute to its onset. Several cross-sectional studies have explained that there are certain risk factors for OA (31–33). Johnson and Hunter (2014) divided these risk factors into person-level and joint-level risk factors (34).

In idiopathic knee OA, person-level risk factors could be age, sex, genetics, obesity and diet. Age has been described as the main risk factor of OA (33). While its exact mechanism for etiopathogenesis is unknown, it has been proposed that OA onset can be explained by kinematic changes to cartilage loading driven by ageing over a long period coupled with older cartilage that

cannot adapt to load-bearing changes, leading to articular surface damage and increased collagen fibrillation (30). Sex has also been proposed as an important risk factor because several studies have reported higher OA incidence rates in postmenopausal women (33,34). Family history has also been linked to OA incidence, and candidate genes, such as insulin-like growth factor 1, genes for vitamin D receptors, type 2 collagen and growth differentiation factor 5, involved in the disease inheritance have been identified (34). The link between obesity and OA has been discussed extensively in the literature (35). The Framingham Study found that obesity precedes OA development, and that could be due to increased joint loading on the knee (32). While some studies have agreed that the relationship between obesity and knee OA could be biomechanical, there has also been a reason to suggest that there might be some metabolic and inflammatory systemic effects at play (33). Investigations on diet and OA have highlighted the importance of adequate intake of vitamins D, C and K because of their roles in articular cartilage and bone metabolism, antioxidant activity, and the regulation of bone and cartilage mineralization, respectively (34).

A joint-level risk factor for idiopathic knee OA is knee malalignment. The Tanamas et al. (2009) systematic review concluded that knee malalignment is an independent risk factor for radiographic knee OA progression (36). Abnormal knee alignment was strongly correlated with increased deterioration in whichever compartment was under greater mechanical stress (34). This means that individuals with a varus knee alignment were more likely to have knee OA in their medial compartment; however, this may not necessarily predict OA incidence (34,37).

2.3.2 Pathology

In knee OA, the entire synovial joint often undergoes degeneration. The cartilage matrix structure and composition changes. Specifically, the collagen network that is responsible for the

matrix integrity and strength is weakened. As a result, there is a decreased ability of the collagen network to counteract the swelling of proteoglycans, leading to cartilage swelling (38). Fibrillations to the cartilage surface, fissuring and degradation develop, which eventually leads to the exposure of the underlying calcified cartilage and subchondral bone (39). While cartilage volume initially increases due to swelling, fissuring and degradation lead to a loss in volume.

Knee OA progression in the subchondral bone is associated with damage to the trabecular bone structure, the increased thickness of the bone plate, known as sclerosis, as well as the formation of osteophytes (bony outgrowths that form along bone edges), bone marrow lesions and cysts (39). In early-stage OA, it has been proposed that the trabecular bone is lost and the subchondral bone plate becomes thinner due to the increased rate of bone remodelling that occurs (16). However, as the disease advances, bone turnover, which refers to the rates of bone remodelling, is reduced. A decline in bone resorption occurs, but it is not accompanied by a similar decline in bone formation (16). Late-stage OA also involves subchondral bone sclerosis, which is the hardening of bone.

Bone marrow lesions are MRI-defined features observed on fluid-sensitive MR sequences, such as the fat-suppressed T2-weighted and short tau inversion recovery (STIR) sequences, as irregularly shaped regions of hyperintense signal in the bone (6). They have been associated with pain in OA (40). Felson et al. (2001) compared MRI data of OA patients with pain versus those without and found that BMLs were found statistically to predict patients with pain (2,40). These lesions were previously referred to as bone marrow “edema”, but edema is not always present when they occur (41). BML etiology is poorly understood; however, a retrospective study that used histology to analyze arthroplasty samples with BMLs reported the presence of adipocyte necrosis and bone marrow fibrosis where these lesions were present (7). Adipocyte necrosis is the

death of fat cells possibly due to the lack of blood supply, while bone marrow fibrosis is the presence of fibrotic tissue in the bone marrow, which occurs most likely due to pathology. Another study found these features in addition to trabecular abnormalities, including cysts and cartilage fragments (6).

Subchondral cysts in OA have been studied extensively and for much longer than BMLs (8,9,42). Cysts are round voids surrounded by trabecular bone, so they can be visualized on radiographs. Subchondral cysts also contain a fluid-like substance, similar to BMLs, and they appear bright on fluid-sensitive MR sequences. However, they can be differentiated from BMLs because of their well-delineated margins (43). Cysts have been frequently observed in advanced knee OA, and there are two main theories explaining their cause (8,42). The first theory is the synovial fluid intrusion theory, which states that cysts form due to raised intraarticular pressure that causes leakage of synovial fluid in the bone through fissures or breaks in the cartilage. This means that for this theory to be valid, subchondral cysts would only occur in areas of the bone with complete cartilage loss or fissuring (8). The other theory, bone contusion/bruise theory, explains that cysts occur as a result of bone necrosis, which is induced by abnormal mechanical stress and subsequent microfracture (8,42). Research that supports the bone contusion theory expects BMLs to precede these cysts because there should be evidence of bone trauma like necrosis and fibrosis (6,8). Pouders et al. (2008) explained that in their clinical experience with MRI, cysts are more common in the central region of the tibia, a non-weight bearing area that is not covered by cartilage, and this finding does not support either theory (9). However, upon MRI and histological evaluation of arthroplasty samples from advanced knee OA patients, they found that both central and weight-bearing cysts were very prevalent and showed evidence of necrosis in the bone, which is more consistent with the bone contusion theory. This led to the proposal that the cysts in the central

region might be experiencing mechanical stresses from the cruciate ligaments (9). Another study, Son et al. (2018), also reported these cysts and termed them insertional cysts because they occurred near the site of attachment of the cruciate ligaments and could have originated due to possible abnormal stresses at the ACL insertional site (44).

2.3.3 *Diagnosis*

Knee OA is diagnosed based on clinical and radiographic data. Diagnosing OA is challenging because there is a poor correlation between knee OA symptoms and radiographic evidence of the disease (5). This means that patients with knee OA symptoms may show no radiographic evidence of OA and vice-versa. The presence of symptoms in patients with OA is the driving factor for diagnosis. Symptoms are more common in advanced OA cases, so diagnosis is easier in advanced OA (39).

There are specific diagnostic criteria for clinical and radiographic knee OA to differentiate the disease from other forms of arthritis (39). The ACR clinical classification criteria for knee OA include patient history and physical examination, often combined with radiographic and laboratory findings (45). This criterion states that knee pain and at least a number of other characteristics must be present to warrant a knee OA classification depending on the components (history and physical examination + radiographic/laboratory findings) used to make the classification (Figure 3).

Using history and physical examination	Using history and physical examination + radiographic findings	Using history and physical examination + laboratory findings
+3 of the following	Pain in the knee +1 of the following	+5 of the following
Over 50 years of age < 30 minutes of morning stiffness Crepitus on active motion Bony tenderness Bony enlargement No palpable warmth of synovium	Over 50 years of age < 30 minutes of morning stiffness Crepitus on active motion and osteophytes	Over 50 years of age < 30 minutes of morning stiffness Crepitus on active motion Bony tenderness Bony enlargement No palpable warmth of synovium ESR < 40 mm/hour Rheumatoid Factor < 1:40 Synovial fluid signs of OA

Figure 3. The ACR clinical classification criteria for knee OA (45). Chart reproduced from (46).

Limitations to the current diagnostic criteria have been discussed in the literature (39). Joint space narrowing has been found to occur more often than osteophytes, yet it is not included in the criteria. The joint space consists of the articular cartilage, menisci, and other soft tissues that undergo degeneration in knee OA, which are not visible on radiographs. Moreover, structural abnormalities seen in MRI can be used to diagnose OA, but only in combination with the ACR diagnostic criteria (47).

2.3.4 Imaging

Radiographic OA, i.e. the presence of structural changes in OA, is important for understanding the disease etiology. The implementation of imaging techniques for researching OA has led to significant findings about this disease. Many studies have used conventional radiography, MRI, CT, ultrasound, and positron emission tomography (PET) to image knee joints with OA (48–50). However, ultrasound and PET are not frequently used.

Conventional radiography is easily accessible in clinical practice and has been used to define OA changes. Radiographically, knee OA is defined by osteophyte presence, joint space narrowing, and subchondral bone sclerosis (49). Knee OA can be assessed using conventional radiography, both semiquantitatively and quantitatively. A popular semiquantitative scoring system for OA is the Kellgren and Lawrence (KL) grade (51). The KL grade is a five-grade system (0 – none, 1 – doubtful, 2 – minimal, 3 – moderate, and 4 – severe OA) that can be used to score OA severity. This assessment is based on a single x-ray view, where the knee joint is imaged in the supine position (52). However, posteroanterior radiographs performed under weight-bearing and semiflexion conditions have been demonstrated to be reproducible and allow for better visualization of the joint space (52). Quantitative assessment of knee OA using conventional radiography consists of measuring joint space width using a ruler (48). This can be done with a physical device or software application on a digitized image for improved precision.

Magnetic resonance imaging has been used extensively in OA research to quantify the soft tissue changes associated with the disease since they cannot be visualized with radiography (47,48,53). This imaging technique also has semiquantitative and quantitative assessments available for knee OA. The Whole-organ Magnetic Resonance Imaging Score (WORMS), Boston Leeds Osteoarthritis Knee Score (BLOKS), and MR Imaging Osteoarthritis Knee Score (MOAKS) are

three common semiquantitative scoring systems that report OA changes in individual MR imaging features (54–56). These scoring systems use different grades and approaches (subregional or site-specific) to score cartilage, BMLs, subchondral cysts, osteophytes, bone attrition (only in WOMS), effusion, synovitis, menisci, ligaments, periarticular features, and loose bodies (48). Quantitative assessment of knee OA with MRI involves the use of digital image processing derived measurements of articular cartilage thickness and volume, meniscal position and volume, and volumes of BMLs, synovitis, and effusion (48,53).

Using computed tomography, the knee joint can be imaged in 3D compared to conventional radiography. CT may play a useful role in OA diagnosis with its improved visualization of calcified cartilage and subchondral bone changes, such as sclerosis, cysts and osteophytes, but it is currently not used diagnostically. In research, quantitative CT techniques, including HR-pQCT and μ CT, have been used to characterize knee OA changes. The availability of sophisticated 3D segmentation and analysis techniques have allowed for quantitative assessments of bone microarchitecture parameters, such as bone mineral density, subchondral bone plate thickness, subchondral bone plate porosity, and trabecular thickness, number and separation, all which undergo changes during OA progression (10,11,57).

2.3.5 Histological Evaluation of Knee OA

Like imaging, histology is an important tool for describing OA pathogenesis. Histology is the study of the microscopic structure of biological tissues, and the use of a histopathological approach is considered the gold standard for confirming the presence and severity of OA (58). Tissue removed from the knee, usually following knee arthroplasty, can be examined histologically to characterize OA. Animal models have also been used to describe the disease histologically. This

is typically performed using one of two grading systems: the Mankin scoring or the Osteoarthritis Research Society International (OARSI) grading system (59). Both scoring systems make use of cationic histological stains such as hematoxylin, safranin O or toluidine blue. Hematoxylin, safranin O and toluidine blue are acidophilic dyes as they bind to tissues with a high DNA and RNA content. The hematoxylin-eosin (H&E) stain is a standard stain for visualizing microscopic anatomy, while safranin O-fast green and toluidine blue stains highlight proteoglycans and type II collagen in the cartilage. The Mankin and OARSI scoring systems require knowledge of the degree of cationic staining in normal cartilage tissue because changes in the volume of stain are used to assess pathology.

Mankin scoring, also known as the Histologic Histochemical Grading System (HHGS), recommends H&E and safranin O-fast green histological stains (60). This scoring system uses a 14 point score to assess the articular cartilage cellular changes, histochemical distribution of safranin O matrix staining, and structural changes, such as erosion and vessel penetration through tidemark (61).

The OARSI grading system is a six-grade scoring system that is also used to assess cartilage histopathology (61). Grades are used to characterize the severity of OA. The principle behind this is that the earliest cartilage changes would be observed near the surface of the cartilage, while changes in the deeper parts of the cartilage would become apparent as OA progresses (61). Consequently, normal cartilage is grade 0, while grade 1 OA is defined by fibrillation, cartilage matrix swelling, chondrocyte death, clustering, and hypertrophy in the superficial zone of the cartilage. Grades 2 to 6 OA build on grade 1 and previous grades. They include deep fibrillation, matrix vertical fissures, cartilage erosion and lesion formation extending to the mid and deep zones of the cartilage. Grades 5 and 6 OA include changes to the subchondral bone, such as sclerosis of the

bone plate and microfracture, respectively, because of the complete erosion of the hyaline cartilage followed by deformation of the articular surface (61).

2.3.6 Treatment

Osteoarthritis is managed through the use of non-pharmacological, pharmacological, and/or surgical interventions. These treatments can be combined and are tailored according to the individual needs of the patients (62). Some non-pharmacological interventions include patient-centred education, self-management, exercise, weight loss, encouragement and frequent reassessments (39).

Pharmacological treatments can be administered to target the pain experienced by individuals with OA. Among these are topical and oral NSAIDs (nonsteroidal anti-inflammatory drugs), oral paracetamol (acetaminophen), and intra-articular corticosteroids (39). Topical NSAIDs and oral paracetamol are considered first-line therapies, while oral NSAIDs and intra-articular corticosteroids might be recommended if there is a need for a greater analgesic effect because of their associated toxicities. If non-pharmacological and pharmacological interventions fail, a surgical approach could be recommended (39).

Arthroplasty has been effective in removing OA. However, surgical risks exist, and there have been more favourable outcomes in the elderly population compared to younger patients, who are characterized as < 55 years of age (63). There is a need for developing safe and effective disease-modifying treatments for OA. However, this knowledge gap is correlated with the poor understanding of the disease etiology.

2.3.7 Preclinical Models

Animal models have been used to study OA. While there is no gold standard animal model to mimic the human disease, they have been advantageous in providing insight into both the natural history and treatment response of knee OA (64). Knee OA animal research has included both small and large animal models. Small animal models, such as mice, rats, rabbits and guinea pigs, offer advantages like their relatively short lifespan that allow for complete documentation of their growth and development. However, they can be disadvantageous because their histopathology may look different from that of humans (64). On the other hand, large animal models include dogs, sheep, goats, and horses, which are more likely to have similar histopathology to humans, but it becomes difficult to observe the entire natural history of idiopathic OA.

The availability of state-of-the-art high-resolution imaging modalities, such as high-field MRI and μ CT, has allowed for the evaluation of morphological and biochemical OA changes in small animal models (65). Various guidelines have also been developed to quantify histopathological changes in these models (66). While a vast amount of information exists, the method of OA induction is relevant to distinguish the type of OA being studied. When knee OA is induced through surgical injury to the joint (64), the joint damage following injury likely occurs via a mechanism similar to that of post-traumatic OA in humans. To model human idiopathic knee OA, OA should arise spontaneously without inducing damage in a model that shares similar risk factors as humans with the disease. This means that single-gene knockout mouse models, while useful in highlighting the genetic mechanisms of joint degradation and possible targets for drug development, do not replicate human idiopathic knee OA because there are a lot more genes that contribute to disease pathogenesis that are not targeted in these models (67).

A model that has been used to study idiopathic knee OA for decades is the Dunkin-Hartley guinea pig (3,68). This model appears to spontaneously develop a knee OA-phenotype similar to primary OA in humans because the incidence is associated with increasing age, weight, and mechanical load (3).

2.4 Dunkin-Hartley Guinea Pig

To study the joint tissue changes that lead to knee OA, DH guinea pigs are frequently compared with other guinea pig strains that develop knee OA-like features later in life. These include the Strain 13 (69) and Bristol Strain 2 (BS2) guinea pigs (70). However, this animal model is not without disadvantages. One of them is the absence of a true control because all guinea pigs eventually develop joint degeneration in their lifetime. Also, it is difficult to study the behavioural response to pain in this model. Pain is an important aspect of advanced knee OA but guinea pigs are prey animals evolved to hide their pain from predators making them less than ideal pain models (67). Notwithstanding these disadvantages, some of the risk factors of knee OA observed in humans have been reported in this model (68,71–74).

2.4.1 Risk Factors of Human Knee OA Studied in the DH Guinea Pig

Previous studies have proposed that some risk factors of knee OA in humans may be implicated in the joint degeneration observed in the DH guinea pig (68,71–74). Among these are increasing age, obesity, a varus knee alignment, and joint instability (75–77).

Knee OA is an age-related degenerative disease, and thus age is an important factor in investigating animal models of knee OA. In the DH guinea pig, cartilage and meniscal pathology have been observed to occur in higher severity with increasing age, and histological signs of knee

OA have been reported as early as 3 months (68,69). At 12 months of age, the DH strain had a higher bone turnover and BMD than Strain 13 (69).

The incidence of knee OA in humans has also been correlated with increased weight and obesity. This has also been studied in the DH guinea pig model. One longitudinal study that compared a group of DH guinea pigs fed with standard chow (control) to another that was diet-restricted found that the control group maintained significantly higher body weight and knee degeneration occurred significantly earlier (71). Obesity in the DH guinea pig has been proposed to alter joint architecture, which may increase the loading of the articular cartilage, promoting matrix degradation and chondrocyte apoptosis (72). Compared with Strain 13, DH guinea pigs have a higher average weight in their lifetime, which may be associated with their increased knee OA susceptibility (69).

Altered joint mechanics due to a varus alignment in these animals, where there is increased load sustained by the medial compartment of the knee joint, may have resulted in this compartment becoming more prone to articular cartilage and subchondral bone degenerative changes, according to one study (70). Knee joint instability due to the individual or collective failure of structures responsible for its stability has been proposed to lead to knee OA (77). The meniscus and ligament, among other structures, provide joint stability and have been observed to deteriorate with increasing age in the DH guinea pig (3,73,74). Meniscal degeneration and increased ACL laxity and deterioration in this model have also been correlated with a decrease in joint integrity.

2.4.2 Tissue Changes Related to Risk Factors of Knee OA

Based on the above risk factors, previous studies have documented associated degenerative changes occurring in the subchondral bone, cartilage, meniscus, and ligament of the DH knee joint.

The subchondral bone plays an important role in knee OA onset and progression. Its degenerative changes, such as changes in BMD, bone turnover and remodelling, sclerosis, osteophyte formation, and cysts, are hallmarks of the disease (16,39,78). These hallmarks have been reported in the subchondral bone of DH guinea pigs. Increased subchondral BMD is a suggested predictor of knee OA occurrence in humans (79), but there is a lot of uncertainty concerning its role in the disease process because a decrease in BMD may be associated with cartilage loss (39,80). In the DH guinea pig model, both low and high BMD has been associated with degenerative changes (70,81–84). Compared to Strain 13 and BS2, greater BMD was reported in DH between the ages of 1 and 9 months by some studies, and lower BMD in others at 4, 6, and 12 months. However, these inconsistencies might be due to differences in measurement tools used in these studies. The studies that reported higher BMD used μ CT and dual-energy X-ray absorptiometry (DXA), while those that described lower BMD used tools like the digital X-ray and an X-ray bone densitometer, which may be less sensitive to bone density calculations. Bone turnover also plays an important pathogenic role in knee OA progression. Studies, with the aid of biomarkers and imaging, have linked increases in bone turnover with thickening of the subchondral bone plate and trabecular bone as well as the formation of bone cysts and peripheral osteophytes (70). The amounts of serum osteocalcin, a bone formation biomarker, and urinary N-telopeptide of type I collagen (NTX), a bone resorption biomarker, were found to be higher in the DH guinea pig compared with Strain 13 throughout their lives, indicative of a greater level of subchondral bone turnover and overall bone remodelling in this model (69,85). Several studies have suggested that subchondral bone plate sclerosis in guinea pigs is morphologically similar to that seen in humans (3,82,86). In 22-month-old DH guinea pigs, it was seen as an area of increased density on a radiograph (87). Osteophytes

have occurred in 9-month-old DH guinea pigs and became larger at older ages (81). Subchondral cysts have been reported in the DH guinea pig knee joint as early as 6 months of age (3,88).

Cartilage changes are a big part of the degenerative changes in knee OA. They include cartilage swelling, degradation, fibrillation, lesions, as well as chondrocyte apoptosis and hypertrophy. Cartilage swelling is a hallmark of human OA, and it has been observed in the DH guinea pig model between 2 and 6 months of age using MRI (72,89). Another study found cartilage swelling surrounding the medial tibial plateau at 3 months of age (3). Cartilage degradation, a key aspect of human knee OA progression, has been reported in the DH guinea pig as early as 3 months of age (68). Studies observed cartilage degradation to progress as the guinea pigs age, indicating severe damage and absence in areas at 16 to 18 months (87,88). Fibrillations in the cartilage are apparent changes that present as superficial fissuring on the cartilage surface (58). Studies have found prominent fibrillation in the middle zone of the medial tibial plateau by 5 months of age, with a 100% incidence by 8 months (83,85,90). Within 8 to 12 months, studies have observed fibrillation encompassing the deep zone of the medial tibial plateau and the femoral condyle (81,85,91). There are reports of cartilage lesions in this model on MR images. They initially appear on the medial compartment of the knee at approximately 6 to 9 months, corresponding with the varus joint alignment of DH guinea pigs (3,81,91,92). Lesions on the lateral compartment occur later, between 10 and 12 months of age (68). During OA progression in humans, chondrocytes may become hypertrophic and undergo cell death or apoptosis (93). Significant chondrocyte apoptosis in the medial articular cartilage was observed in DH guinea pigs between 6 and 7.5 months in one study (70). Another study documented an increase in the severity of chondrocyte apoptosis in this model by 12 months (68). Hypertrophic articular chondrocytes in the DH guinea pig have been seen as early as 6 months (81).

Damage to the meniscus, which is among multiple anatomic structures that provide joint stability, may lead to a degenerative joint disease like knee OA in humans (94). In the DH model, joint areas not covered by menisci were observed to have increased cartilage fragmentation, cartilage lesions and epiphyseal bone cysts at 9 months (3). Upon histological analysis in this same study, meniscal degeneration began at 3 months, and meniscal ossification occurred between 3 and 12 months (3). Another study has correlated meniscus mineralization to defective joint load transmission, shock absorption, and stability in this model (95). Meniscus mineralization has also been associated with cartilage degeneration and is reported to increase with age in the DH guinea pig (72,84,85). Specifically, one study noted meniscus mineralization between the ages of 3 and 12 months (67). Lastly, older guinea pigs, 17 to 37 months, had osteophytes on the edge of their mineralized menisci (96).

Anterior cruciate ligament deterioration and elevated laxity have been suggested as relevant factors to consider in primary human knee OA, even though this has been mostly studied in post-traumatic knee OA (73). In the DH guinea pig, evidence of ACL deterioration and increased laxity have been reported (73,74). Compared to age-matched BS2 controls, DH guinea pigs had higher ACL laxity (73). This study also revealed higher collagen turnover and ligament remodeling at the ages (2 to 4 months), where the DH guinea pigs had more lax ACL. The DH guinea pigs also formed osteophytes after ligament dysfunction was observed, suggesting that ACL deterioration may trigger other knee OA-related changes.

2.4.3 Knee OA Assessment in the DH Guinea Pig

Knee OA in the DH guinea pig has been studied with imaging and histological techniques. These techniques allow for qualitative, quantitative and semi-quantitative assessment of the disease-related changes. Qualitative assessments have involved the documentation of gross morphology changes from MRI and/or μ CT-obtained images as well as photomicrographs (3,69,81). Common quantitative assessment techniques used in a high-resolution μ CT system are bone microarchitecture analysis, which involves the quantification of properties of the subchondral bone plate, cortical bone and trabecular bone (97). Quantitative analyses with MRI involve measurements of cartilage thickness and volume (86). Lastly, semi-quantitative assessments are grading or scoring systems specifically designed to evaluate pathological changes in the knee joint. These assessments could be based on imaging and/or histological data, like MOAKS with MRI and the Mankin score with histology. One example is the Rat Arthritis Knee Scoring System (RAKSS), which uses CT, MRI and histology to score knee OA in the rat model, but can be altered for use in the DH guinea pig (98).

2.5 Summary

The knee joint undergoes a slow process of degeneration during idiopathic OA. Medical imaging and histology have allowed for the timely characterization of the associated degenerative changes. However, in humans, the natural history of slowly progressive idiopathic OA has been difficult to document. The availability of the DH guinea pig, a small animal model that spontaneously develops knee OA, offers hope to understanding the natural history of knee OA and the etiology of BMLs, an important finding associated with the pain seen in the disease.

Chapter 3: Age-related Joint Degeneration in the Dunkin-Hartley Guinea Pig: Joint Assessments with Micro-computed Tomography, MRI and Histology

3.1 Introduction

Knee osteoarthritis (OA) is a degenerative disease that affects the entire synovial joint. There is currently no cure, and treatments have been primarily focused on alleviating the pain associated with the disease. OA is characterized by the radiographic evidence of joint space narrowing and bone anomalies, such as subchondral bone sclerosis, osteophyte formation, and bone cysts (3). However, these characteristics are poorly associated with pain (5). An additional attribute of OA is the presence of bone marrow lesions (BMLs) in MRIs. BMLs are identified by a diffuse hyperintense signal on fluid-sensitive magnetic resonance sequences, such as the fat-suppressed T2-weighted and short tau inversion recovery (STIR) sequences (6). BMLs have been associated with pain in OA, but their role in OA pathogenesis remains unknown (2,40).

Previous studies have found that BMLs typically occur in the weight-bearing regions of the joint and are associated with histological abnormalities, such as adipocyte necrosis, bone marrow fibrosis, trabecular abnormalities like subchondral cysts, and bone microarchitecture alterations (6,7). Of particular interest is that BMLs can progress to subchondral cysts, and both appear bright on fluid-sensitive MR sequences as features, although cysts have well-circumscribed margins (8,99). If BMLs can occur as precystic lesions, these two features may play similar roles in the disease progression.

Currently, there is inconclusive evidence on the relationship between cysts and pain (8,100). However, unlike BMLs, cysts can be visualized radiographically as cavities in the trabecular bone and have two proposed theories on their origin (8,43). The synovial fluid intrusion theory states that cysts form due to raised intraarticular pressure that causes leakage of synovial fluid in the bone through fissures or breaks in the cartilage (8). In contrast, the bone contusion theory explains that cysts occur as a result of bone necrosis induced by abnormal mechanical stress and subsequent microfracture (8,42). Findings in support of the synovial fluid intrusion theory would show cysts only in areas of the bone with complete cartilage loss or fissuring, while those in support of the bone contusion theory would show cysts formed in the weight-bearing regions of the joint, with BMLs preceding them (8,9). Differentiating between these theories will provide insight into whether cysts and BMLs play similar roles in OA pathogenesis. In addition, this information may provide a target to focus future pain research and treatments.

In order to understand the disease processes that may coincide with the onset and progression of BMLs in the context of idiopathic OA, we chose the Dunkin-Hartley (DH) guinea pig that spontaneously develops a knee OA phenotype similar to idiopathic OA observed in humans within a shorter time frame (3,68,101), including a single report of BMLs (88). Therefore, the purpose of this study is to add to this limited knowledge by characterizing the development of BMLs and cysts in the DH guinea pig to understand their etiology and role in knee OA progression. To address this, we aim to document the natural history of OA-related joint degeneration in the DH guinea pig and study the development of BMLs and cysts with complementary information from MRI, μ CT, and histology.

3.2 Methods

3.2.1 Ethics Statement

This study was approved by the University of Calgary Health Sciences Animal Care Committee (ethics protocol #AC17-0206). All animal work was done in full compliance with the Canadian Council on Animal Care guidelines.

3.2.2 Sample Collection

Thirty DH guinea pigs (14 males and 16 females) were purchased from Charles River Laboratories (Saint-Constant, Quebec, Canada) and housed in age and sex-matched pairs at the University of Calgary Health Sciences Animal Resources Centre and the Veterinary Sciences Research Station. The guinea pigs were 2, 4, 6, 12, and 24 months of age at euthanasia. The animals were anesthetized with 5% isoflurane inhalation and euthanized by sodium pentobarbital injection via the intracardiac route. Upon euthanasia, the animals were weighed, and their left hindlimbs were dislocated at the femoral head and excised. The knees were left intact, and the surrounding tissue was carefully trimmed to avoid disturbing the joint capsule. The joints were transferred to 15 mL falcon tubes containing Fluorinert™ FC-770 (Sigma-Aldrich) in preparation for MR scanning.

3.2.3 Magnetic Resonance Imaging

The 2, 4, and 24-month old knee joints were scanned on a 9.4 T MRI with a cryoprobe (Magnex and Bruker). On this scanner, T2 FLASH (Fast Low Angle Shot) scans with and without fat suppression were acquired. On a 1.0 T MRI (Bruker), 6 and 12-month old knees were scanned using the STIR sequence. Table 1 outlines the MRI acquisition parameters.

Table 1. Summary of MR sequences and their scan acquisition parameters.

MRI	Sequences	Scan Acquisition Parameters
9.4 T	T2 FLASH	TE = 6.5 ms TR = 1500 ms Flip angle = 60° Voxel volume = 0.038 mm x 0.038 mm x 0.500 mm Scan time = 25 minutes and 36 seconds
1.0 T	STIR	TE = 25.29 ms TR = 5000 ms TI = 155 ms Voxel volume = 0.098 mm x 0.098 mm x 1.250 mm Scan time = 1 hour and 46 minutes

3.2.4 Micro-computed Tomography and Bone Microarchitecture Analysis

Micro-computed tomography scans were acquired using the VivaCT 40 (Scanco Medical) with resolutions of 10.5 and 15 μm (for 24-month old samples). The energy, current, and power of the x-ray tube were set at 55 kVp, 72 mA, and 4 W, respectively. The integration time was 250 ms and the scan time was 46 minutes. Image processing was done with IPL (Image Processing Language, Scanco Medical). This involved Gaussian filtering and a semi-automatic segmentation pipeline ($\sigma = 1.2$, support = 2, lower threshold = 500 mgHA/cm³, upper threshold = 3000 mgHA/cm³) that isolated the femoral and tibial epiphyses, and separated their periosteal and endosteal surfaces for independent analyses (10,11). Manual selection of the joint compartments (medial, lateral) in the weight-bearing regions of the femur (Figure 4A) and tibia (Figure 4B) were done using BIsurfaceViewer (Bone Imaging Laboratory, University of Calgary) (11). The central region was defined as the region between the medial and lateral regions. A bone morphometry analysis script was run on the medial, lateral, and central epiphyseal regions (Figure 5) to produce

quantitative outcomes, including subchondral bone plate thickness (Sbp.Th, mm), subchondral bone plate porosity (Sbp.Po, %), and trabecular BMD (Tb.BMD, mgHA/cm³), bone volume fraction (Tb.BV/TV, %), thickness (Tb.Th, mm), number (Tb.N, mm⁻¹) and separation (Tb.Sp, mm), on all three joint compartments across femora and tibiae.

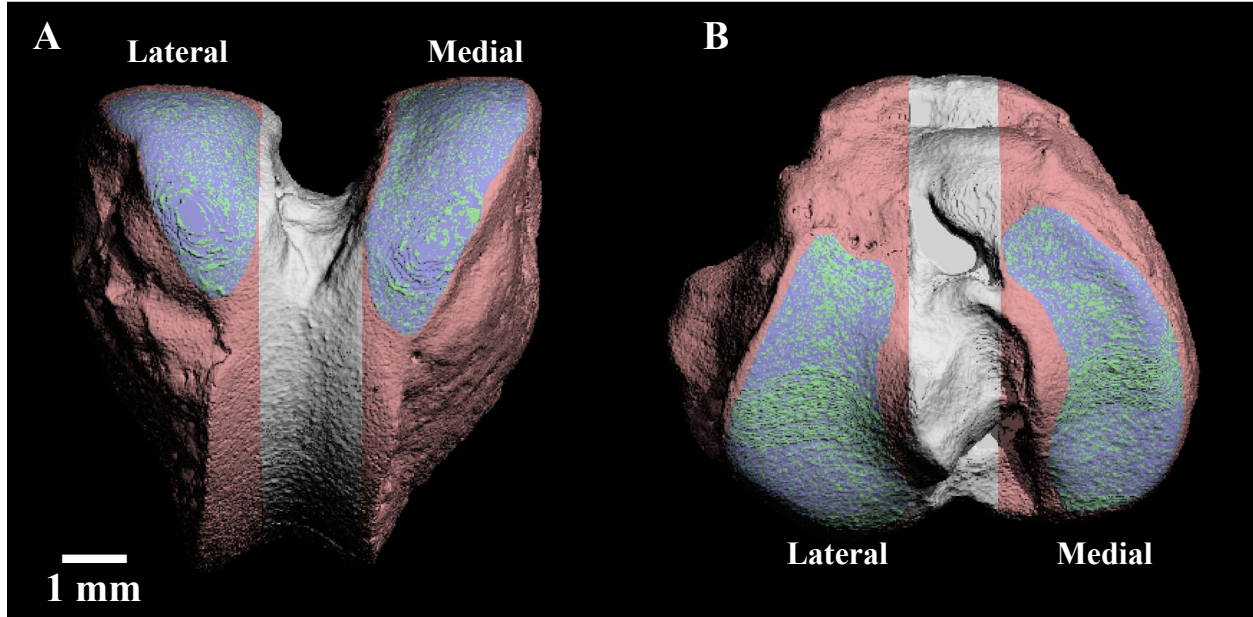


Figure 4. An overlay of medial and lateral weight-bearing regions (purple) on the left (A) femur and (B) tibia from a DH guinea pig. The central region is between the medial and lateral regions.

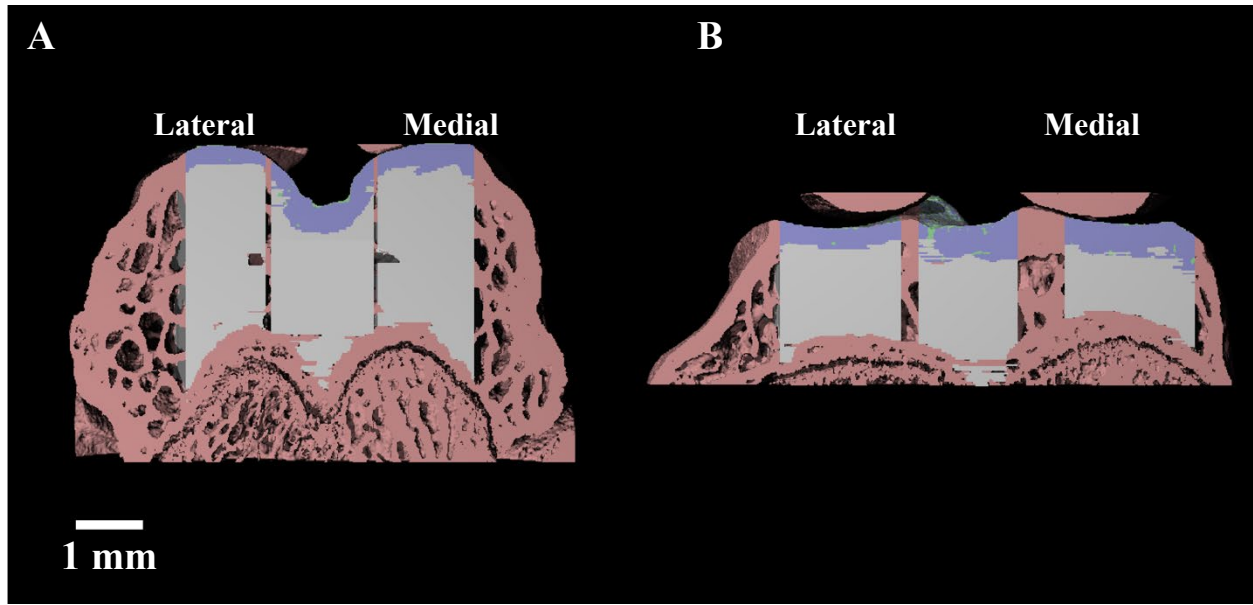


Figure 5. Masked regions of the femur (A) and tibia (B) indicating the areas of the cortical plate (purple) and trabecular bone (grey) that were included in the bone microarchitecture analysis.

3.2.5 Rat Arthritis Knee Scoring System (RAKSS)

RAKSS (98) was modified to semi-quantitatively analyze only bony features from μ CT images, including osteophytes, subchondral sclerosis, bone cysts and loose bodies (Table 2). Across femora and tibiae, osteophytes were scored on eight regions, the anterior and posterior medial and lateral locations for each bone, using a ruler tool on image slices in the μ CT Evaluation Program V6.6 (Scanco Medical). Sclerosis was scored based on the quantitative bone microarchitecture outcome, maximum Sbp.Th (mm) in four regions, the medial and lateral femur and tibia. The maximum depth of a subchondral bone plate without sclerosis was set at 0.44 mm, as calculated by the median maximum Sbp.Th on DH guinea pigs with no visible sclerosis on their μ CT images. Bone cysts were scored as present or absent in the femur and tibia. Lastly, the number of calcified loose bodies surrounding the knee joint was scored by count.

Table 2. Modified rat arthritis knee scoring system (RAKSS). Osteophytes are scored in 8 regions (anterior and posterior medial and lateral locations for femur and tibia each), and sclerosis is scored in 4 regions (medial and lateral tibia and femur). Adapted from (98).

Bony Feature	Grade [0–33]
Osteophyte (scored in 8 regions)	Grade [0–16]
None/Possible (from osteophyte to cortex ≤ 0.2 mm)	0
Definite ($0.2 \text{ mm} < \leq 0.5$ mm)	1
Large (> 0.5 mm)	2
Subchondral Sclerosis (scored in 4 regions)	Grade [0–12]
Maximum Subp.Th Without Sclerosis ≤ 0.44 mm	0
$0.44 \text{ mm} < \leq 0.65$ mm	1
$0.65 \text{ mm} < \leq 1$ mm	2
> 1 mm	3
Bone Cysts (scored in tibia and femur)	Grade [0–2]
None	0
Present	1
Loose Bodies	Grade [0–3]
None	0
Number of Bodies = 1	1
Number of Bodies = 2	2
Number of Bodies ≥ 3	3

3.2.6 Histology

Tibiofemoral joints were fixed in 10% neutral buffered formalin (ThermoFisher Scientific) for five days. Following fixation, samples were decalcified in Cal-Ex[®] II (ThermoFisher Scientific) for four weeks, then transected sagittally into medial and lateral compartments. Medial and lateral samples were embedded in paraffin wax (50% Paraplast plus/50% Paraplast extra), and 15

µm-thick sections were obtained in the sagittal plane with a microtome (Leica RM2255). Sections were stained with hematoxylin-eosin (H&E) and toluidine blue histological stains, then imaged with a digital microscope slide scanner (ZEISS Axio Scan.Z1).

3.2.7 Visual Assessments

STIR and T2 images were visually assessed; the number of hyperintensities, whether the hyperintensities were consistent with the definitions of BMLs or cysts, and their anatomical locations in the knee joint, were recorded. On MRI, BMLs were defined as diffuse hyperintense regions, while cysts were defined as well-delineated hyperintense regions. For subchondral cysts, the well-delineated hyperintense regions on MRI had to correspond to bone cavities on µCT and histology sections. On histology sections, BMLs were defined as regions with adipocyte necrosis and fibrosis. Anomalies including cysts, sclerosis, and osteophytes in µCT images and H&E stained sections were also documented. The cartilage structure in the toluidine blue-stained sections of DH guinea pigs with bone defects were assessed.

3.2.8 Statistical Analysis

All statistical analyses were conducted with IBM SPSS Statistics version 26 (IBM Corp., Armonk, NY). The Shapiro-Wilks test was used to test for normality of the data. Two-way ANOVAs were performed to compare differences in bone microarchitecture data across age groups and joint compartments, with post-hoc simple effects testing when main effects or interactions were significant. Bonferroni adjustments were included in the simple effects analysis to account for multiple comparisons. Skeletally immature age populations (2 and 4 months) were excluded from all bone microarchitecture statistical analyses (n = 20). The results are presented as mean +/- SE

unless otherwise indicated. The total semiquantitative RAKSS scores were compared across age groups using a Kruskal-Wallis nonparametric test with multiple pairwise comparisons. The significance level was set at $p < 0.05$.

3.3 Results

Dunkin-Hartley guinea pigs were grouped by age and their physical characteristics, including their sample sizes, sexes, weight, and whether they were skeletally mature according to the state of their growth plates (102). This information is recorded in Table 3.

Table 3. Animal characterization by age, sample size, weight, and level of skeletal maturity.

	2 months	4 months	6 months	12 months	24 months
Number of animals	2	8	8	8	4
Number of males	0	4	4	4	2
Number of females	2	4	4	4	2
Mean weight \pm S.E. (g)	424 \pm 10	689 \pm 31	804 \pm 37	1141 \pm 74	990 \pm 54
Growth plate	Unfused	Unfused	Partially fused	Fused with remnants	Completely fused

3.3.1 MRI Hyperintensities

The T2 and STIR MR images of all guinea pig age groups showed varying degrees of hyperintensities in their tibiofemoral joints at 6, 12 and 24 months (Figure 6). All hyperintense regions had well-delineated margins. A count and matching of these hyperintense regions to complementary μ CT images revealed that the 6 months and older age groups have cavities in their

trabecular bone that are correlated with hyperintensities (Table 4) that match the definition of subchondral cysts (Figure 7). These cysts were primarily located in the central compartment and largest in the 24-month-old guinea pigs.

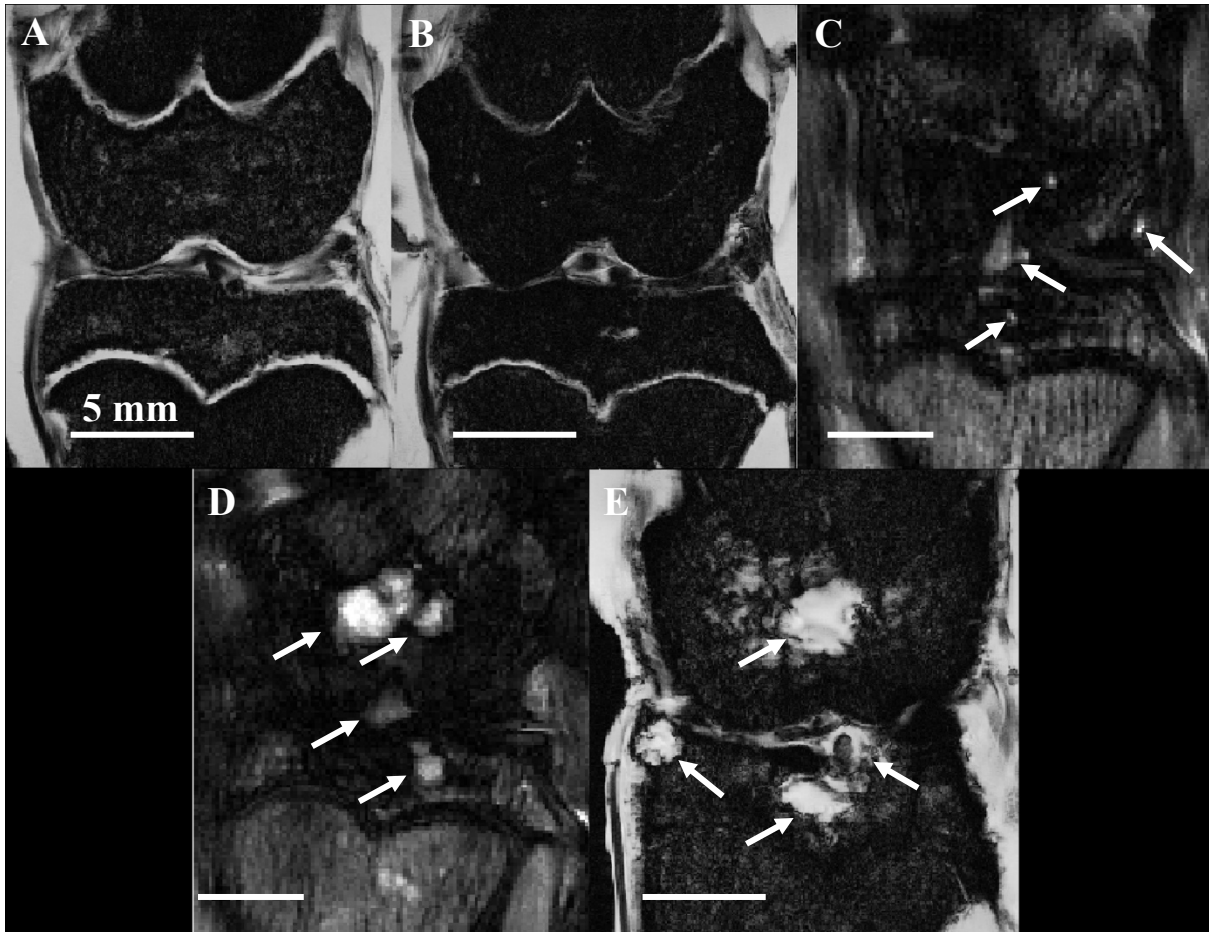


Figure 6. Coronal MR images of DH guinea pig tibiofemoral joints at 2, 4, 6, 12, and 24 months. T2 FLASH with fat suppression images at ages 2 (A) and 4 months (B). (C) STIR image of a 6-month-old with hyperintensities in the lateral femur, central femoral and tibial epiphyses, and ACL. (D) STIR image of a 12-month-old with two hyperintensities in the central femoral epiphysis, one in the tibial epiphysis, and another in the joint space. (E) T2 FLASH image of a 24-month-old with an even larger hyperintensity in the central femoral epiphysis, two in the tibia, and one in the joint space. White arrows indicate hyperintensities.

Table 4. Description of the hyperintense regions observed on MRI in different DH guinea pig age groups according to their mean count, anatomical locations, whether they are bone changes and match BML or cyst definitions.

Age (Months)	Mean \pm SD Hyperintensity Count	Anatomical Locations of Hyperintensity	# of Bone Changes Corresponding to Hyperintensity	Matching BML or Cyst Definition?
2	1 \pm 0	Joint space	0	Cyst due to well-delineated margins
4		N/A due to fat suppression inconsistencies		
6	3 \pm 1	Central femoral epiphysis, joint space, central tibial epiphysis	2	Cyst due to well-delineated margins. Corresponds to bone cavity if located in trabecular bone
12	4 \pm 1	Central femoral epiphysis, joint space, central tibial epiphysis. Can appear more than once in any of the three locations	3	Cyst due to well-delineated margins. Corresponds to bone cavity if located in trabecular bone
24	4 \pm 1	Central femoral epiphysis, joint space, central tibial epiphysis, osteophyte. Can appear more than once in any of the three locations	3	Cyst due to well-delineated margins. Corresponds to bone cavity if located in trabecular bone

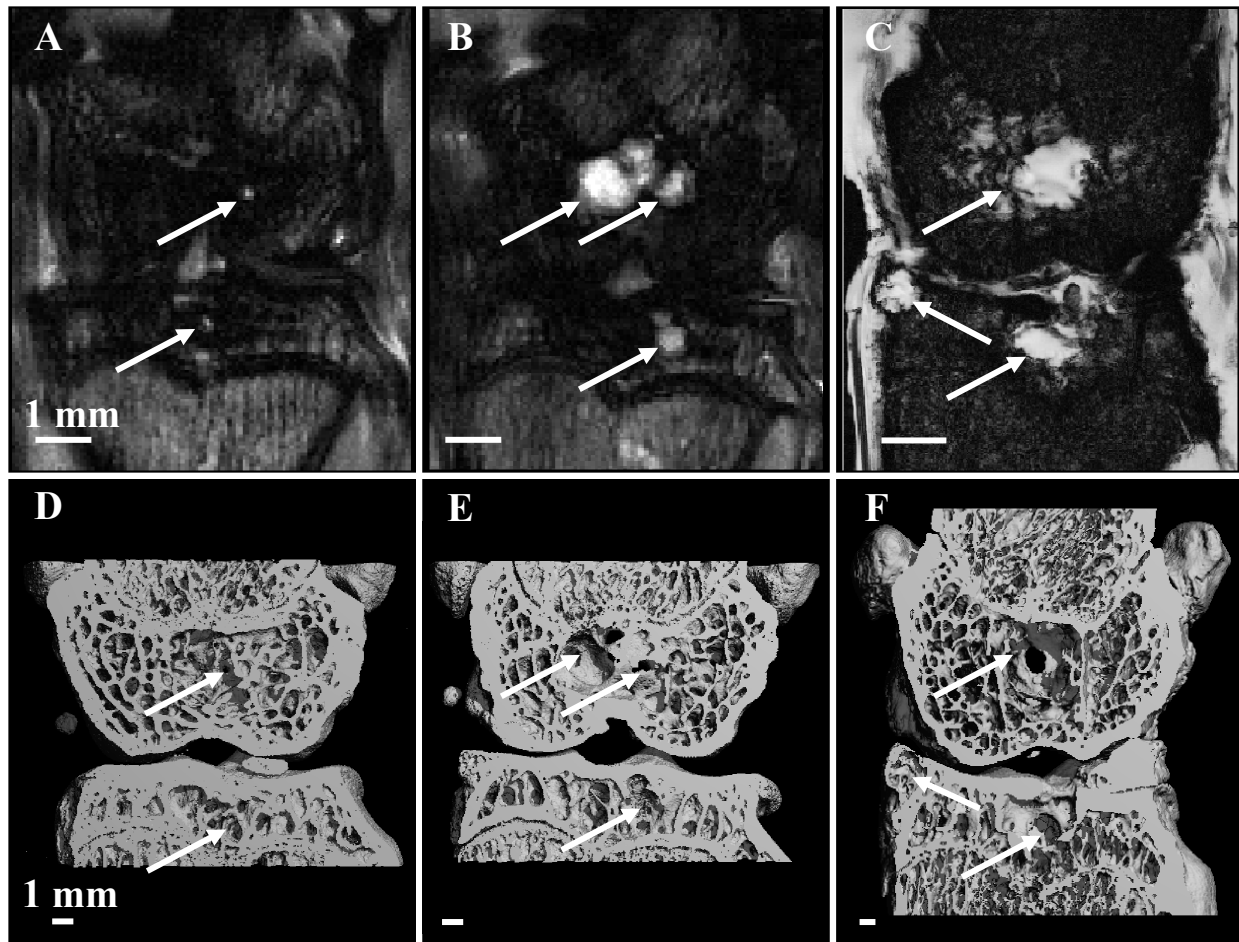


Figure 7. Fluid-sensitive MR (A, B, C) and complementary μ CT (D, E, F) images of guinea pig tibiofemoral joints at ages 6 (A, D), 12 (B, E) and 24 (C, F) months. White arrows indicate cysts as defined by hyperintensities on fluid-sensitive MRI and corresponding cavities in the trabecular bone.

3.3.2 RAKSS

The median RAKSS scores are reported in Table 5. Osteophytes, sclerosed bone, cysts and loose bodies were predominantly present in the 6, 12 and 24-month age groups. The Kruskal-Wallis H test showed a statistically significant difference in total RAKSS score between age

groups ($n = 30$, $H = 16.67$, $p = 0.002$). Pairwise comparisons showed significant differences in total RAKSS score between the younger ages, 2 and 4 months, and the older ages, 6, 12 and 24 months. The 6, 12 and 24-month age groups did not differ significantly in total RAKSS scores with each other.

Table 5. Median (interquartile range) of RAKSS scores based on μ CT bony features. Different letters (^{a,b}) indicate significant differences in total RAKSS score (Kruskal-Wallis test and subsequent pairwise multiple comparisons, $p < 0.05$).

Feature [Grade]	2 months	4 months	6 months	12 months	24 months
Osteophyte [0–16]					
Femur [0–8]	0 (0 – 0)	0 (0 – 0)	0 (0 – 1)	1 (0 – 1)	3 (1 – 3)
Tibia [0–8]	0 (0 – 0)	0 (0 – 0)	0 (0 – 0)	0 (0 – 3)	5 (1 – 5)
Total [0–16]	0 (0 – 0)	0 (0 – 0)	0 (0 – 1)	1 (0 – 5)	7 (2 – 8)
Sclerosis [0–12]					
Femur [0–6]	1 (0 – 1)	2 (1 – 2)	2 (2 – 3)	2 (2 – 2)	3 (2 – 4)
Tibia [0–6]	0 (0 – 0)	0 (0 – 2)	2 (1 – 2)	2 (2 – 2)	2 (1 – 2)
Total [0–12]	1 (0 – 1)	2 (1 – 4)	4 (3 – 5)	4 (3 – 4)	5 (4 – 5)
Bone cysts [0–2]					
Femur [0–1]	1 (1 – 1)	1 (1 – 1)	1 (1 – 1)	1 (1 – 1)	1 (1 – 1)
Tibia [0–1]	0 (0 – 0)	0 (0 – 0)	1 (0 – 1)	1 (0 – 1)	1 (0 – 1)
Total [0–2]	1 (1 – 1)	1 (1 – 1)	2 (1 – 2)	2 (1 – 2)	2 (1 – 2)

Table 5. (Continued)

Feature [Grade]	2 months	4 months	6 months	12 months	24 months
Loose bodies [0–3]					
Total	0 (0 – 0)	0 (0 – 1)	3 (1 – 3)	2 (1 – 3)	2 (1 – 3)
Total RAKSS [0–33]	2 (1 – 2) ^b	3 (2 – 6) ^b	8 (7 – 10) ^a	9 (7 – 13) ^a	15 (9 – 17) ^a

3.3.3 Bone Microarchitecture

The two-way ANOVA test conducted to examine the differences in maximum femoral Sbp.Th across age groups and joint compartments revealed a statistically significant interaction between age and joint compartment ($F = 4.561$, $p = 0.013$). Additional analysis showed that age had a statistically significant simple effect on maximum femoral Sbp.Th in the medial joint compartment ($F = 11.08$, $p = 0.001$) (Figure 8A). In this compartment, the mean maximum femoral Sbp.Th was highest in the 24-month age group, followed by the 6 and 12-month groups. On the other hand, joint compartment had statistically significant simple effects in the 6 ($F = 3.675$, $p = 0.049$) and 24-month ($F = 20.43$, $p < 0.001$) age groups. In both age groups, the medial compartment had a greater mean maximum femoral Sbp.Th than the lateral compartment.

In the tibia, the maximum Sbp.Th two-way ANOVA results revealed no significant interaction between age and joint compartment ($F = 1.229$, $p = 0.317$). Age had no significant main effect on maximum tibial Sbp.Th ($F = 0.515$, $p = 0.607$) (Figure 8B). In contrast, joint compartment had a statistically significant main effect on maximum tibial Sbp.Th ($F = 13.46$, $p < 0.001$). The estimated marginal means results for joint compartment showed that the medial compartment (0.528 ± 0.021 mm) had a higher mean Sbp.Th than the lateral compartment (0.306 ± 0.011 mm).

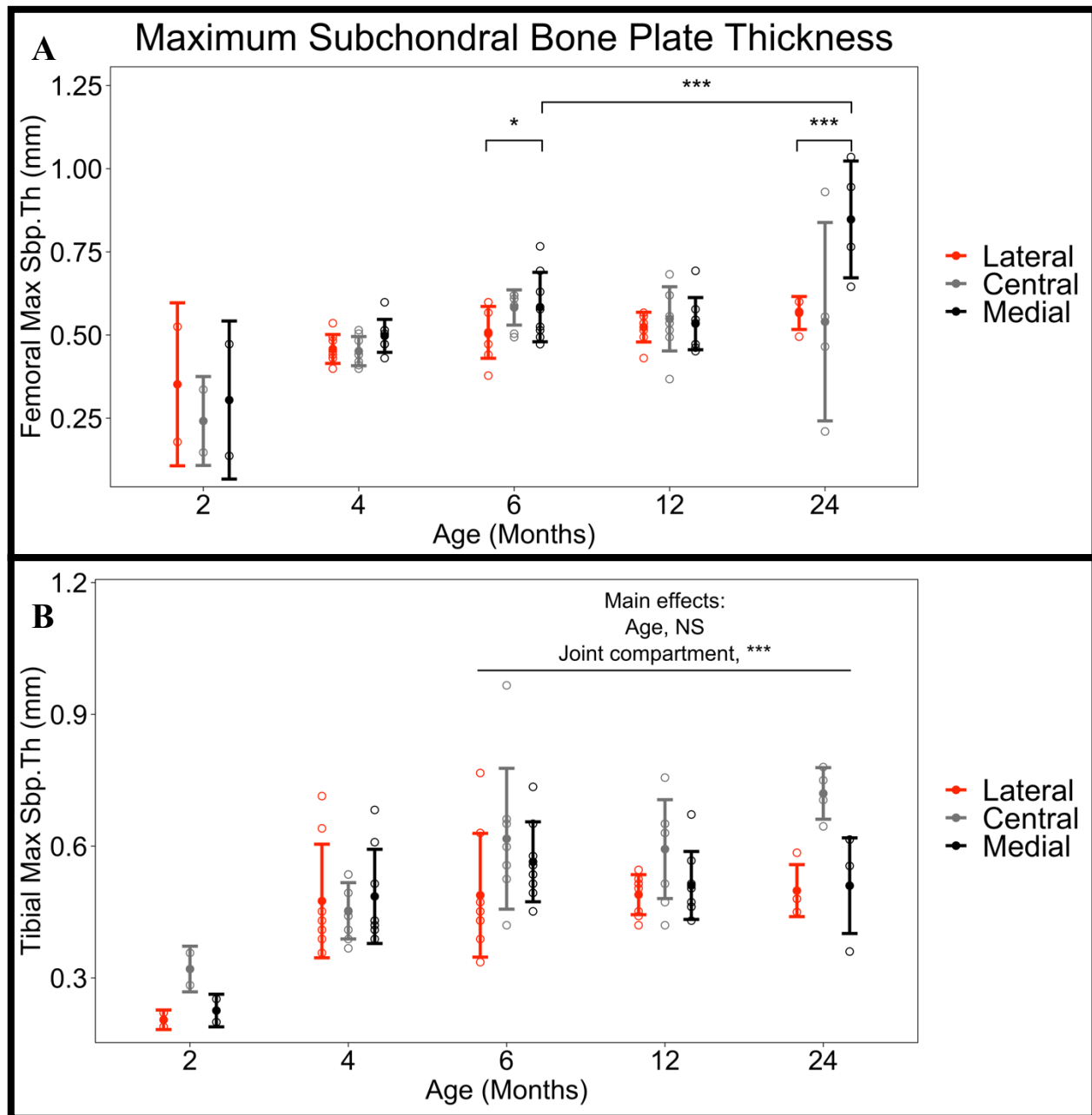


Figure 8. Maximum subchondral bone plate thickness (mm) in the lateral, central and medial compartments of the (A) femur and (B) tibia plotted across DH guinea pig age groups. Data points represent individual animals. Mean \pm SD maximum Sbp.Th for age groups are indicated by the full circles and error bars, respectively. Simple effects results from the two-way ANOVA tests are represented in (A), where * and *** mean $p < 0.05$ and $p \leq 0.001$, respectively. Main effects results are represented in (B), where NS and *** mean $p > 0.05$ and $p \leq 0.001$, respectively.

The femoral Sbp.Po results revealed a significant interaction between age and joint compartment ($F = 4.819$, $p = 0.003$). Age had statistically significant simple effects in the medial ($F = 7.758$, $p = 0.004$), lateral ($F = 5.709$, $p = 0.013$), and central ($F = 10.21$, $p = 0.001$) joint compartments (Figure 9A). In all three compartments, the mean femoral Sbp.Po was highest in the 24-month age group, followed by the 6 and 12-month groups. Joint compartment had statistically significant simple effects in the 6 ($F = 8.424$, $p = 0.003$), 12 ($F = 4.089$, $p = 0.037$) and 24-month ($F = 31.68$, $p < 0.001$) age groups. The mean femoral Sbp.Po was higher in the medial compartment for the 12 and 24-month age groups when compared with the lateral compartment, while the 6-month group had a higher mean femoral Sbp.Po in the lateral compartment.

Regarding tibial Sbp.Po, there was no significant interaction between age and joint compartment ($F = 1.408$, $p = 0.252$). Both age ($F = 18.64$, $p < 0.001$) and joint compartment ($F = 5.867$, $p = 0.006$) had statistically significant main effects on tibial Sbp.Po (Figure 9B). The estimated marginal mean Sbp.Po was highest in 24-month age group (1.600 ± 0.100 %) and lowest in the 12-month group (0.400 ± 0.100 %). The medial compartment had a lower estimated marginal mean Sbp.Po (0.700 ± 0.100 %) than the lateral compartment (0.800 ± 0.100 %).

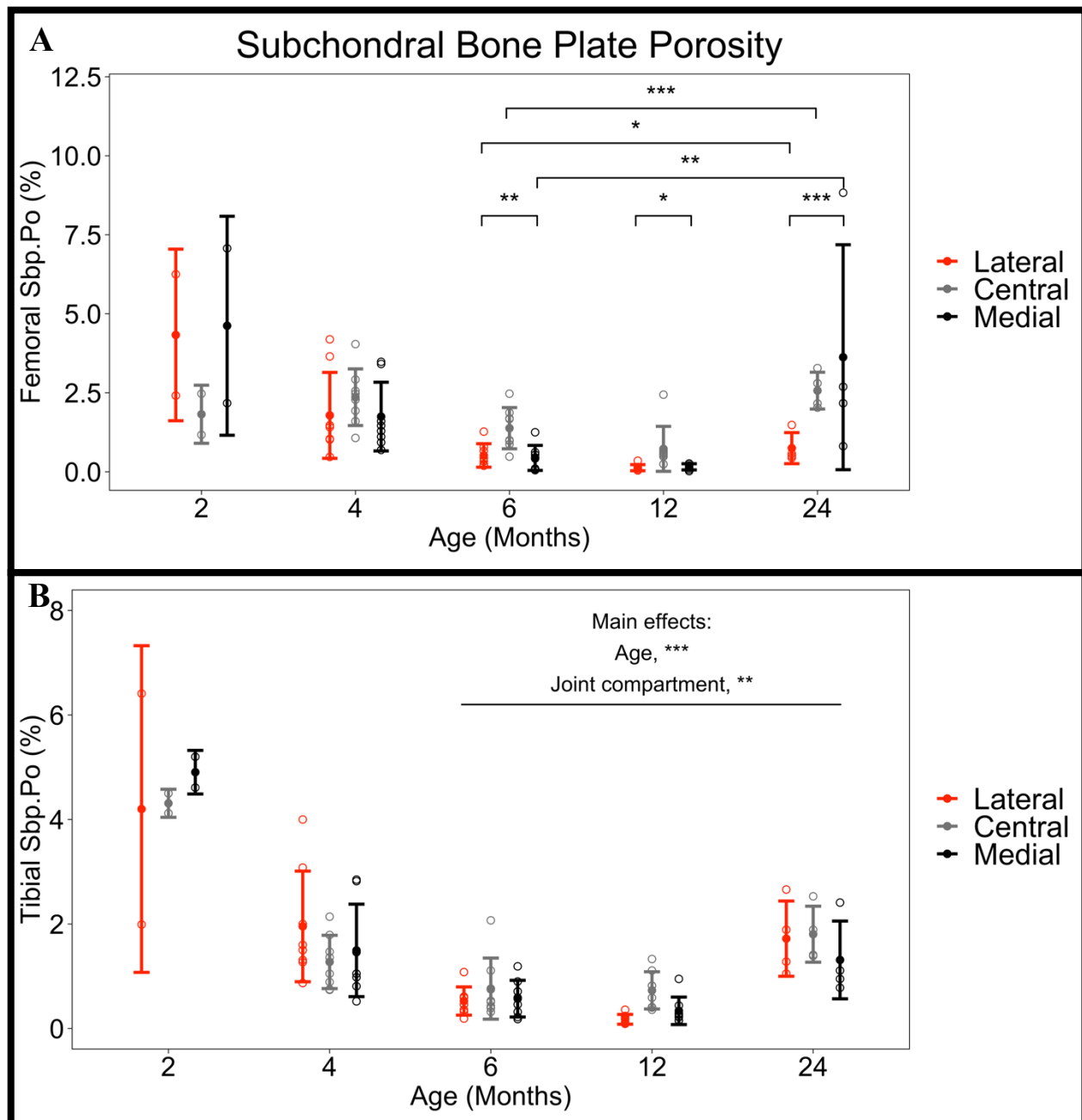


Figure 9. Subchondral bone plate porosity (%) in the lateral, central and medial compartments of the (A) femur and (B) tibia plotted across DH guinea pig age groups. Data points represent individual animals. Mean \pm SD Sbp.Po for age groups are indicated by the full circles and error bars, respectively. Simple effects results from the two-way ANOVA tests are represented in (A), where *, **, and *** mean $p < 0.05$, $p \leq 0.01$, $p \leq 0.001$, respectively. Main effect results are represented in (B), where ** and *** mean $p \leq 0.01$ and $p \leq 0.001$, respectively.

For femoral Tb.BMD, there was no significant interaction between age and joint compartment ($F = 0.644$, $p = 0.635$). Age had no significant main effect on femoral Tb.BMD ($F = 3.253$, $p = 0.064$), while joint compartment did have a significant main effect ($F = 10.88$, $p < 0.001$) (Figure 10A). The estimated marginal means results for joint compartment showed that the medial compartment (496.1 ± 11.5 mgHA/cm³) had a higher mean femoral Tb.BMD than the lateral compartment (467.9 ± 23.4 mgHA/cm³).

On the other hand, the tibial Tb.BMD results had a statistically significant interaction between age and joint compartment ($F = 3.976$, $p = 0.009$). Additional analysis revealed that age had statistically significant simple effects in the lateral ($F = 8.992$, $p = 0.002$) and central ($F = 3.605$, $p = 0.050$) joint compartments (Figure 10B). Within the lateral compartment, the 24-month age group had the lowest mean tibial Tb.BMD, followed by the 6 and 12-month groups. Within the central compartment, the 24-month age group also had the lowest mean tibial Tb.BMD, but it was followed by the 12-month group. Joint compartment had statistically significant simple effects in the 6 ($F = 109.1$, $p < 0.001$), 12 ($F = 162.9$, $p < 0.001$) and 24-month ($F = 73.21$, $p < 0.001$) age groups. In the three age groups, the medial compartment had a higher mean tibial Tb.BMD than the lateral compartment.

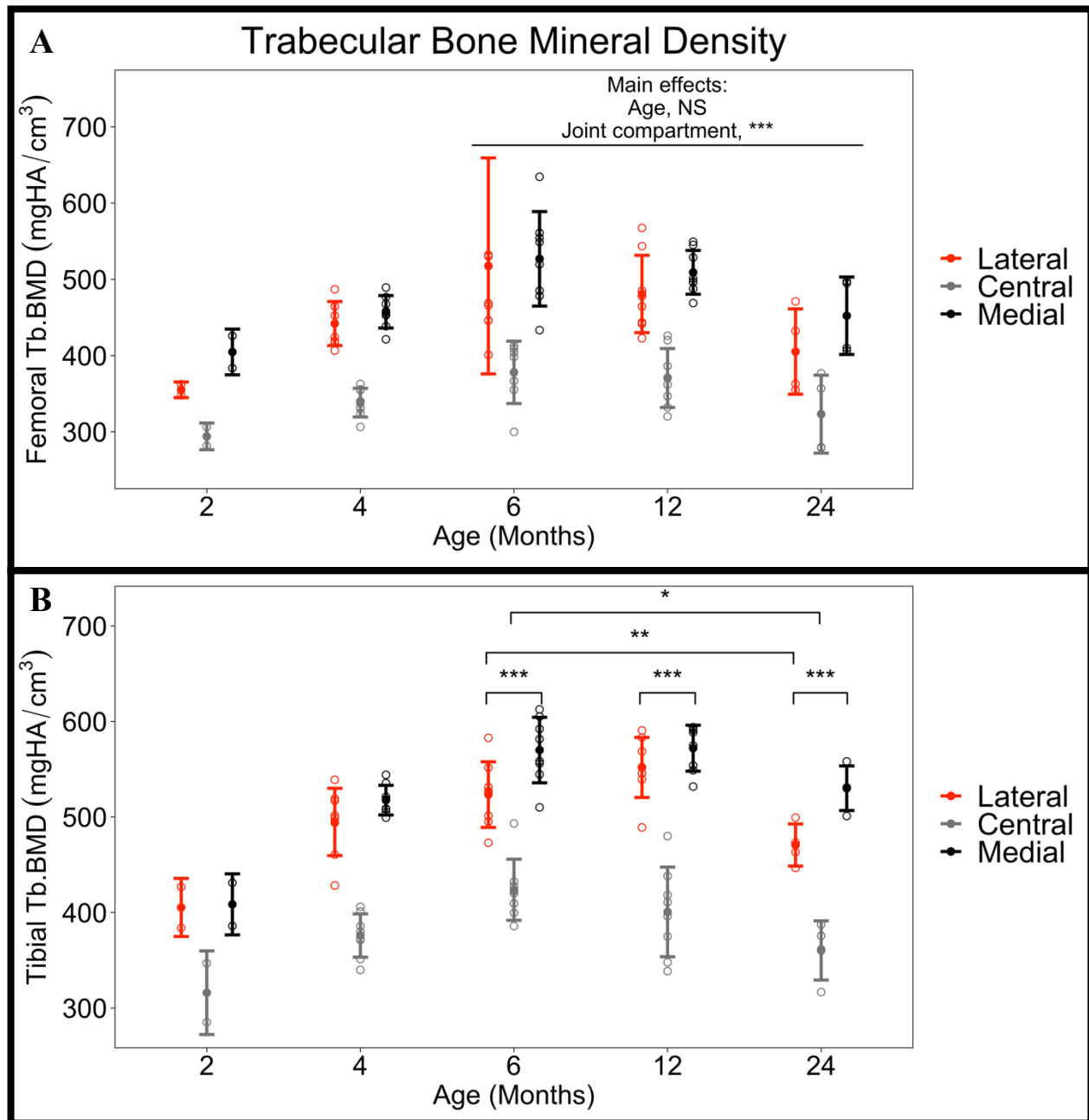


Figure 10. Trabecular bone mineral density (mgHA/cm³) in the lateral, central and medial compartments of the (A) femur and (B) tibia plotted across DH guinea pig age groups. Data points represent individual animals. Mean \pm SD Tb.BMD for age groups are indicated by the full circles and error bars, respectively. Main effect results from the two-way ANOVA test are represented in (A), where NS and *** mean $p > 0.05$ and $p \leq 0.001$, respectively. Simple effects results are represented in (B), where *, **, and *** mean $p < 0.05$, $p \leq 0.01$, and $p \leq 0.001$, respectively.

The femoral Tb.BV/TV results revealed no significant interaction between age and joint compartment ($F = 0.860$, $p = 0.498$). The main effect of age on femoral Tb.BV/TV was not statistically significant ($F = 3.365$, $p = 0.059$), while the main effect of joint compartment was significant ($F = 234.5$, $p < 0.001$) (Figure 11A). The estimated marginal means results for joint compartment showed that the medial compartment ($45.90 \pm 1.00\%$) had a higher mean femoral Tb.BV/TV than the lateral compartment ($41.70 \pm 1.20\%$).

In contrast, the tibial Tb.BV/TV results revealed a significant interaction between age and joint compartment ($F = 4.360$, $p = 0.006$). Age had significant simple effects on tibial Tb.BV/TV in the lateral ($F = 5.985$, $p = 0.011$) and central ($F = 5.008$, $p = 0.020$) joint compartments (Figure 11B). Within the lateral compartment, the mean tibial Tb.BV/TV was highest in the 12-month age group, followed by the 6 and 24-month groups. In the central compartment, the 6-month group had the highest mean tibial Tb.BV/TV followed by the 12 and 24-month groups. Joint compartment had statistically significant simple effects in the 6 ($F = 108.8$, $p < 0.001$), 12 ($F = 160.0$, $p < 0.001$) and 24-month ($F = 95.56$, $p < 0.001$) age groups. In all three age groups, the medial compartment had a greater mean tibial Tb.BV/TV than the lateral compartment.

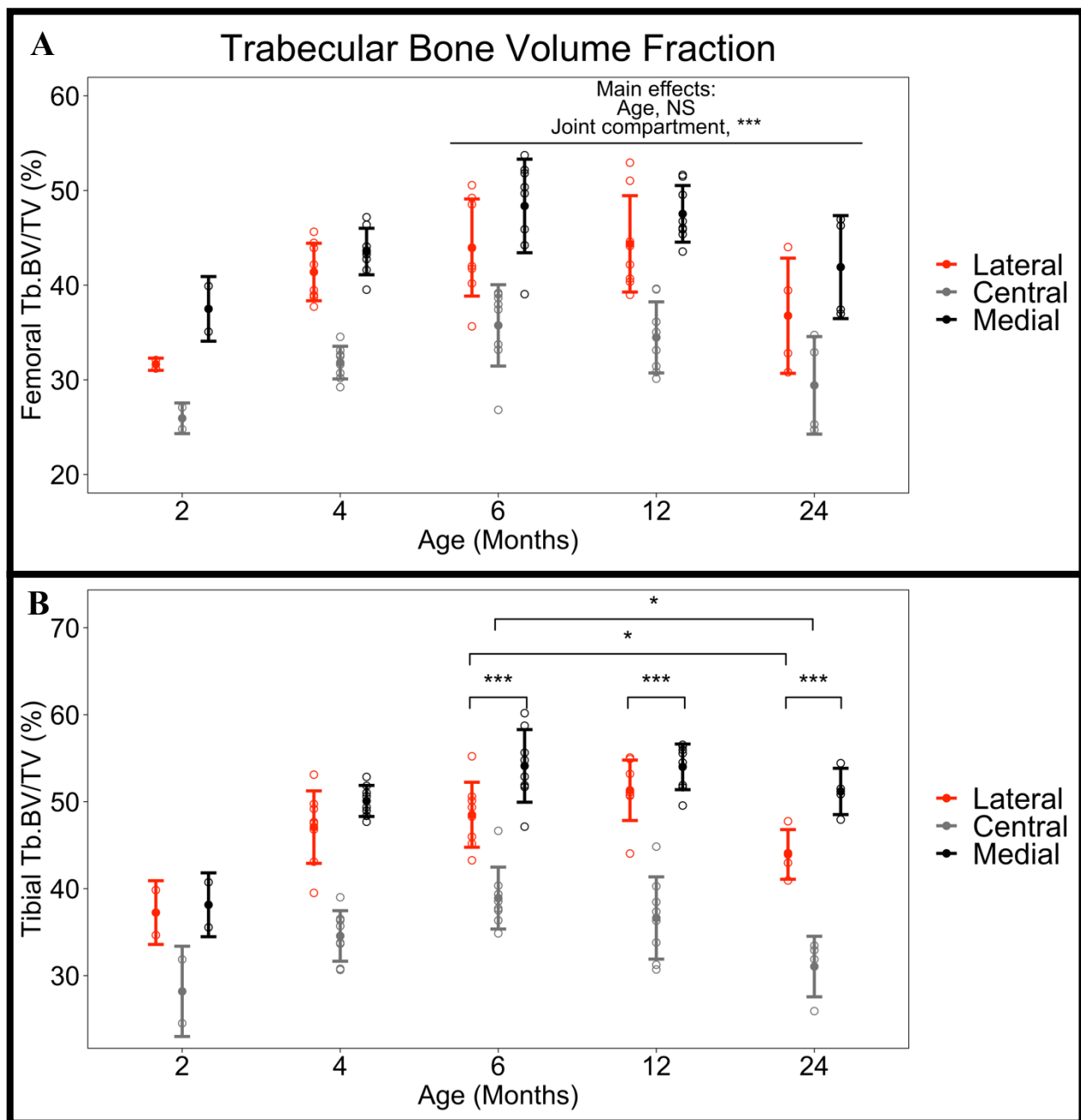


Figure 11. Trabecular bone volume fraction (%) in the lateral, central and medial compartments of the (A) femur and (B) tibia plotted across DH guinea pig age groups. Data points represent individual animals. Mean \pm SD Tb.BV/TV for age groups are indicated by the full circles and error bars, respectively. Main effect results from the two-way ANOVA test are represented in (A), where NS and *** mean $p > 0.05$ and $p \leq 0.001$, respectively. Simple effects result is represented in (B), where * and *** mean $p < 0.05$ and $p \leq 0.001$, respectively.

Regarding femoral Tb.Th, the interaction between age and joint compartment was significant ($F = 4.287$, $p = 0.006$). Age did not have a statistically significant simple effect on femoral Tb.Th in any of the joint compartments (Figure 12A). In contrast, joint compartment had statistically significant simple effects in the 6 ($F = 73.53$, $p < 0.001$), 12 ($F = 55.07$, $p < 0.001$) and 24-month ($F = 6.411$, $p = 0.001$) age groups. In all three age groups, the medial compartment had a greater mean femoral Tb.Th than the lateral compartment.

The tibial Tb.Th results showed a significant interaction between age and joint compartment ($F = 4.683$, $p = 0.004$). Age had a significant simple effect on tibial Tb.Th only in the medial compartment ($F = 9.760$, $p = 0.002$) (Figure 12B). Within this compartment, the mean tibial Tb.Th was highest in the oldest, 24-month age group, followed by the younger 6-month group. Joint compartment had statistically significant simple effects in the 6 ($F = 13.37$, $p < 0.001$), 12 ($F = 11.97$, $p = 0.001$) and 24-month ($F = 16.92$, $p < 0.001$) age groups. In the 6 and 24-month age groups, the medial compartment had a greater mean tibial Tb.Th than the lateral compartment. However, in the 12-month group, the mean tibial Tb.Th of the lateral compartment was greater than that of the medial.

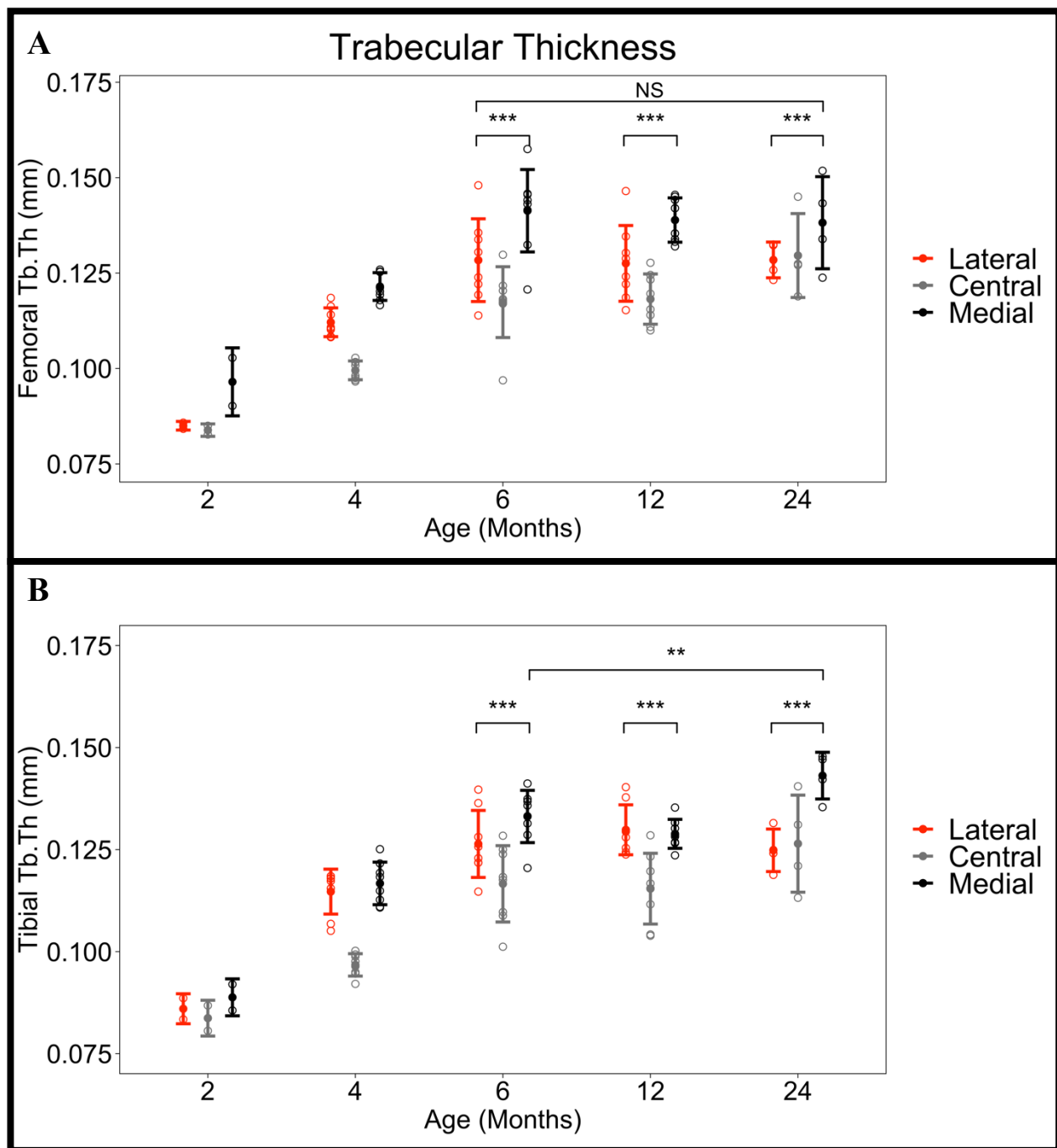


Figure 12. Trabecular thickness (mm) in the lateral, central and medial compartments of the (A) femur and (B) tibia plotted across DH guinea pig age groups. Data points represent individual animals. Mean \pm SD Tb.Th for age groups are indicated by the full circles and error bars, respectively. Simple effects results from the two-way ANOVA tests are represented on plots, where NS, **, and *** mean $p > 0.05$, $p \leq 0.01$, and $p \leq 0.001$, respectively.

The femoral Tb.N results revealed no significant interaction between age and joint compartment ($F = 0.959$, $p = 0.443$). Age ($F = 9.361$, $p = 0.002$) and joint compartment ($F = 199.7$, $p < 0.001$) had statistically significant main effects on femoral Tb.N (Figure 13A). The estimated marginal mean Tb.N was highest in 6-month age group ($3.080 \pm 0.140 \text{ mm}^{-1}$) and lowest in the 24-month group ($2.098 \pm 0.197 \text{ mm}^{-1}$). The medial compartment had a higher estimated marginal mean Tb.N ($3.228 \pm 0.095 \text{ mm}^{-1}$) than the lateral compartment ($3.025 \pm 0.105 \text{ mm}^{-1}$).

The tibial Tb.N results also revealed no significant interaction between age and joint compartment ($F = 1.797$, $p = 0.152$). Age ($F = 7.568$, $p = 0.004$) and joint compartment ($F = 144.7$, $p < 0.001$) had significant main effects on tibial Tb.N (Figure 13B). The 6-month age group had the highest estimated marginal mean tibial Tb.N ($4.064 \pm 0.171 \text{ mm}^{-1}$) while the 24-month group had the lowest ($2.939 \pm 0.242 \text{ mm}^{-1}$). Also, the medial compartment had a higher estimated marginal mean tibial Tb.N ($4.055 \pm 0.120 \text{ mm}^{-1}$) than the lateral compartment ($3.859 \pm 0.132 \text{ mm}^{-1}$).

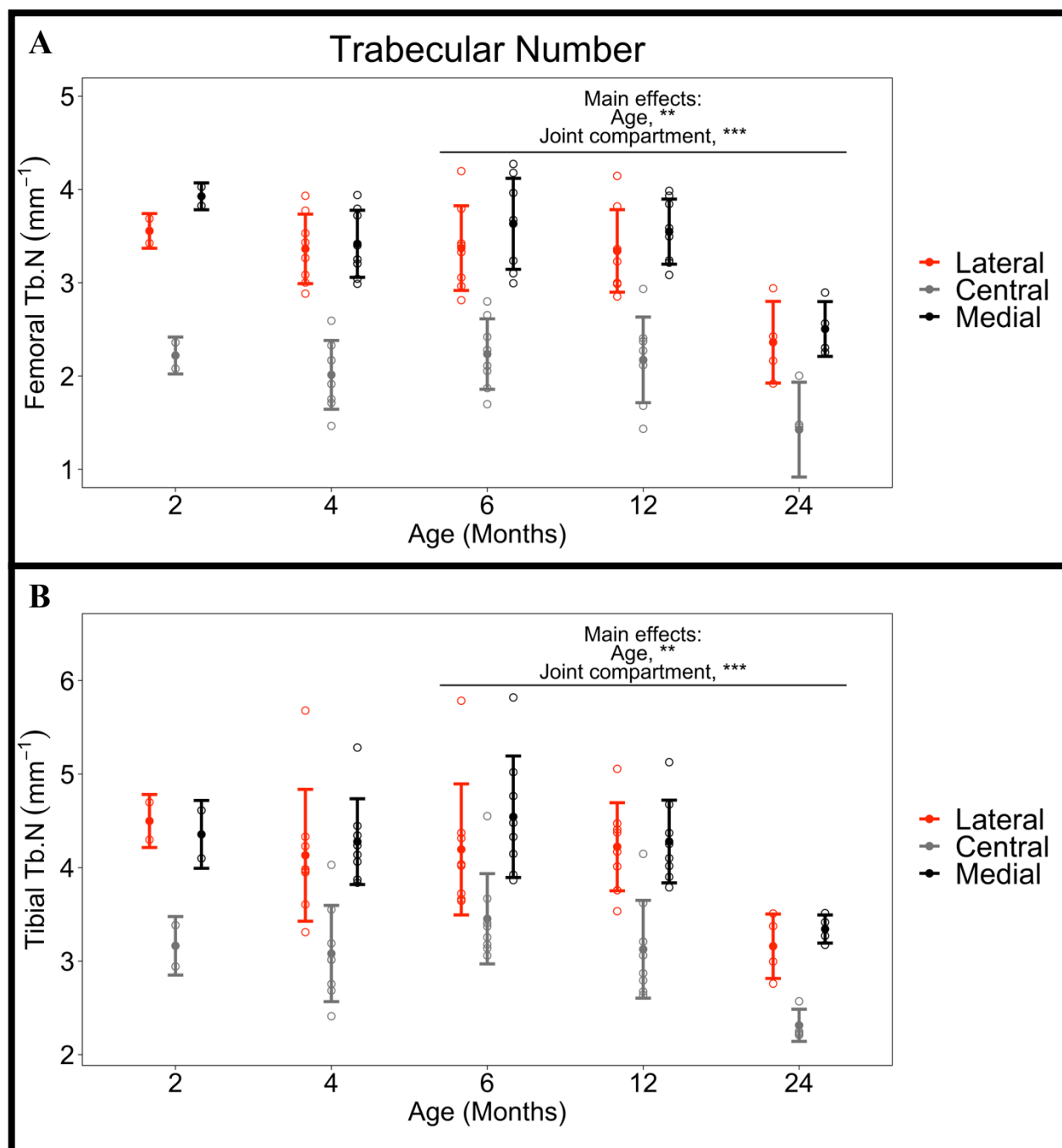


Figure 13. Trabecular number (mm^{-1}) in the lateral, central and medial compartments of the (A) femur and (B) tibia plotted across DH guinea pig age groups. Data points represent individual animals. Mean \pm SD Tb.N for age groups are indicated by the full circles and error bars, respectively. Main effects from the two-way ANOVA test are represented on plots, where ** and *** mean $p \leq 0.01$ and $p \leq 0.001$, respectively.

The femoral Tb.Sp results showed no significant interaction between age and joint compartment ($F = 2.418$, $p = 0.068$). Age ($F = 5.551$, $p = 0.014$) and joint compartment ($F = 58.64$, $p < 0.001$) had significant main effects on femoral Tb.Sp (Figure 14A). Regarding age, the 24-month age group had the highest estimated marginal mean femoral Tb.Sp (0.577 ± 0.051 mm), followed by the 12 (0.388 ± 0.036 mm) and 6-month (0.389 ± 0.036 mm) groups. The lateral joint compartment (0.348 ± 0.013 mm) had a higher estimated marginal mean femoral Tb.Sp than the medial (0.325 ± 0.010 mm).

With tibial Tb.Sp, the interaction between age and joint compartment was significant ($F = 4.160$, $p = 0.008$). Age had significant simple effects on tibial Tb.Sp in the medial ($F = 4.354$, $p = 0.030$), lateral ($F = 4.051$, $p = 0.036$), and central ($F = 7.613$, $p = 0.004$) joint compartments (Figure 14B). Within all three compartments, the 24-month age group had the highest mean tibial Tb.Sp. The 6-month age group had the lowest mean tibial Tb.Sp only in the medial and central compartments. Joint compartment had statistically significant simple effects on tibial Tb.Sp in the 6 ($F = 38.08$, $p < 0.001$), 12 ($F = 63.97$, $p < 0.001$) and 24-month ($F = 52.69$, $p < 0.001$) age groups. In all three age groups, the lateral compartment had a greater mean tibial Tb.Sp than the medial compartment.

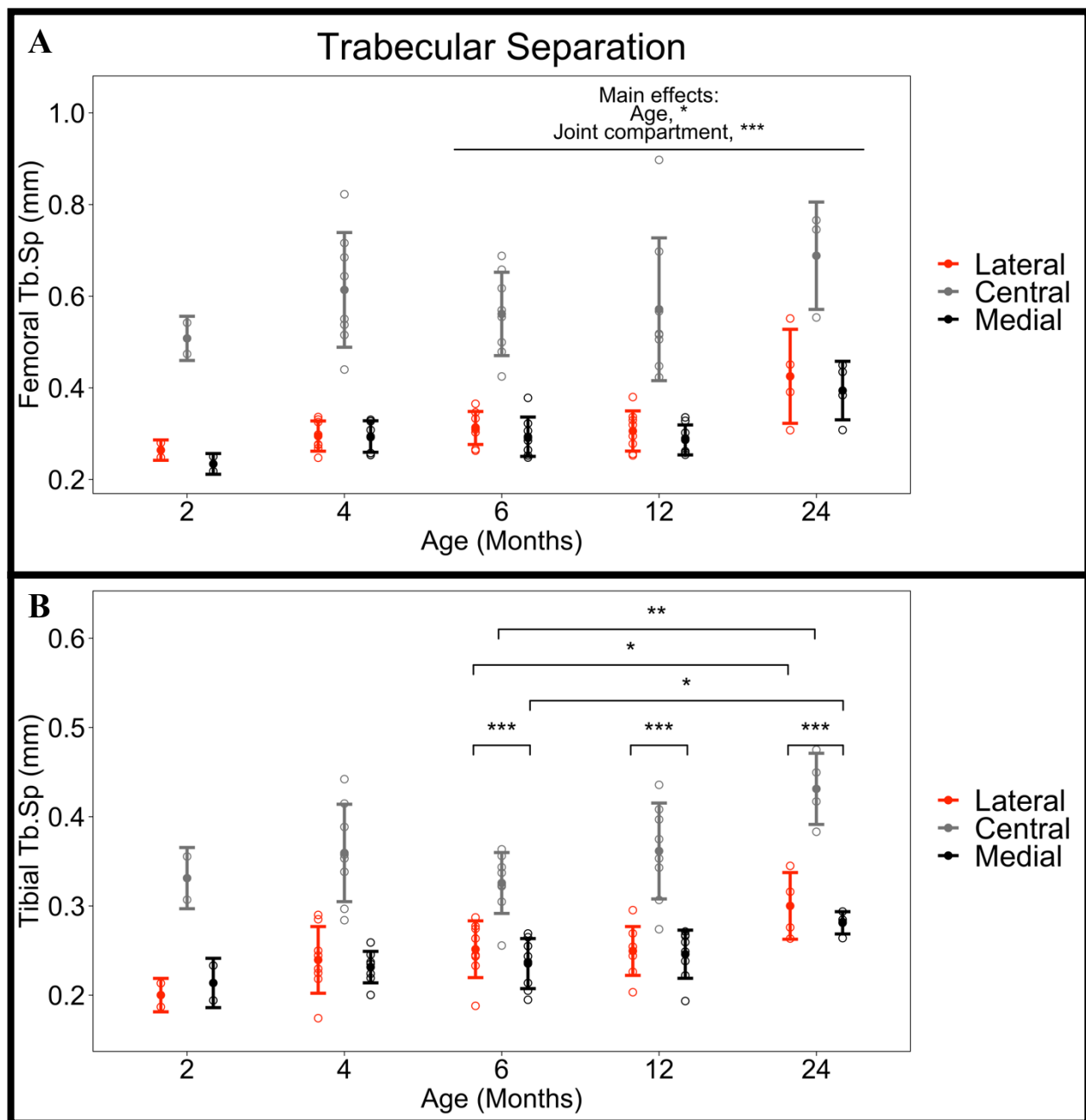


Figure 14. Trabecular separation (mm) in the lateral, central and medial compartments of the (A) femur and (B) tibia plotted across DH guinea pig age groups. Data points represent individual animals. Mean \pm SD Tb.Sp for age groups are indicated by the full circles and error bars, respectively. Main effect results from the two-way ANOVA test are represented in (A), where * and *** mean $p < 0.05$ and $p \leq 0.001$, respectively. Simple effect results are represented in (B), where *, ** and *** mean $p < 0.05$, $p \leq 0.01$ and $p \leq 0.001$, respectively.

3.3.4 Histological Assessments

Hematoxylin-eosin stained sections confirmed the presence of bone anomalies in the DH guinea pigs. When present, cysts were most commonly found in the central compartment of the femur and tibia of the 6, 12, and 24-month age groups. However, there was an exception in a 2-month-old with a cyst in the ACL (Figure 15).

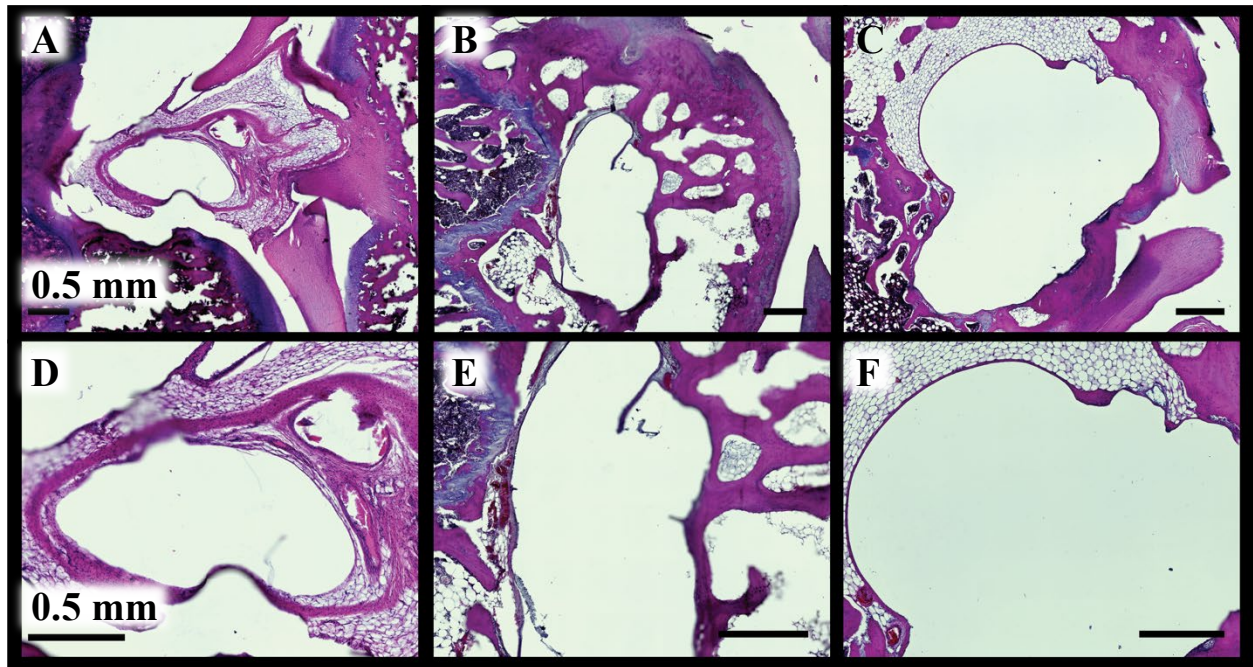


Figure 15. Image of cysts seen on H&E-stained sections from three DH guinea pig age groups. (A&D) ACL cyst in a 2-month-old. (B&E) Femoral cyst in a 12-month-old. (C&F) Femoral cyst and cystic rim in a 24-month-old. Photomicrographs were scanned at 20X magnification.

In addition to cysts, defects, including osteophytes and fibrosis in trabecular bone were observed in 6, 12, and 24-month age groups (Figure 16). Some of the bony defects were also visible on μ CT images (Figure 17). There was no evidence of adipocyte necrosis.

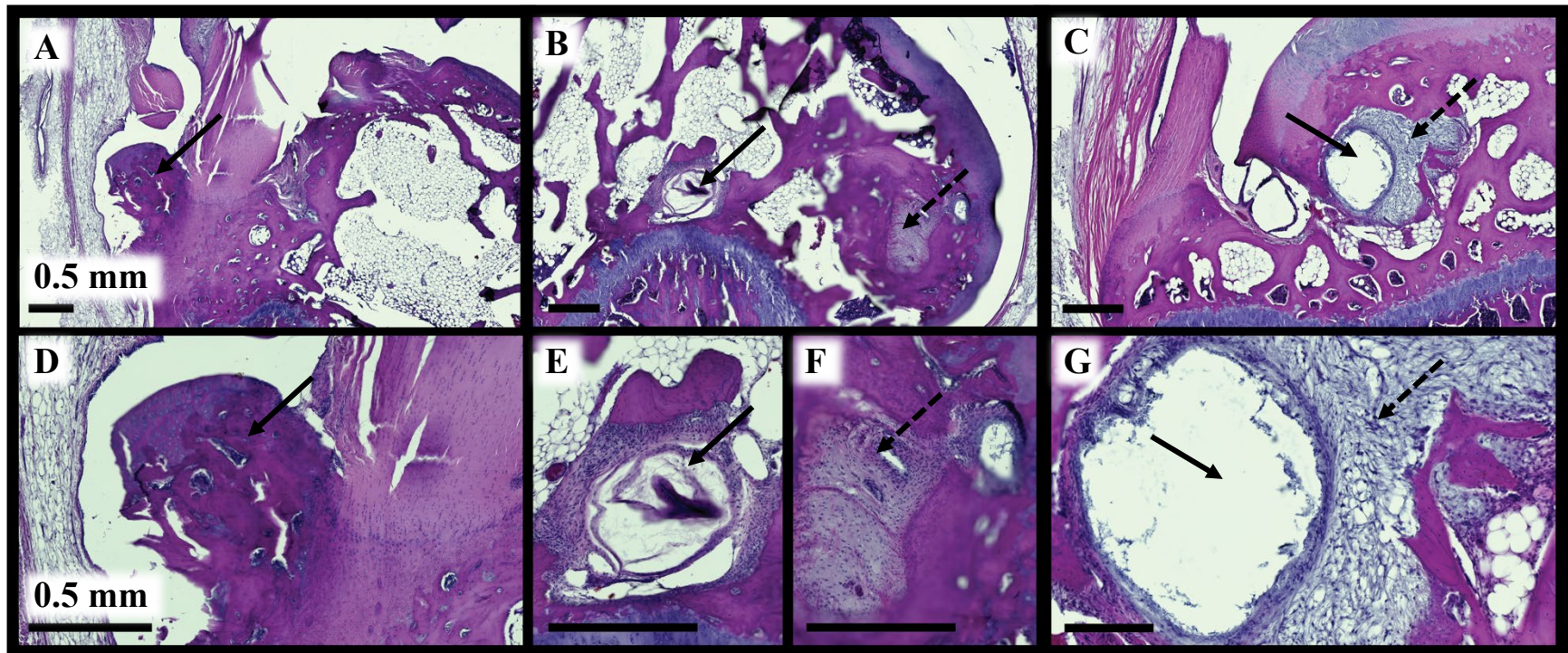


Figure 16. Anomalies (indicated by arrows) were seen on H&E-stained sections of the subchondral bone of the DH guinea pigs. (A&D) A femoral osteophyte (highlighted) near the site of cruciate ligament insertion in a 6-month-old. (B, E, & F) An abnormal soft connective tissue (solid arrow) and an anomaly (dashed arrow) similar to a fibrous clot in a 6-month-old femur. (C&G) A tibial cyst (solid arrow) adjacent to fibrotic tissue (dashed arrow) detected in a 12-month-old. Photomicrographs were scanned at 20X magnification.

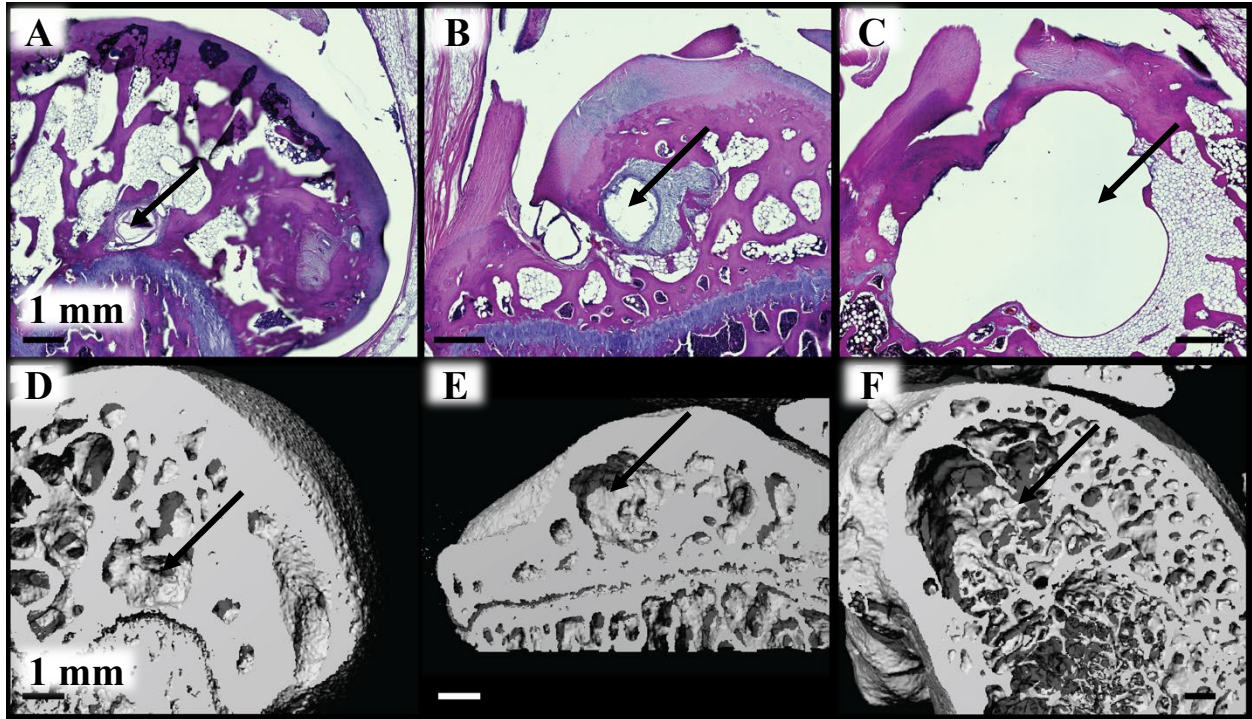


Figure 17. Anomalies (indicated by black arrows) on H&E-stained sections that were bone-related, as seen on μ CT images. (A&D) 6-month-old, (B&E) 12-month-old, (C&F) 24-month-old. Photomicrographs were scanned at 20X magnification. μ CT images were upscaled by a factor of 2.5.

Toluidine blue-stained sections revealed some degeneration in the cartilage overlying bone defects. Cartilage fibrillation, fragmentation, and loss, as well as a reduction in matrix staining and hypocellularity, were seen in the 6, 12, and 24-month age groups (Figure 18).

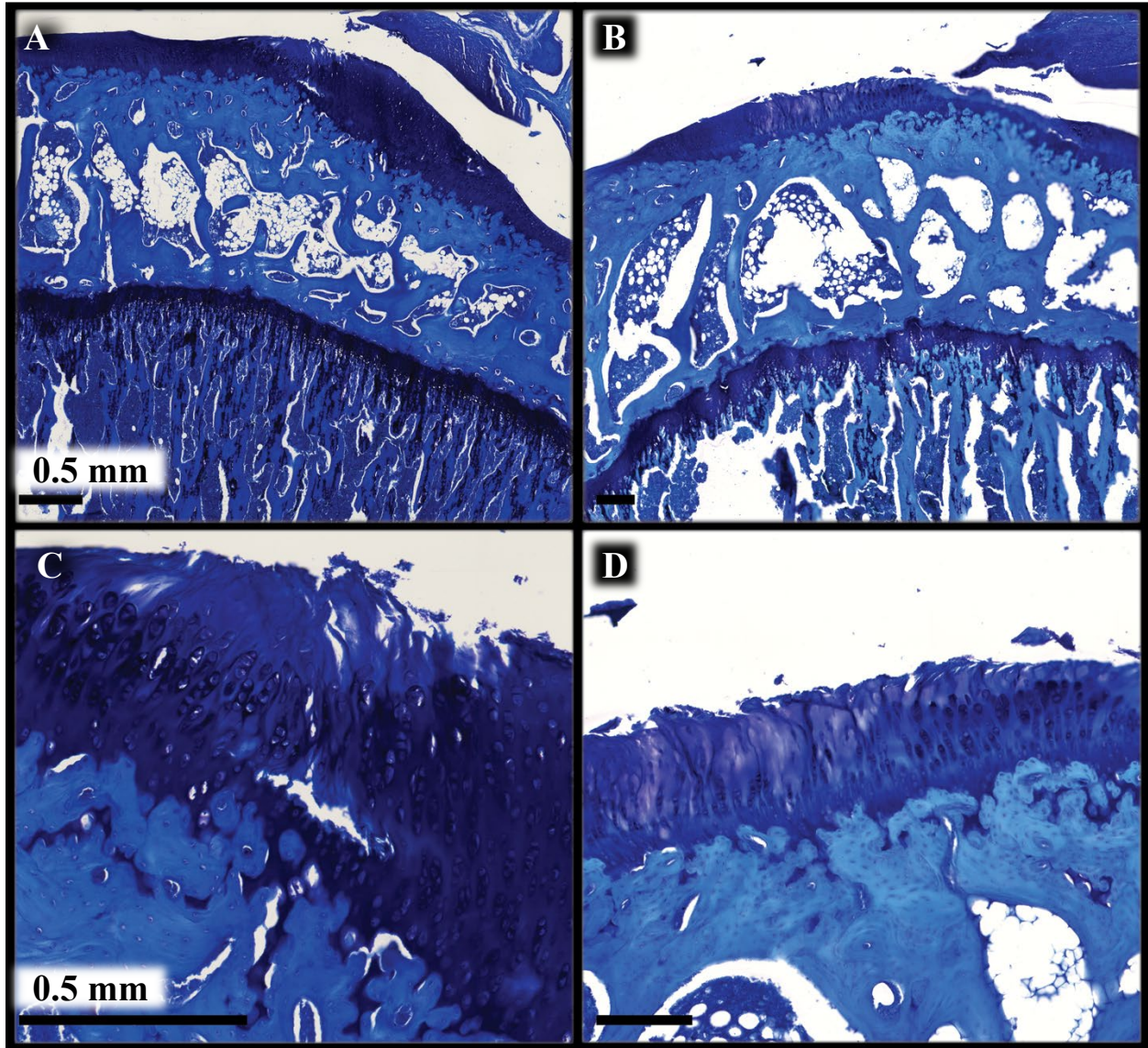


Figure 18. Toluidine-blue stained sections of the articular cartilage overlying a (A&C) 6-month-old tibia and (B&D) 12-month-old tibia. (C) The zoomed in region of the 6-month-old tibial articular cartilage shows fibrillation and fragment loss in the superficial and transitional zone and a moderate reduction in matrix staining. (D) The zoomed in region of the 12-month-old tibial articular cartilage shows fibrillation and loss of matrix stain to the deep zone. Photomicrographs were scanned at 10X magnification.

3.4 Discussion

This study documented the natural history of knee OA-related joint degeneration in the DH guinea pig using complementary information from MRI, μ CT, and histology. Age-related joint degeneration was first evident in the 6-month age group with the presence of cartilage degradation and hypocellularity as well as subchondral cysts, a hallmark of OA (39). Cysts as defined by hyperintense regions on fluid-sensitive MRI and cavities in the trabecular bone on μ CT images and histology sections were more apparent in the 12-month age group and appeared to be larger in the 24-month age group. Other bony evidence of OA, such as sclerosis and osteophytes, were visibly larger in the 24-month group compared to the 12 and 6-month groups. The 24-month age group also demonstrated the most severe joint degeneration, as evidenced by a relatively high RAKSS score and differences in bone microarchitecture, compared to the 12 and 6-month groups. This group had the highest Sbp.Th in the medial femoral compartment, which is indicative of sclerosis. The highest Sbp.Po, Tb.Th in the medial tibia, and femoral Tb.Sp, as well as the lowest femoral and tibial Tb.N and Tb.BMD and Tb.BV/TV in the lateral tibia were also observed in this age group. These findings are consistent with previous studies that reported the alterations in bone microarchitecture during OA progression (16,80,103–107).

Cysts observed in the 6, 12 and 24-month age groups were predominantly located in the central joint compartment near the cruciate ligament insertion site. Cysts formed in this compartment are not classified as weight-bearing cysts, and there is no articular cartilage directly overlying the bone in this area. Thereby, these “insertional” cysts do not fit either synovial fluid or bone contusion theories for cyst formation, as explained in a previous study done on human knee OA (9). However, the ACL insertion site is exposed to very high mechanical stresses, which may cause a bone contusion. Son et al. (2018) highlighted that these insertional cysts are different from those

formed in the weight-bearing compartments of the knee, but they are still associated with OA because they are often related to cartilage degradation in humans (44). Also, cyst location has been associated with increased disease severity in that region, and our histology results showed fibrotic tissue in the region of an insertional cyst, as well as cartilage degradation in bone with cysts (108). Our bone microarchitecture results are also consistent with the Son et al. study because we observed a lower Tb.BMD and Tb.BV/TV, as well as a higher Tb.Sp in the central knee of the oldest, 24-month age group that had the largest cysts. While these insertional cysts appear to be pathological, further investigation is still required to understand why they form and whether they play a role in disease progression and/or pain.

Unlike cysts, we did not observe evidence of BMLs in the MRI scans we obtained. BMLs were defined as diffuse hyperintense regions on fluid-sensitive MRI, and none of the hyperintense regions that we observed matched this definition. One study that only used a histological approach to examine the DH guinea pig model reported fibrotic and necrotic regions on histological sections that they described as BMLs (88). BMLs have been associated with fibrosis and adipocyte necrosis in histological assessments of human arthroplasty samples (6). In our 12-month age group, fibrotic tissue was observed in the same region as an insertional cyst. Therefore, it is possible that BMLs develop in our animal model. However, histological assessments of the weight-bearing regions of the knee, where BMLs typically occur, showing adipocyte necrosis and fibrosis would be required to make a conclusive assessment. With MRI, BMLs were difficult to discern in our samples due to poor STIR MR resolution (1.25 mm slice thickness at 1.0T), and our high-resolution T2 images had inconsistencies with suppressing the little fat in the mostly hematopoietic bone marrow of the younger guinea pig knees. While there was no histological evidence of adipocyte necrosis, which

is commonly reported in BMLs (7), the presence of fibrosis near a cyst lends support to the hypothesis that cysts and BMLs may play similar roles in OA pathogenesis. Further investigation is required to determine if these fibrotic regions can be detected on MRI in this model.

Additionally, we observed some differences in the weight-bearing (medial and lateral) compartments within individual age groups in our bone microarchitecture results. The varus alignment of the DH guinea pig knee means that the medial compartment is under more mechanical stress than the lateral compartment (64). This is also the case in humans with a similar alignment of the knee. While OA may vary across the joint, more commonly, it is often more severe in the medial than in the lateral compartment (109). Hence, it is expected that the disease seen in this model is more evident in the medial compartment (3,71). Our results found some evidence of increased joint degeneration on the medial compartment of the DH guinea pig knee joints. Femoral and tibial Sbp.Th in the 6, 12, and 24-month age groups, as well as femoral Sbp.Po in the 12 and 24-month groups was greater in the medial compartment compared to the lateral compartment. These findings are consistent with studies that have reported a thickened and more porous subchondral bone plate from patients with OA (16,107).

However, this study is not without limitations. First, the DH guinea pig does not have a control because all guinea pigs eventually develop joint degeneration in their lifetime. For that reason, we decided to focus on comparisons between older, skeletally mature animals and young animals. Second, the same MR imaging was not done on all the guinea pigs. While the T2 MRI on a 9.4T (0.5 mm slice thickness) had a much better signal-to-noise ratio (SNR), fat suppression was inconsistent in mostly hematopoietic bone marrow, and we found that STIR was better suited for imaging this model. However, we didn't use STIR at 9.4T because of the lengthening and convergence of T1 relaxation times at high magnetic fields, which makes it difficult to achieve good T1

contrast. Therefore, we used a 1.0T MRI for STIR imaging to adequately capture hyperintensities in the predominantly hematopoietic bone marrow of the DH guinea pig samples, but the low-field scanner and 1.25 mm slice thickness used led to images with lower spatial resolution. STIR imaging could alternatively be performed on 3.0T MRI, improving the SNR and allowing the flexibility to pick a slice thickness with good spatial resolution. Third, our MR imaging, which was performed in the coronal plane, was conducted before finalizing a histology protocol that involved sagittal sectioning, making it challenging to make side by side visual assessments. Sagittal sectioning was chosen over coronal to facilitate the decalcification process of our samples, but the same MRI, μ CT and histology orientations would have been advantageous for multi-modal comparison. Fourth, our histological analyses were focused on the central compartment to describe the tissue characteristics where cysts were predominantly visualized on MRI and CT. Future work would additionally examine the histological sections within weight-bearing regions. Lastly, our bone microarchitecture analysis involved significant manual corrections during the segmentation of cortical and trabecular bone. To minimize the potential sources of error, a single experienced user made all of the corrections; nonetheless, this step may have introduced some error in our bone microarchitecture results.

For future work, *in vivo* MR and μ CT imaging will be conducted on DH guinea pigs from ages 4 to 24 months to monitor the development of insertional cysts and their relationship to longitudinal changes in bone microarchitecture and soft tissue. Pain as a function of cyst volume and overall joint degeneration will also be assessed in this model via the recording of electrophysiological activity of joint nociceptive nerves (96). This work will give insight into the etiology of insertional cysts and whether they are related to pain.

3.5 Conclusions

This study demonstrates that joint degeneration occurs in the DH guinea pig spontaneous knee OA model with age and as a result of abnormal stresses that may arise at the insertional site of a ligament and in the medial compartment of a varus knee. The spontaneous DH guinea pig knee OA model allowed us to characterize the development of insertional cysts that may originate from abnormal stresses on the subchondral bone at the site of ACL insertion. These subchondral cysts appeared relatively early in the young adult 6-month-old guinea pigs. They also increased in size and number in the much older 24-month-old guinea pigs, suggesting age-related joint degeneration in this model. While we found no evidence of BMLs on our MR images, our histology results show fibrosis in the region of an insertional cyst. Therefore, it may be valuable to explore the etiology of insertional cysts in this model as they might be similar to BMLs. The DH guinea pig allowed us to explore an idiopathic subtype of OA and is a good model to possibly study OA prospectively.

Chapter 4: General Discussion

4.1 Addressing Aims

The purpose of this thesis project was to describe the natural history of knee OA in the DH guinea pig by documenting knee joint degeneration, investigating the presence and timing of any BMLs and cysts, and characterizing the development of the insertional cysts seen in this model. The first aim was to document the knee joint degeneration in the DH guinea pig with complementary information from MRI, μ CT, and histology. I documented knee joint degeneration in this model and found evidence of age-related cartilage degradation, sclerosis, osteophytes, and cysts. Other interesting findings include age-related meniscal ossification and weight gain. Meniscal ossification appears to be a common finding in the DH guinea pig and has been proposed to alter their knee joint biomechanics, possibly contributing to joint degeneration (72). The older guinea pigs weighed more than the younger guinea pigs; therefore, obesity might have played a role in the observed degeneration seen in the older guinea pigs. Obesity, which is a risk factor of idiopathic OA in humans, has also been observed to be correlated with the severity of joint degeneration in a study that compared DH guinea pigs fed with standard chow to those that were diet-restricted (71).

The second aim was focused on investigating the presence and timing of BMLs and cysts in the subchondral bone of the DH guinea pig relative to other pathological features associated with the development of knee OA. After a cross-sectional assessment of DH guinea pig knee joints at ages 2, 4, 6, 12 and 24 months, I did not find evidence of BML presence. BMLs were assessed on MRI by searching for diffuse hyperintense regions, which were absent. These lesions could not be properly assessed on histology because my results did not include histological sections of the weight-bearing regions of the joint. On the other hand, I found bone cysts in the central, non-

weight-bearing compartment of the 6, 12 and 24-month-old guinea pigs near the ACL insertion site. These cysts were present along with cartilage degradation and osteophytes, which are OA-related features. The size and number of these cysts also appeared to increase with age, suggestive of age-related increases in degeneration.

Lastly, the third aim was to characterize the development of insertional cysts and whether they are associated with pathological features of knee OA. This aim was developed to better understand the type of cysts seen in my DH guinea pig sample because they did not develop in the weight-bearing region of the bone. These insertional cysts are so-called because they are located near the ACL insertion site in the bone (44). They also appeared to be pathological as they were present alongside OA features such as osteophytes and cartilage degradation. However, further investigation in the form of a longitudinal study is required to better understand their progression.

4.2 Validity of Measurements

The measurements used in my thesis are valid and inspired by peer-reviewed publications (10,11,98). In the bone microarchitecture analysis, the 5 μm difference in voxel size between the 24-month and other age groups accounted for very little measurement error because of the relatively high thickness of the DH guinea pig bone, even at the level of the trabeculae.

Regarding RAKSS, this semi-quantitative scoring system was modified to only include only bony features from μCT images, including osteophytes, subchondral sclerosis, bone cysts and loose bodies. While this score is valid for analyzing bony degeneration in this model, it cannot be generalized to whole joint OA because the disease involves other parts of the joint such as the articular cartilage and synovium that were not assessed.

4.3 Study Limitations

A major limitation of my project was the inability to confirm the presence or absence of BMLs on my MR scans. The low-field 1.0T scanner and 1.25 mm slice thickness led to images with lower spatial resolution, and the coronal orientation of the MR images made it challenging for multi-modal registration with the 15 μm thick sagittal histological sections. Also, one of the gradients on the 1.0T MRI was faulty, which caused a motion-like artifact on the scans, and this was not fixed for the duration of my study. BMLs are defined as diffuse regions of hyperintense signal on fluid-sensitive MRI, meaning that they are made up of fluid. They also appear to be associated with adipocyte necrosis and bone marrow fibrosis, as confirmed with histology. The only report of BMLs in the DH guinea pig is from a study that only used a histological approach (88). However, histology alone is insufficient to define these lesions because fluid is not typically seen in histological sections. I expected to find BMLs in the DH guinea pig because cysts, which have been associated with them, develop in this model. However, the cysts found within my sample were mostly insertional cysts, which are different from weight-bearing cysts that have been associated with BMLs in human knee OA studies (8,9). In short, I have no evidence that BMLs are associated with the joint degeneration observed in this model, and further research is required to determine whether or not they exist in this model.

4.4 Future Directions

In light of the above limitation, which is also discussed in Chapter 3, some things can be improved upon in the future. First, acquiring the same STIR MRI for all samples is necessary to compare hyperintensities across age groups. Unfortunately, we obtained the 24-month-old samples

opportunistically through Veterinary Medicine before any pilot testing or histology had been performed; hence we performed T2 FLASH images as would typically be performed to detect BMLs in adults with primarily yellow marrow. However, our first histological sections revealed hematopoietic marrow even in these aged animals. Also, with the gradient issues on the 1.0T MRI resolved, the quality of STIR images would improve, and more images, including some 4-month-old knees that were not scanned, can be obtained. These images would also be in the sagittal orientation, matching the histology sections. Additionally, I would obtain histological sections from the weight-bearing regions of the knee joints to include semi-quantitative modified Mankin scores to assess age-related and joint compartmental differences in cartilage structure. This project focused on histological sections in the central compartment, where insertional cysts were present to see whether or not they were associated with other anomalies. Even so, a histological assessment of the weight-bearing compartments of the knee could highlight anomalies that may develop in these regions as a result of degeneration.

In the future, I would like this project adapted to incorporate a longitudinal study, with *in vivo* MR and μ CT imaging. With a longitudinal study, individual age-related joint degeneration can also be documented over time, thereby modelling the natural history of spontaneous knee OA in an *in vivo* environment. However, this will only be possible with optimized *in vivo* μ CT and MR imaging protocols that involve a fully functioning MRI, capable of STIR imaging.

4.5 Concluding Remarks

The DH guinea pig is a good model for a specific subtype of idiopathic knee OA. OA is known as a heterogeneous disease, where hallmark features such as cartilage degradation, sclero-

sis, osteophytes, and cysts have been reported (43). Other features including BMLs are also commonly seen with this disease, although they do not occur in all cases of knee OA (6). Our DH guinea pig sample showed evidence of cartilage degradation, osteophyte formation, sclerosis, and cysts. The degenerative features also appeared to be age-related, an encouraging finding for this model as age is a major risk factor for idiopathic OA (33). Despite challenges assessing BMLs, the changes in 3D bone microarchitecture and increase in total RAKSS score also demonstrate this age-related joint degeneration. Based on our findings, we did not document the natural history of BMLs in our animal model. However, we were able to document insertional cysts, and this project that combines MRI, μ CT and bone microarchitecture analysis, semi-quantitative RAKSS, and histological assessments lends support to others that have evaluated joint degeneration in the DH guinea pig spontaneous knee OA model using a single approach. Our results can also allow for comparisons with clinical studies using a similar methodology.

Osteoarthritis is still very prevalent, and there is a need for effective disease-modifying treatments. A better understanding of the disease etiology is the solution to this problem. The challenge lies with the slow degenerative process of idiopathic OA in humans, making it difficult to document the natural history of the disease. Therefore, we used the DH guinea pig as a model for idiopathic knee OA in this project because of their ability to spontaneously develop a knee OA phenotype similar to the disease seen in humans. Animal models that OA is induced by joint injury model post-traumatic OA, which likely occurs via a different mechanism than that of idiopathic OA, are not suited to model idiopathic OA. In summary, the DH guinea pig, where joint damage occurs with age, is more appropriate for modelling idiopathic OA and serves as a good candidate to document its natural history.

References

1. Allen KD, Golightly YM. State of the evidence. *Curr Opin Rheumatol*. 2015;27(3):276–283.
2. Felson DT, Chaisson CE, Hill CL, et al. The association of bone marrow lesions with pain in knee osteoarthritis. *Ann Intern Med*. 2001;134(7):541.
3. Tessier J., Bowyer J, Brownrigg N., et al. Characterisation of the guinea pig model of osteoarthritis by in vivo three-dimensional magnetic resonance imaging. *Osteoarthr Cartil*. 2003;11(12):845–853.
4. Thomas AC, Hubbard-Turner T, Wikstrom EA, Palmieri-Smith RM. Epidemiology of posttraumatic osteoarthritis. *J Athl Train*. 2017;52(6):491–496.
5. Hannan MT, Felson DT, Pincus T. Analysis of the discordance between radiographic changes and knee pain in osteoarthritis of the knee. *J Rheumatol*. 2000;27(6):1513–1517.
6. Zanetti M, Bruder E, Romero J, Hodler J. Bone marrow edema pattern in osteoarthritic knees: Correlation between MR imaging and histologic findings. *Radiology*. 2000;215(3):835–840.
7. Kazakia GJ, Kuo D, Schooler J, et al. Bone and cartilage demonstrate changes localized to bone marrow edema-like lesions within osteoarthritic knees. *Osteoarthr Cartil*. 2013;21(1):94–101.
8. Crema MD, Roemer FW, Zhu Y, et al. Subchondral cystlike lesions develop longitudinally in areas of bone marrow edema-like lesions in patients with or at risk for knee osteoarthritis: Detection with MR imaging—the MOST study. *Radiology*.

- 2010;256(3):855–862.
9. Pouders C, De Maeseneer M, Van Roy P, Gielen J, Goossens A, Shahabpour M. Prevalence and MRI-anatomic correlation of bone cysts in osteoarthritic knees. *Am J Roentgenol*. 2008;190(1):17–21.
 10. Buie HR, Campbell GM, Klinck RJ, MacNeil JA, Boyd SK. Automatic segmentation of cortical and trabecular compartments based on a dual threshold technique for in vivo micro-CT bone analysis. *Bone*. 2007;41(4):505–515.
 11. Kroker A, Zhu Y, Manske SL, Barber R, Mohtadi N, Boyd SK. Quantitative in vivo assessment of bone microarchitecture in the human knee using HR-pQCT. *Bone*. 2017;97:43–48.
 12. Putz R, Mühlhofer H, Ercan Y. [Ligaments of the knee]. *Orthopade*. 2007;36(7):612–619.
 13. Sophia Fox AJ, Bedi A, Rodeo SA. The basic science of articular cartilage: Structure, composition, and function. *Sports Health*. 2009;1(6):461–468.
 14. Bhosale AM, Richardson JB. Articular cartilage: Structure, injuries and review of management. *Br Med Bull*. 2008;87(1):77–95.
 15. Clarke B. Normal bone anatomy and physiology. *Clin J Am Soc Nephrol*. 2008;3 Suppl 3:131–139.
 16. Burr DB, Gallant MA. Bone remodelling in osteoarthritis. *Nat Rev Rheumatol*. 2012;8(11):665–673.
 17. Burr DB. Targeted and nontargeted remodeling. *Bone*. 2002;30(1):2–4.
 18. Fox AJS, Wanivenhaus F, Burge AJ, Warren RF, Rodeo SA. The human meniscus: A

- review of anatomy, function, injury, and advances in treatment. *Clin Anat.* 2015;28(2):269–287.
19. Cox C, Hubbard J. *Anatomy, Bony Pelvis and Lower Limb, Knee Lateral Meniscus.* StatPearls Publishing; 2020.
 20. Clarke HD, Kransdorf MJ, Conley CR, Pederson HB, Scott WN. *Anatomy. In: Scott Surg knee.* Philadelphia, PA : Elsevier; Sixth edition.; 2018. p. 2-49.e3.
 21. Harfe DT, Chuinard CR, Espinoza LM, Thomas KA, Solomonow M. Elongation patterns of the collateral ligaments of the human knee. *Clin Biomech.* 1998;13(3):163–175.
 22. Smith NB, Webb A. *X-ray Planar Radiography and Computed Tomography. Introd to Med Imaging Physics, Eng Clin Appl.* Cambridge University Press; 2010. p. 34–88.
 23. Bushberg JT, Seibert JA, Leidholdt EM. *Introduction to Medical Imaging. Essent Phys Med Imaging.* Philadelphia: Wolters Kluwer Health; 2011. p. 3–17.
 24. Smith NB, Webb A. *Magnetic Resonance Imaging (MRI). Introd to Med Imaging Physics, Eng Clin Appl.* Cambridge University Press; 2010. p. 204–281.
 25. Westbrook C, Roth CK, Talbot J. *Basic Principles. MRI Pract.* 4th ed. Wiley-Blackwell; 2011.
 26. Berger A. How does it work?: Magnetic resonance imaging. *BMJ.* 2002;324(7328):35–35.
 27. Bushberg JT, Seibert JA, Leidholdt EM. *Magnetic Resonance Basics: Magnetic Fields, Nuclear Magnetic Characteristics, Tissue Contrast, Image Acquisition. Essent Phys Med Imaging.* Philadelphia: Wolters Kluwer Health; 2011. p. 402–448.
 28. Bombardier C, Hawker G, Mosher D. The impact of arthritis in Canada: Today and over

- the next 30 years. Arthritis Alliance of Canada. 2011;Fall:52.
29. Felson DT, Naimark A, Anderson J, Kazis L, Castelli W, Meenan RF. The prevalence of knee osteoarthritis in the elderly. The Framingham osteoarthritis study. *Arthritis Rheum.* 1987;30(8):914–918.
 30. Andriacchi TP, Mündermann A, Smith RL, Alexander EJ, Dyrby CO, Koo S. A framework for the in vivo pathomechanics of osteoarthritis at the knee. *Ann Biomed Eng.* 2004;32(3):447–457.
 31. Cooper C, Snow S, McAlindon TE, et al. Risk factors for the incidence and progression of radiographic knee osteoarthritis. *Arthritis Rheum.* 2000;43(5):995.
 32. Felson DT, Zhang Y, Hannan MT, et al. Risk factors for incident radiographic knee osteoarthritis in the elderly. *Arthritis Rheum.* 1997;40(4):728–733.
 33. Palazzo C, Nguyen C, Lefevre-Colau MM, Rannou F, Poiraudau S. Risk factors and burden of osteoarthritis. *Ann Phys Rehabil Med.* 2016;59(3):134–138.
 34. Johnson VL, Hunter DJ. The epidemiology of osteoarthritis. *Best Pract Res Clin Rheumatol.* Elsevier Ltd; 2014;28(1):5–15.
 35. Felson DT. Epidemiology of hip and knee osteoarthritis. *Epidemiol Rev.* 1988;10(1):1–28.
 36. Tanamas S, Hanna FS, Cicuttini FM, Wluka AE, Berry P, Urquhart DM. Does knee malalignment increase the risk of development and progression of knee osteoarthritis? A systematic review. *Arthritis Care Res.* 2009;61(4):459–467.
 37. Hunter DJ, Niu J, Felson DT, et al. Knee alignment does not predict incident osteoarthritis: The Framingham osteoarthritis study. *Arthritis Rheum.* 2007;56(4):1212–

1218.

38. Bank RA, Soudry M, Maroudas A, Mizrahi J, Tekoppele JM. The increased swelling and instantaneous deformation of osteoarthritic cartilage is highly correlated with collagen degradation. *Arthritis Rheum.* 2000;43(10):2202–2210.
39. Martel-Pelletier J, Barr AJ, Cicuttini FM, et al. Osteoarthritis. *Nat Rev Dis Prim.* 2016;2(1):16072.
40. Felson DT. The sources of pain in knee osteoarthritis. *Curr Opin Rheumatol.* 2005;17(5):624–628.
41. Shabestari M, Vik J, Reseland JE, Eriksen EF. Bone marrow lesions in hip osteoarthritis are characterized by increased bone turnover and enhanced angiogenesis. *Osteoarthr Cartil.* 2016;24(10):1745–1752.
42. Ondrouch AS. Cyst formation in osteoarthritis. *J Bone Joint Surg Br.* 1963;45-B(4):755–760.
43. Carrino JA, Blum J, Parellada JA, Schweitzer ME, Morrison WB. MRI of bone marrow edema-like signal in the pathogenesis of subchondral cysts. *Osteoarthr Cartil.* 2006;14(10):1081–1085.
44. Son JY, Yoon YC, Jin W, Cha JG. The prevalence and characteristics of a subcortical cystic lesion at the subspinous region of the knee. *Acta radiol.* 2018;59(1):97–104.
45. Altman R, Asch E, Bloch D, et al. Development of criteria for the classification and reporting of osteoarthritis: Classification of osteoarthritis of the knee. *Arthritis Rheum.* 1986;29(8):1039–1049.

46. Johns Hopkins Arthritis Center. ACR Diagnostic Guidelines. 2020.
https://www.hopkinsarthritis.org/physician-corner/education/arthritis-education-diagnostic-guidelines/#class_knee. Accessed April 14, 2020.
47. Hunter DJ, Arden N, Conaghan PG, et al. Definition of osteoarthritis on MRI: Results of a Delphi exercise. *Osteoarthr Cartil*. 2011;19(8):963–969.
48. Guermazi A, Hayashi D, Eckstein F, Hunter DJ, Duryea J, Roemer FW. Imaging of osteoarthritis. *Rheum Dis Clin North Am*. 2013;39(1):67–105.
49. Altman RD, Gold GE. Atlas of individual radiographic features in osteoarthritis, revised. *Osteoarthr Cartil*. 2007;15(SUPPL. A):A1–A56.
50. Keen HI, Conaghan PG. Ultrasonography in osteoarthritis. *Radiol Clin North Am*. 2009;47(4):581–594.
51. Kellgren JH, Lawrence JS. Radiological assessment of osteo-arthritis. *Ann Rheum Dis*. 1957;16(4):494–502.
52. Boegård T, Rudling O, Petersson IF, et al. Postero-anterior radiogram of the knee in weight-bearing and semiflexion: Comparison with MR imaging. *Acta radiol*. 1997;38(6):1063–1070.
53. Hunter DJ, Zhang W, Conaghan PG, et al. Responsiveness and reliability of MRI in knee osteoarthritis: a meta-analysis of published evidence. *Osteoarthr Cartil*. 2011;19(5):589–605.
54. Peterfy C., Guermazi A, Zaim S, et al. Whole-Organ Magnetic Resonance Imaging Score (WORMS) of the knee in osteoarthritis. *Osteoarthr Cartil*. 2004;12(3):177–190.

55. Hunter DJ, Lo GH, Gale D, Grainger AJ, Guermazi A, Conaghan PG. The reliability of a new scoring system for knee osteoarthritis MRI and the validity of bone marrow lesion assessment: BLOKS (Boston-Leeds Osteoarthritis Knee Score). *Ann Rheum Dis*. 2008;67(2):206–211.
56. Hunter DJ, Guermazi A, Lo GH, et al. Evolution of semi-quantitative whole joint assessment of knee OA: MOAKS (MRI Osteoarthritis Knee Score). *Osteoarthr Cartil*. 2011;19(8):990–1002.
57. Wenham CYJ, Grainger AJ, Conaghan PG. The role of imaging modalities in the diagnosis, differential diagnosis and clinical assessment of peripheral joint osteoarthritis. *Osteoarthr Cartil*. 2014;22(10):1692–1702.
58. Cook JL, Kuroki K, Visco D, Pelletier J-P, Schulz L, Lajeunesse FPJG. The OARSI histopathology initiative – recommendations for histological assessments of osteoarthritis in the dog. *Osteoarthr Cartil*. Elsevier Ltd; 2010;18(SUPPL. 3):S66–S79.
59. Aho OM, Finnilä M, Thevenot J, Saarakkala S, Lehenkari P. Subchondral bone histology and grading in osteoarthritis. *PLoS One*. 2017;12(3):1–16.
60. Mankin HJ. Biochemical and metabolic aspects of osteoarthritis. *Orthop Clin North Am*. 1971;2(1):19–31.
61. Pritzker KPH, Gay S, Jimenez SA, et al. Osteoarthritis cartilage histopathology: Grading and staging. *Osteoarthr Cartil*. 2006;14(1):13–29.
62. Bijlsma JWJ, Berenbaum F, Lajeunesse FPJG. Osteoarthritis: An update with relevance for clinical practice. *Lancet*. 2011;377(9783):2115–2126.

63. Wood AM, Brock TM, Heil K, Holmes R, Weusten A. A review on the management of hip and knee osteoarthritis. *Int J Chronic Dis*. 2013;2013:1–10.
64. Gregory MH, Capito N, Kuroki K, Stoker AM, Cook JL, Sherman SL. A review of translational animal models for knee osteoarthritis. *Arthritis*. 2012;2012:1–14.
65. Piscaer TM, Van Osch GJVM, Verhaar JAN, Weinans H. Imaging of experimental osteoarthritis in small animal models. *Biorheology*. 2008;45(3–4):355–364.
66. Kraus VB, Huebner JL, DeGroot J, Bendele A. The OARSI histopathology initiative – recommendations for histological assessments of osteoarthritis in the guinea pig. *Osteoarthr Cartil*. Elsevier Ltd; 2010;18(SUPPL. 3):S35–S52.
67. Kuyinu EL, Narayanan G, Nair LS, Laurencin CT. Animal models of osteoarthritis: classification, update, and measurement of outcomes. *J Orthop Surg Res*. 2016;11(1):19.
68. Bendele AM, Hulman JF. Spontaneous cartilage degeneration in guinea pigs. *Arthritis Rheum*. 1988;31(4):561–565.
69. Huebner JL, Hanes MA, Beekman B, TeKoppele JM, Kraus VB. A comparative analysis of bone and cartilage metabolism in two strains of guinea-pig with varying degrees of naturally occurring osteoarthritis. *Osteoarthr Cartil*. 2002;10(10):758–767.
70. Zamli Z, Robson Brown K, Tarlton JF, et al. Subchondral bone plate thickening precedes chondrocyte apoptosis and cartilage degradation in spontaneous animal models of osteoarthritis. *Biomed Res Int*. 2014;2014:1–10.
71. Bendele AM, Hulman JF. Effects of body weight restriction on the development and progression of spontaneous osteoarthritis in guinea pigs. *Arthritis Rheum*.

- 1991;34(9):1180–1184.
72. Kapadia R., Badger A., Levin J., et al. Meniscal ossification in spontaneous osteoarthritis in the guinea-pig. *Osteoarthr Cartil.* 2000;8(5):374–377.
 73. Quasnicka HL, Anderson-MacKenzie JM, Bailey AJ. Subchondral bone and ligament changes precede cartilage degradation in guinea pig osteoarthritis. *Biorheology.* 2006;43(3,4):389–397.
 74. Quasnicka HL, Anderson-MacKenzie JM, Tarlton JF, Sims TJ, Billingham MEJ, Bailey AJ. Cruciate ligament laxity and femoral intercondylar notch narrowing in early-stage knee osteoarthritis. *Arthritis Rheum.* 2005;52(10):3100–3109.
 75. Silverwood V, Blagojevic-Bucknall M, Jinks C, Jordan JL, Protheroe J, Jordan KP. Current evidence on risk factors for knee osteoarthritis in older adults: A systematic review and meta-analysis. *Osteoarthr Cartil.* 2015;23(4):507–515.
 76. Sharma L, Song J, Dunlop D, et al. Varus and valgus alignment and incident and progressive knee osteoarthritis. *Ann Rheum Dis.* 2010;69(11):1940–1945.
 77. Blalock D, Miller A, Tilley M, Wang J. Joint instability and osteoarthritis. *Clin Med Insights Arthritis Musculoskelet Disord.* 2015;8:15–23.
 78. van der Kraan PM, van den Berg WB. Osteophytes: Relevance and biology. *Osteoarthr Cartil.* 2007;15(3):237–244.
 79. Hannan MT, Anderson JJ, Zhang Y, Levy D, Felson DT. Bone mineral density and knee osteoarthritis in elderly men and women. The Framingham study. *Arthritis Rheum.* 1993;36(12):1671–1680.

80. Lee JY, Harvey WF, Price LL, Paulus JK, Dawson-Hughes B, McAlindon TE. Relationship of bone mineral density to progression of knee osteoarthritis. *Arthritis Rheum.* 2013;65(6):1541–1546.
81. Yan J-Y, Tian F-M, Wang W-Y, et al. Age dependent changes in cartilage matrix, subchondral bone mass, and estradiol levels in blood serum, in naturally occurring osteoarthritis in guinea pigs. *Int J Mol Sci.* 2014;15(8):13578–13595.
82. Anderson-MacKenzie JM, Quasnicka HL, Starr RL, Lewis EJ, Billingham MEJ, Bailey AJ. Fundamental subchondral bone changes in spontaneous knee osteoarthritis. *Int J Biochem Cell Biol.* 2005;37(1):224–236.
83. Wang T, Wen C-Y, Yan C-H, Lu W-W, Chiu K-Y. Spatial and temporal changes of subchondral bone proceed to microscopic articular cartilage degeneration in guinea pigs with spontaneous osteoarthritis. *Osteoarthr Cartil.* 2013;21(4):574–581.
84. Sun Y, Scannell BP, Honeycutt PR, Mauerhan DR, H JN, Hanley Jr EN. Cartilage degeneration, subchondral mineral and meniscal mineral densities in Hartley and Strain 13 guinea pigs. *Open Rheumatol J.* 2015;9(1):65–70.
85. Muraoka T, Hagino H, Okano T, Enokida M, Teshima R. Role of subchondral bone in osteoarthritis development: A comparative study of two strains of guinea pigs with and without spontaneously occurring osteoarthritis. *Arthritis Rheum.* 2007;56(10):3366–3374.
86. Jimenez PA, Harlan PM, Chavarria AE, Haimes HB. Induction of osteoarthritis in guinea pigs by transection of the anterior cruciate ligament: Radiographic and histopathological changes. *Inflamm Res.* 1995;44(S2):S129–S130.
87. Jimenez PA, Glasson SS, Trubetskoy O V, Haimes HB. Spontaneous osteoarthritis in

- Dunkin Hartley guinea pigs: histologic, radiologic, and biochemical changes. *Lab Anim Sci.* 1997;47(6):598–601.
88. Sun Y, Kiraly AJ, Sun AR, Cox M, Mauerhan DR, Hanley EN. Effects of a phosphocitrate analogue on osteophyte, subchondral bone advance, and bone marrow lesions in Hartley guinea pigs. *Bone Joint Res.* 2018;7(2):157–165.
 89. Huebner JL, Williams JM, Deberg M, Henrotin Y, Kraus VB. Collagen fibril disruption occurs early in primary guinea pig knee osteoarthritis. *Osteoarthr Cartil.* 2010;18(3):397–405.
 90. Kim JE, Song D, Kim SH, Jung Y, Kim SJ. Development and characterization of various osteoarthritis models for tissue engineering. Lammi MJ, editor. *PLoS One.* 2018;13(3):1–15.
 91. Wei L, Svensson O, Hjerpe A. Correlation of morphologic and biochemical changes in the natural history of spontaneous osteoarthrosis in guinea pigs. *Arthritis Rheum.* 1997;40(11):2075–2083.
 92. Bolbos R, Benoit-Cattin H, Langlois J-B, et al. Measurement of knee cartilage thickness using MRI: a reproducibility study in a meniscectomized guinea pig model of osteoarthritis. *NMR Biomed.* 2008;21(4):366–375.
 93. Sandell LJ. Etiology of osteoarthritis: Genetics and synovial joint development. *Nat Rev Rheumatol.* 2012;8(2):77–89.
 94. Sun Y, Mauerhan DR, Honeycutt PR, et al. Analysis of meniscal degeneration and meniscal gene expression. *BMC Musculoskelet Disord.* 2010;11(1):19.

95. Du G, Zhan H, Ding D, et al. Abnormal mechanical loading induces cartilage degeneration by accelerating meniscus hypertrophy and mineralization after ACL injuries in vivo. *Am J Sports Med.* 2016;44(3):652–663.
96. McDougall JJ, Andruski B, Schuelert N, Hallgrímsson B, Matyas JR. Unravelling the relationship between age, nociception and joint destruction in naturally occurring osteoarthritis of Dunkin Hartley guinea pigs. *Pain.* 2009;141(3):222–232.
97. Ding M, Danielsen CC, Hvid I. Age-related three-dimensional microarchitectural adaptations of subchondral bone tissues in guinea pig primary osteoarthrosis. *Calcif Tissue Int.* 2006;78(2):113–122.
98. Panahifar A, Jaremko JL, Tessier AG, et al. Development and reliability of a multi-modality scoring system for evaluation of disease progression in pre-clinical models of osteoarthritis: Celecoxib may possess disease-modifying properties. *Osteoarthr Cartil.* 2014;22(10):1639–1650.
99. Kon E, Ronga M, Filardo G, et al. Bone marrow lesions and subchondral bone pathology of the knee. *Knee Surgery, Sport Traumatol Arthrosc.* Springer Berlin Heidelberg; 2016;24(6):1797–1814.
100. Burnett WD, Kontulainen SA, McLennan CE, et al. Knee osteoarthritis patients with more subchondral cysts have altered tibial subchondral bone mineral density. *BMC Musculoskelet Disord.* BMC Musculoskeletal Disorders; 2019;20(1):1–9.
101. Silverstein E, Sokoloff L. Natural history of degenerative joint disease in small laboratory animals. 5. Osteoarthritis in guinea pigs. *Arthritis Rheum.* 1958;1(1):82–86.
102. Zuck TT. Age order of epiphyseal union in the guinea pig. *Anat Rec.* 1938;70(4):389–

- 399.
103. Fazzalari NL, Parkinson IH. Femoral trabecular bone of osteoarthritic and normal subjects in an age and sex matched group. *Osteoarthr Cartil.* 1998;6(6):377–382.
 104. Buckland-Wright JC, Macfarlane DG, Jasani MK, Lynch JA. Quantitative microfocal radiographic assessment of osteoarthritis of the knee from weight bearing tunnel and semiflexed standing views. *J Rheumatol.* 1994;21(9):1734–1741.
 105. Chen Y, Wang T, Guan M, et al. Bone turnover and articular cartilage differences localized to subchondral cysts in knees with advanced osteoarthritis. *Osteoarthr Cartil.* 2015;23(12):2174–2183.
 106. Patel V, Issever AS, Burghardt A, Laib A, Ries M, Majumdar S. MicroCT evaluation of normal and osteoarthritic bone structure in human knee specimens. *J Orthop Res.* 2003;21(1):6–13.
 107. Hwang J, Bae WC, Shieu W, Lewis CW, Bugbee WD, Sah RL. Increased hydraulic conductance of human articular cartilage and subchondral bone plate with progression of osteoarthritis. *Arthritis Rheum.* 2008;58(12):3831–3842.
 108. Kaspiris A, Khaldi L, Grivas TB, et al. Subchondral cyst development and MMP-1 expression during progression of osteoarthritis: An immunohistochemical study. *Orthop Traumatol Surg Res. Elsevier Masson SAS;* 2013;99(5):523–529.
 109. Findlay DM, Kuliwaba JS. Bone–cartilage crosstalk: a conversation for understanding osteoarthritis. *Bone Res.* 2016;4(1):16028.

Appendix A – Additional Tables and Figures

This section consists of tables containing results from the subchondral bone microarchitecture analysis, which were graphically represented in the main thesis.

Table A-1. Mean (\pm SD) bone microarchitecture parameter results of the medial, lateral and central femur across age groups

Bone microarchitecture outcomes	Femur				
	2 months	4 months	6 months	12 months	24 months
Maximum Sbp.Th (mm)					
Medial	0.30 \pm 0.24	0.50 \pm 0.05	0.58 \pm 0.10	0.53 \pm 0.08	0.85 \pm 0.18
Lateral	0.35 \pm 0.24	0.46 \pm 0.04	0.51 \pm 0.08	0.52 \pm 0.04	0.57 \pm 0.05
Central	0.24 \pm 0.13	0.45 \pm 0.04	0.58 \pm 0.05	0.55 \pm 0.10	0.54 \pm 0.30
Tb.BMD (mgHA/cm ³)					
Medial	404.8 \pm 30.0	457.5 \pm 21.3	526.9 \pm 62.0	509.2 \pm 28.7	452.3 \pm 50.8
Lateral	355.2 \pm 10.3	442.0 \pm 28.9	517.6 \pm 141.6	480.8 \pm 50.7	405.2 \pm 55.9
Central	294.1 \pm 17.5	338.4 \pm 18.8	308.4 \pm 200.6	370.7 \pm 38.6	323.2 \pm 51.1
Sbp.Po (%)					
Medial	4.62 \pm 3.46	1.75 \pm 1.09	0.44 \pm 0.40	0.16 \pm 0.10	3.63 \pm 3.56
Lateral	4.33 \pm 2.72	1.79 \pm 1.36	0.52 \pm 0.37	0.13 \pm 0.10	0.75 \pm 0.49
Central	1.82 \pm 0.92	2.36 \pm 0.90	1.38 \pm 0.65	0.73 \pm 0.71	2.57 \pm 0.58
Tb.BV/TV (%)					
Medial	37.5 \pm 3.4	43.6 \pm 2.5	48.4 \pm 4.9	47.5 \pm 3.0	41.9 \pm 5.4
Lateral	31.6 \pm 0.6	41.4 \pm 3.0	44.0 \pm 5.1	44.4 \pm 5.1	36.8 \pm 6.0
Central	25.9 \pm 1.6	31.8 \pm 1.7	35.8 \pm 4.3	34.5 \pm 3.8	29.4 \pm 5.2

Table A-1. (*Continued*)

Bone microarchitecture outcomes	Femur				
	2 months	4 months	6 months	12 months	24 months
Tb.Th (mm)					
Medial	0.10 ± 0.01	0.12 ± 0.004	0.14 ± 0.01	0.14 ± 0.01	0.14 ± 0.01
Lateral	0.09 ± 0.001	0.11 ± 0.004	0.13 ± 0.01	0.13 ± 0.01	0.13 ± 0.004
Central	0.08 ± 0.002	0.10 ± 0.002	0.12 ± 0.01	0.12 ± 0.01	0.13 ± 0.01
Tb.N (mm ⁻¹)					
Medial	3.93 ± 0.14	3.42 ± 0.36	3.63 ± 0.49	3.55 ± 0.35	2.50 ± 0.23
Lateral	3.56 ± 0.19	3.36 ± 0.37	3.37 ± 0.45	3.34 ± 0.44	2.36 ± 0.44
Central	2.22 ± 0.20	2.01 ± 0.37	2.24 ± 0.38	2.17 ± 0.46	1.43 ± 0.51
Tb.Sp (mm)					
Medial	0.23 ± 0.02	0.29 ± 0.03	0.29 ± 0.04	0.29 ± 0.03	0.39 ± 0.06
Lateral	0.26 ± 0.02	0.29 ± 0.03	0.31 ± 0.04	0.31 ± 0.04	0.43 ± 0.10
Central	0.51 ± 0.05	0.61 ± 0.13	0.56 ± 0.09	0.57 ± 0.16	0.91 ± 0.46

Table A-2. Mean (\pm SD) bone microarchitecture parameter results of the medial, lateral and central tibia across age groups.

	Tibia				
Bone microarchitecture outcomes	2 months	4 months	6 months	12 months	24 months
Maximum Sbp.Th (mm)					
Medial	0.23 \pm 0.04	0.49 \pm 0.11	0.56 \pm 0.10	0.51 \pm 0.08	0.51 \pm 0.11
Lateral	0.20 \pm 0.02	0.48 \pm 0.13	0.49 \pm 0.14	0.49 \pm 0.05	0.50 \pm 0.06
Central	0.32 \pm 0.05	0.45 \pm 0.06	0.62 \pm 0.16	0.59 \pm 0.11	0.72 \pm 0.06
Tb.BMD (mgHA/cm³)					
Medial	408.6 \pm 31.9	517.6 \pm 15.5	570.1 \pm 34.3	572.0 \pm 24.0	530.1 \pm 23.3
Lateral	405.3 \pm 30.4	494.8 \pm 35.3	523.4 \pm 34.3	551.9 \pm 31.4	470.7 \pm 22.1
Central	316.1 \pm 43.7	375.9 \pm 22.6	423.9 \pm 32.0	400.6 \pm 46.9	360.3 \pm 31.0
Sbp.Po (%)					
Medial	4.91 \pm 0.42	1.50 \pm 0.89	0.57 \pm 0.35	0.34 \pm 0.26	1.31 \pm 0.74
Lateral	4.20 \pm 3.13	1.95 \pm 1.06	0.53 \pm 0.27	0.18 \pm 0.09	1.72 \pm 0.72
Central	4.31 \pm 0.27	1.27 \pm 0.51	0.76 \pm 0.58	0.73 \pm 0.36	1.81 \pm 0.54
Tb.BV/TV (%)					
Medial	38.1 \pm 3.7	50.1 \pm 1.8	54.1 \pm 4.2	54.0 \pm 2.6	51.2 \pm 2.7
Lateral	37.3 \pm 3.7	47.1 \pm 4.2	48.5 \pm 3.7	51.3 \pm 3.5	43.9 \pm 2.9
Central	28.2 \pm 5.2	34.6 \pm 2.9	38.9 \pm 3.6	36.6 \pm 4.7	31.0 \pm 3.5
Tb.Th (mm)					
Medial	0.09 \pm 0.004	0.12 \pm 0.01	0.13 \pm 0.01	0.13 \pm 0.004	0.14 \pm 0.01
Lateral	0.09 \pm 0.004	0.11 \pm 0.01	0.13 \pm 0.01	0.13 \pm 0.01	0.12 \pm 0.01
Central	0.08 \pm 0.004	0.10 \pm 0.003	0.12 \pm 0.01	0.12 \pm 0.01	0.13 \pm 0.01

Table A-2. *(Continued)*

Tibia					
Bone microarchitecture outcomes	2 months	4 months	6 months	12 months	24 months
Tb.N (mm⁻¹)					
Medial	4.36 ± 0.36	4.28 ± 0.46	4.54 ± 0.65	4.28 ± 0.44	3.34 ± 0.15
Lateral	4.50 ± 0.28	4.13 ± 0.70	4.19 ± 0.70	4.22 ± 0.47	3.16 ± 0.34
Central	3.16 ± 0.31	3.08 ± 0.51	3.45 ± 0.48	3.13 ± 0.52	2.31 ± 0.17
Tb.Sp (mm)					
Medial	0.21 ± 0.03	0.23 ± 0.02	0.24 ± 0.03	0.25 ± 0.03	0.28 ± 0.01
Lateral	0.20 ± 0.02	0.24 ± 0.04	0.25 ± 0.03	0.25 ± 0.03	0.30 ± 0.04
Central	0.33 ± 0.03	0.36 ± 0.05	0.33 ± 0.03	0.36 ± 0.05	0.43 ± 0.04

Appendix B – Extended Methods

Below is an outline of the quantitative μ CT image analysis pipeline used in this study.

Step 1 – Contouring:

1. Images obtained from a Scanco Medical μ CT scanner can be visualized and analyzed on a computer with access to OpenVMS and the XQuartz app.
2. In the Terminal app, login to the IP address of the μ CT scanner. Scans can be viewed by entering “uct_evaluation” in the command line.
3. Open image and draw rough contours around the epiphysis of the bones. Separate the tibia and femur contours by saving GOBJ as _TROUGH or FROUGH.GOBJ respectively.
4. Run scripts for “Auto Contour Slab with cut-out and SEG TIBIA(FEMUR) – Guinea pig 10um) to make periosteal gobjs.
5. Upon completion of autocontour script, load the periosteal gobjs (_T or _F.GOBJ) and run scripts for “Auto Contour Endosteal Tibia(Femur) – Guinea pig 10um updated”.
6. Navigate to the image directories in OpenVMS and write _T and _F.AIM files from _T and _F.GOBJ files in IPL.
7. Check greyscale AIM file before proceeding. It gets cropped in one of the multiple contouring steps. Run the isq_to_aim command in IPL if that’s the case.

Step 2 – Manual Selection of Joint Compartments (AKA picking points):

1. Download _T(or F)_SEG_R02.AIM files from data disk to a local directory.
2. Install blSurfaceViewer (Bonelab, University of Calgary) on computer, then use it to load _T(or F)_SEG_R02.AIM files.

3. To manually select medial or lateral compartments, press “p” on keyboard and click mouse pointer over region. Use the “z” key to deselect point.
4. Follow the shape of the bone, pick points on the medial side, and press “t” on keyboard to write to text file. Save file as *imageID_T(or F)_MED.TXT* in desired folder.
5. Delete all points, pick points on the lateral side, and save as *imageID_T(or F)_LAT.TXT* in folder.

Step 3 – Convert TXT files to MHA:

1. Download the saltac folder on computer.
2. Open run_saltac.py located in saltac folder and check that the extrusion distance is set to 0.0105, indicative of 10.5 μm voxel size of guinea pig scans.
3. In the Terminal app, run the following commands:

```
conda activate py3  
cd <directory>/saltac/scripts  
python run_saltac.py convert-points-2-roi <location of TXT files> <destination of  
MHA files >
```

Step 4 – Convert MHA to AIM:

1. To convert MHA to AIM files, an AIM writer is required. The bl (Bonelab, University of Calgary) library has one.
2. In the Terminal app, run the following commands:

```
conda activate bl  
cd <location of MHA files>
```

blImageConvert *imageID*_T(or F)_MED(or LAT).MHA *imageID*_T(or F)_MED(or LAT).AIM

3. Transfer *imageID*_T(or F)_MED(or LAT).AIM files back to data disks.

Step 5 – Generate Regions of Interest (ROIs):

1. Open image in uct_evaluation.
2. Check that greyscale AIM is present.
3. Run scripts 164 (Knee - Generate ROI Tibia- Guinea pig 10um) and 175 (Knee - Generate ROI Femur- Guinea pig 10um).

Step 6 – Bone Microarchitecture Evaluation:

1. Run scripts 166 (Knee - Evaluation Tibia - Guinea pig 10um) and 176 (Knee - Evaluation Femur - Guinea pig 10um) in uct_evaluation.
2. Run one at a time. Note that the results TXT file gets populated according to the order of script completion, and also doesn't specify whether results are for tibia or femur.

Step 7 – Analyze the Central Joint Compartment:

1. All image files were transferred from the OpenVMS data disk to a projects disk.
2. A custom IPL script named SUBMIT_CREATE_CENTRAL_KNEE_MASK.COM included all samples.
3. The submit script calls CREATE_CENTRAL_KNEE_MASK_EVAL.COM that uses the *imageID*_T(or F)_MED(and LAT).AIM files to determine the central joint compartment, which then undergoes bone microarchitecture evaluation.

4. The results TXT file gets populated to include the central compartment.
5. Download RESULTS-KNEE.TXT and RESULTS-KNEE_FILELIST.TXT to local computer and open with Microsoft Excel.

This section also includes detailed histological methods that allowed for good sectioning of the Dunkin-Hartley guinea pig knee joint. The knee joint in this model is larger than those of other small rodents (mice and rats), and therefore, takes a lot longer to decalcify.

The guinea pig tibiofemoral joints were fixed in 10% neutral buffered formalin (ThermoFisher Scientific) for five days to preserve morphology and prevent autolysis and bacterial attack. Following fixation, samples were washed with normal saline (Isotonic solution 0.90% w/v) and decalcified in Cal-Ex[®] II (ThermoFisher Scientific) for a total of four weeks. At the two-week mark during decalcification, the joints were transected in half sagittally, and then separate medial and lateral compartments were returned to Cal-Ex[®] II for the remaining two weeks. After decalcification, the samples underwent overnight processing in an automatic tissue processor (Leica TP1020), where they were dehydrated in ethanol (80% - 100%), cleared in Slide Brite[™], and infiltrated in wax (50% Paraplast plus/50% Paraplast extra). Samples were embedded in 50% Paraplast plus/50% Paraplast extra paraffin wax, and 15 µm-thick sections were obtained with a microtome (Leica RM2255). Sections were stained with H&E and toluidine blue histological stains, then imaged with a light microscope (Carl Zeiss Axioplan 2).

Appendix C – Copyright Permissions

<https://www.netterimages.com/invoice-copy.htm?uuid=57476D6A-4DD6-EAFB-3E16-12820B988525>

netterimages


Invoice

Inv no.: NI0016942
Date: 10 Aug 2020

Destiny Francis
The University of Calgary

Telephone: [REDACTED]

Order Summary

Description	Price
 <p><i>Title:</i> Cross Section of the Knee: Coronal View <i>Image #:</i> 57238 <i>Description:</i> 601x409 px, 6.29 MB CMYK JPG <i>Usage:</i> Student Presentation or Poster, Thesis, Dissertation</p>	\$49

Sub Total:	\$49
Discount:	\$0
Tax:	\$0
Total:	\$49

Delivery method: Download

Billed to: Visa ending in [REDACTED]

We at netterimages.com want to thank you for purchasing images through us. In a moment you will receive an e-mail confirming your order. You can view your licenses and download image files on the Licenses Page (in the My Account section of the site).

<https://www.netterimages.com/invoice-copy.htm?uuid=57476D6A-4DD6-EAFB-3E16-12820B988525>

© 2005–2020 Elsevier. All Rights Reserved.

By purchasing this image, you are agreeing to the terms of use on www.netterimages.com.
The license grants permission for the use of this image according to the stated reason for purchase.
Use of this image beyond the stated purpose is strictly prohibited.
No other print or electronic reproduction of this content is allowed other than the use permitted by this agreement.
Content cannot be photocopied, downloaded for electronic or print distribution, downloaded and saved to a CD, DVD or hard drive or provided via link from another website without permission.
Elsevier maintains the complete copyright for the image. No editorial changes can be made to this image without permission.

The appearance of this image must be accompanied by this copyright line: Netter illustration used with permission of Elsevier Inc.
All rights reserved. www.netterimages.com

NETTERIMAGES.COM CONTENT LICENSE AGREEMENT

THIS IS A LEGAL AGREEMENT BETWEEN YOU ("LICENSEE") AND ELSEVIER ("ELSEVIER").
THIS AGREEMENT APPLIES TO LICENSES ISSUED VIA THE WEB AND IS APPLICABLE TO ONLINE, DIGITAL AND PHYSICAL DELIVERY OF LICENSED CONTENT (THE "CONTENT").

1. Definitions. In this Agreement the following definitions apply:

1.1 "Invoice" means the computer-generated invoice provided by Elsevier that may include, without limitation, the permitted scope of use of the Licensed Content selected, any limitations on the license in addition to those specified herein and the corresponding price for the license of such Licensed Content. The Invoice shall be incorporated into this Agreement and all references to the Agreement shall include the Invoice.

1.2 "Licensed Content" means any illustration or digital file protected by copyright, trademark, patent or other intellectual property right, which is licensed to Licensee by Elsevier under the terms of this Agreement.
Any reference in this Agreement to the Licensed Content shall be to each individual item within the Licensed Content and also to the Licensed Content taken as a whole.

1.3 "Reproduction" and "Reproduce" mean any form of copying or publication of the whole or a part of any Licensed Content, via any medium and by whatever means, and the distortion or manipulation of the whole or any part of the Licensed Content and the creation of any derivative work from the Licensed Content.

1.4 "Project and Product" mean the work or works in which the Licensed Content appears.

2. Grant of Rights & Restrictions.

2.1 Unless stated otherwise in the Invoice, Elsevier grants to Licensee a non-exclusive, non-sublicensable and non-assignable right to Reproduce the Licensed Content identified in the Invoice, solely to the extent explicitly stated in this Agreement. This right may be exercised by subcontractors of Licensee, provided that such subcontractors agree to abide by the terms of this Agreement.

2.2 Use of the Licensed Content is strictly limited to the use, medium, period of time, print run and any other restrictions specified in the Invoice. Licensee may utilize the Licensed Content in any production process that may be necessary for the intended use specified in the Invoice.

2.3 Use of the Licensed Content is one time. No more than ten (10) Illustrations shall be reproduced in any one project or product at any one time. For subsequent uses of the Licensed Content, Licensee must purchase subsequent licenses.

2.4 While efforts have been made to correctly caption the subject matter of the Licensed Content, Elsevier does not warrant that such information is accurate.

2.5 Pornographic, defamatory or otherwise unlawful use of Licensed Content is strictly prohibited whether directly or in context or juxtaposition with specific subject matter.

2.6 Licensed Content shall not be incorporated into a logo, trademark

or service mark.

2.7 Licensed Content shall not be used contrary to any restriction on use that is notified to Licensee prior to or at the time the Licensed Content is delivered to Licensee. Such restrictions may be included in the information provided with the Licensed Content on Elsevier website or in any other communication by Elsevier. Any such restriction provided to the Licensee shall be incorporated in this Agreement.

2.8 The granting or sale of subsidiary rights to the Licensed Content is not permitted under this agreement.

2.9 Upon reasonable notice, Elsevier may inspect any records, accounts and books relating to the Reproduction of any of the Licensed Content to ensure that the Licensed Content is being used in accordance with this Agreement.

3. Copyright. No ownership or copyright in any Licensed Content shall pass to Licensee by the issuance of the license contained in this Agreement. Except as expressly stated in this Agreement, Elsevier grants Licensee no right or license, express or implied, to the Licensed Content.

4. Warranty and Limitation of Liability.

4.1 Elsevier warrants that:

(i) it has all necessary rights and authority to enter into and perform this Agreement; and
(ii) Licensee's use of the Licensed Content in its original form, and when used in accordance with this Agreement and the Invoice, will not infringe on any copyright, moral right, trademark or other intellectual property right and will not violate any right of privacy or right of publicity.

4.2 ELSEVIER MAKES NO OTHER WARRANTIES, EXPRESS OR IMPLIED, REGARDING THE LICENSED CONTENT, INCLUDING, WITHOUT LIMITATION, ANY IMPLIED WARRANTIES OF MERCHANTABILITY OR FITNESS FOR A PARTICULAR PURPOSE. ELSEVIER SHALL NOT BE LIABLE TO LICENSEE OR ANY OTHER PERSON OR ENTITY FOR ANY GENERAL, PUNITIVE, SPECIAL, INDIRECT, CONSEQUENTIAL OR INCIDENTAL DAMAGES, OR LOST PROFITS OR ANY OTHER DAMAGES, COSTS OR

LOSSES ARISING OUT OF LICENSEE'S USE OF THE LICENSED CONTENT OR OTHERWISE, EVEN IF ELSEVIER HAS BEEN ADVISED OF THE POSSIBILITY OF SUCH DAMAGES, COSTS OR LOSSES. ELSEVIER'S MAXIMUM LIABILITY ARISING OUT OF OR IN CONNECTION WITH LICENSEE'S USE OF OR INABILITY TO USE THE LICENSED CONTENT (WHETHER IN CONTRACT, TORT OR OTHERWISE) SHALL, TO THE EXTENT PERMITTED BY LAW, BE LIMITED TO THE VALUE PAID BY THE LICENSEE FOR THE LICENSED CONTENT.

4.3 THE REPRESENTATIONS AND WARRANTIES MADE BY ELSEVIER IN THIS AGREEMENT APPLY ONLY TO THE LICENSED CONTENT AS DELIVERED BY ELSEVIER AND WILL BE INVALID IF THE LICENSED CONTENT IS USED BY LICENSEE IN ANY MANNER NOT SPECIFICALLY AUTHORIZED IN THIS AGREEMENT OR IF LICENSEE IS OTHERWISE IN BREACH OF THIS AGREEMENT.

5. Indemnification.

5.1 Provided Licensed Content is only used in accordance with this Agreement and Licensee is not otherwise in breach of this Agreement, Elsevier shall defend, indemnify and hold Licensee harmless from all damages (except punitive damages), liabilities and expenses (including reasonable attorneys' fees and permitted and authorized costs), arising out of or connected with any actual or threatened lawsuit, claim or legal proceeding alleging that Elsevier is in breach of its warranties given in section 4 above.

THE FOREGOING STATES ELSEVIER ENTIRE INDEMNIFICATION OBLIGATION UNDER THIS AGREEMENT AND LICENSEE'S SOLE AND EXCLUSIVE REMEDY FOR ANY ALLEGED OR ACTUAL BREACH OF THE REPRESENTATIONS AND WARRANTIES SET FORTH IN SECTION 4 ABOVE.

5.2 If Licensee's use of the Licensed Content is not authorized by this Agreement, Licensee shall defend, indemnify and hold Elsevier and its parent, subsidiaries and commonly owned or controlled affiliates and their respective officers, directors and employees harmless from all damages, liabilities and expenses (including reasonable attorneys' fees and costs), arising out of or connected with any actual or threatened lawsuit, claim or legal proceeding relating to the use of such Licensed Content by Licensee, to the extent that such claim relates to the absence of a release or the Licensee's unauthorized use of the Licensed Content.

6. Notice of Defense. The party seeking indemnification pursuant to section 5 shall promptly notify the other party of such claim. At indemnifying party's option, indemnifying party may assume the handling, settlement or defense of any claim or litigation, in which event indemnified party shall cooperate in the defense thereof. Indemnified party shall have the right to participate in such litigation, at its expense, through counsel selected by indemnified party. The indemnifying party will not be liable for legal fees and other costs incurred prior to the other party giving notice of the claim for which indemnity is sought.

7. Parties' Obligation. Upon notice from Elsevier, or upon Licensee's knowledge that any Licensed Content is subject to a threatened or actual claim of infringement, violation of another right, or any other claim for which Elsevier may be liable herein, or if Elsevier withdraws any Licensed Content for any good reason, Licensee will physically remove the Licensed Content from its premises, computer systems and storage (electronic or physical) and, if possible, cease any future use at its own expense. Elsevier shall provide Licensee with comparable Licensed Content (which comparability will be determined by Elsevier in its reasonable commercial judgment) free of charge, but subject to the other terms and conditions of this Agreement.

8. Electronic Storage. For all Licensed Content that Licensee takes delivery of in electronic form, Licensee must retain the copyright symbol, the name of Elsevier, the artist's signature, and the image number or other identification number associated with the Licensed Material as may be included as part of the electronic file. Licensee may not make additional high-resolution copies of the Licensed Content and Licensee will maintain a robust firewall to safeguard against unauthorized third-party access to the Licensed Content. Notwithstanding the foregoing, Licensee may make one (1) high-resolution backup copy of the Licensed Content for security reasons only. Upon the expiration of this Agreement, Licensee shall promptly delete the Licensed Content from its computer or other electronic storage systems and shall ensure that its sub-contractors do likewise.

9. Condition of Licensed Content. Licensee should examine all Licensed Content for possible defects (whether digital or otherwise) before sending any Licensed Content for Reproduction. Without prejudice to section 4.1. (ii) above, Elsevier shall not be liable for any loss or damage suffered by Licensee or any third party, whether directly or indirectly, arising from any alleged or actual defect in any Licensed Content or its caption or in any way from its Reproduction.

10. Credit Lines for Editorial Use. Any Licensed Content that is Reproduced will be accompanied by the following credit line, "[republication date]. Used with permission of Elsevier. All rights reserved." The image will preserve "Netter" or other artist's signature in the file. The credit line must appear adjacent to the Licensed Content. If any Licensed Content Reproduced by Licensee omits the requisite credit line, an additional fee equal to two times the original amount invoiced shall be payable by Licensee at Elsevier's discretion. The foregoing fee shall be in addition to any other rights or remedies that Elsevier may have at law or in equity.

11. Miscellaneous Terms.

11.1 Unauthorized Use. Any use of Licensed Content in a manner not expressly authorized by this Agreement or in breach of a term of this Agreement constitutes copyright infringement, entitling Elsevier to exercise all rights and remedies available to it under copyright laws around the world. Licensee shall be responsible for any damages resulting from any such copyright infringement, including any claims by a third party. In addition and without prejudice to Elsevier other remedies under this Agreement, Elsevier reserves the right to charge and Licensee agrees to pay a fee equal to five times Elsevier normal license fee for use of the Licensed Content.

11.2 Governing Law. This Agreement will be governed in all respects by the laws of the State of New York, U.S.A., without reference to its laws relating to conflicts of law. Any disputes arising from this Agreement or its enforceability shall be settled by binding arbitration to be held in New York, New York. If Elsevier and Licensee are unable to agree on the location of the

arbitration, Elsevier decision shall be final.
The United Nations Convention on Contracts for the International Sale of Goods does not govern this Agreement.
Notwithstanding the foregoing, Elsevier shall have the right to commence and prosecute any legal or equitable action or proceeding before any court of competent jurisdiction to obtain injunctive or other relief against
Licensee in the event that, in the opinion of Elsevier, such action is necessary or desirable.

11.3 Severability. If one or more of the provisions contained in the Agreement is found to be invalid, illegal or unenforceable in any respect, the validity, legality and enforceability of the remaining provisions shall not be affected. Such provisions shall be revised only to the extent necessary to make them enforceable.

11.4 Waiver. No action of Elsevier, other than express written waiver, may be construed as a waiver of any provision of this Agreement. A delay on the part of Elsevier in the exercise of its rights or remedies will not operate as a waiver of such rights or remedies, and a single or partial exercise by Elsevier of any such rights or remedies will not preclude other or further exercise of that right or remedy.
A waiver of a right or remedy on any one occasion will not be construed as a bar to or waiver of those rights or remedies on any other occasion.

11.5 Entire Agreement.
This Agreement, including the Invoice, contains all the terms of the license agreement and no terms or conditions may be added or deleted unless made in writing and signed by an authorized representative of both parties.
In the event of any inconsistency between the terms contained herein and the terms contained on any purchase order or other communication sent by Licensee, the terms of this Agreement shall govern.
It is your duty to retain a copy of this license.

**WOLTERS KLUWER HEALTH, INC. LICENSE
TERMS AND CONDITIONS**

Jun 11, 2020

This Agreement between Destiny Francis ("You") and Wolters Kluwer Health, Inc. ("Wolters Kluwer Health, Inc.") consists of your license details and the terms and conditions provided by Wolters Kluwer Health, Inc. and Copyright Clearance Center.

License Number 4846230783904

License date Jun 11, 2020

Licensed Content Publisher Wolters Kluwer Health, Inc.

Licensed Content Publication Journal of the American Academy of Orthopaedic Surgeons

Licensed Content Title Restoration of Injured or Degenerated Articular Cartilage

Licensed Content Author Joseph Buckwalter, Van Mow, and Anthony Ratchliffe

Licensed Content Date Jul 1, 1994

Licensed Content Volume 2

Licensed Content Issue 4

Type of Use Dissertation/Thesis

Requestor type University/College

Sponsorship No Sponsorship

Format Electronic

Will this be posted on a password protected website?	No
Portion	Figures/tables/illustrations
Number of figures/tables/illustrations	1
Author of this Wolters Kluwer article	No
Will you be translating?	No
Intend to modify/adapt the content	Yes
Title	The Natural History of Bone Marrow Lesions and Cysts in the Dunkin-Hartley Guinea Pig Knee Osteoarthritis Model
Institution name	University of Calgary
Expected presentation date	Aug 2020
Portions	Figure 1
	Destiny Francis [REDACTED]
Requestor Location	Calgary, AB [REDACTED] Canada Attn:
Billing Type	Invoice
Billing Address	Destiny Francis [REDACTED] Calgary, AB [REDACTED]